MODELING OF POLYMERIC MATERIALS WITH APPLICATIONS IN ACTIVE MATERIALS AND ADDITIVE MANUFACTURING

A Dissertation
Presented to
The Academic Faculty

by

Craig M. Hamel

In Partial Fulfillment
of the Requirements for the Degree
Doctor of Philosophy in the
George W. Woodruff School of Mechanical Engineering

Georgia Institute of Technology
August 2020

MODELING OF POLYMERIC MATERIALS WITH APPLICATIONS IN ACTIVE MATERIALS AND ADDITIVE MANUFACTURING

Approved by:

Dr. H. Jerry Qi, Advisor
School of Mechanical Engineering
Georgia Institute of Technology

Dr. Karl Jacob
School of Materials Science and Engineering
Georgia Institute of Technology

Dr. Min Zhou
School of Mechanical Engineering
Georgia Institute of Technology

Dr. Kevin N. Long
Sandia National Laboratories

Dr. Yuhang Hu
School of Mechanical Engineering
Georgia Institute of Technology

Date Approved: May 8, 2020

To my loving wife Lizzy Storm and the rest of my family

ACKNOWLEDGEMENTS

First, I would like to express my gratitude to my Ph.D. Professor H. Jerry Qi for his guidance and the challenging problems he presented to me over the last four years of my studies. I think it would be impossible to calculate the amount of time he devoted to discussing my research and helping improve the quality of my written and oral communication skills. This work would have not been possible to finish without his advisement. I would also like to take my committee members: Professor Min Zhou, Professor Yuhang Hu, Professor Karl Jacob, and Dr. Kevin N. Long, for their suggestions, challenging questions, and the time they took out of their busy schedules to serve as my proposal and defense committees. I would also like to give further thanks to Dr. Kevin N. Long for mentoring me during the summer of 2019 at Sandia National Laboratories.

Next, I need to thank all of the current and past group members of Professor Qi's research group. I would like to thank Devin Roach, Dr. Xiao Kuang, Dr. Jiangtao Wu, Conner Dunn, Dr. Vincent Li, Dr. Xiaoming Mu, Xirui Peng, Dr. Zeang Zhao, Dr. Quanyi Mu, Shayuan Weng, Haley Hilborn, Janet Wong, Qiang Zhang, Macrae Montgomery, and Connor Armstrong. Special thanks are needed for my master's thesis advisor Shawn A. Chester for guiding me through my early stages as a researcher.

Finally, I would like to thank my loving wife Lizzy Storm and her relatives, my parents, my two brothers, and my grandmother, for having faith in me throughout the years.

TABLE OF CONTENTS

LIST OF TABLES

LIST OF FIGURES

LIST OF SYMBOLS AND ABBREVIATIONS

The following table lists the most common abbreviations and symbols that are used throughout this dissertation

ML	Machine Learning
EA	Evolutionary Algorithm
FEA	Finite Element Analysis
FEM	Finite Element Method
FDM	Finite Difference Method
SMP	Shape Memory Polymer
DMA	Dynamic Mechanical Analysis
TTS	Time-Temperature Superposition
WLF	Williams-Landel-Ferry
CAD	Computer Aided Design
DMD	Digital Micromirror Device
UV	Ultraviolet
DLP	Digital Light Processing
FTIR	Fourier Transform Infrared Spectroscopy
3D	Three Dimensional
DoC	Degree of Cure

SUMMARY

Polymeric materials used in the settings of active materials and additive manufacturing offer unique challenges for which high fidelity multiphysics modeling would greatly assist in improving processing and component function during service. In recent years there have been many advances in polymeric materials that offer exciting applications such as 3D printing, actuation, and recyclability. With these advances, however, there has been a scarcity of physics driven models to accompany the three applications listed above. Actuation is now possible with many different physical mechanisms due to advances in material synthesis but the coupling of large deformation of these solid materials with physical actuation mechanisms is a vast area of research. This modeling approach is further complicated if one wishes to use these models in a design for 4D printing for example. Modeling of the 3D printing process is also needed to gain further understanding into how processing parameters such as 3D printing ink formulations, printing speed, and others play a role in the geometrical tolerances of printed parts along with the effects these parameters have upon the material properties after manufacturing. Recycling of polymeric materials could also greatly benefit from model driven optimization of processes. With a robust enough model, “virtual” experiments of new recycling methods could be conducted which would greatly reduce both the consumption of time and experiments needed for streamlining a new recycling process.

The objective of this dissertation is to evaluate the use of high-fidelity material models of polymeric materials for applications in active materials and additive manufacturing settings. The general goals are to build models for various stages a polymer

sees during its lifecycle in the application of 3D printing. Specifically, the problems that will be considered are the dissolution of polymeric materials, free radical diffusion in photopolymers during curing in digital light processing (DLP) 3D printing, and design of active structures for 4D printing. For the case of dissolution in polymers, a reaction-diffusion model will be presented and its effectiveness at predicting the dissolution process and will be applied to specialty grade polymers known as vitrimers. The model will enable the streamlining of new recycling processes without the need for a large suite of experimental methods through the use of process simulation. In the case of free radical diffusion in photopolymers in the DLP process a reaction-diffusion model will be presented that can assess the evolution of functional groups at the pixel level and can directly predict the geometric distortion with reasonable agreement to experiments. This work enables further process modeling but in this case the process is manufacturing rather than recycling. Again, type of model can be utilized for optimizing printing parameters such as the light intensity and resin composition to improve geometric tolerance in the future. Design of active structures for 4D printing utilizes non-linear constitutive models coupled with machine learning techniques to determine an ideal material distribution to achieve a pre-defined target shape upon activation from an environmental stimulus. This work will enable the use of high-fidelity physics models in design for 4D printing.

CHAPTER 1. INTRODUCTION

1.1 Background

1.1.1 Overview

Polymeric based materials see several distinct points during their material lifecycle. These include material synthesis, design, material fabrication (such as injection moulding or 3D printing), application and, recycling. Each of these areas has a rich industry surrounding them and has potential for innovation. In the research presented within this dissertation three distinct portions of the polymer lifecycle which were mentioned above will be considered. The first of these will design with a specific end goal of applications in 4D printing in mind. The goal of this portion of the research is to determine how to properly distribute multiple materials within a printed part to achieve a pre-defined shape change upon activation by an external stimulus. The second region of a polymer lifecycle that will be considered is modeling the manufacturing of polymer parts via a 3D printing method known as digital light processing (DLP). The third portion of the research will focus on modeling the recycling of polymeric materials.

1.1.2 Design for active composites and 4D printing

Active materials and composites are a class of materials which can respond to environmentally triggered phenomena. Different classes of active materials include shape memory polymers [1], light active shape memory polymers [2], dielectric elastomers [3], liquid crystal elastomers [4, 5], as well as hydrogels [6, 7]. Upon an environmental stimulus, the responsive material undergoes actuation which causes a shape change or

property change. There are many physical mechanisms which have been utilized to achieve actuation in materials such as temperature [8-16], water , electromagnetism, pH, and light [2, 17-19] to name a few. An interesting application of these materials is to fabricate composites consisting of active materials within the confinement of a non-active matrix. The key ingredients to these composites are an active material and a passive material. The passive material is usually compliant to allow for large actuation while the active material may be activated by different stimuli such as light, electricity, temperature, magnetism etc. The shape-change or the actuation depends on the spatial arrangement of active and non-active components in these composites. This imparts an advantage of soft active composites that through the layout design of active and passive phases throughout a structure, a variety of actuation responses can be achieved upon external stimuli. Recent advances in additive manufacturing (or 3D printing) enable accurate placement of different materials in a single part which allows for the ease of fabrication of the composites described above. These improvements thus allow for the rapid design and manufacture of structures composed of active materials, which can add functionality to normally static mechanical components. This also leads to the term 4D printing [20, 21] which is a recent paradigm that can allow a normally static 3D printed part to be transformed into a different shape upon activation by an external stimulus such as temperature or other physical phenomenon. 4D printing has potential applications in sensors, robotics, bio-medical applications, smart actuators, and MEMS devices. Figure 1.1 shows several examples of various 4D printing paradigms.

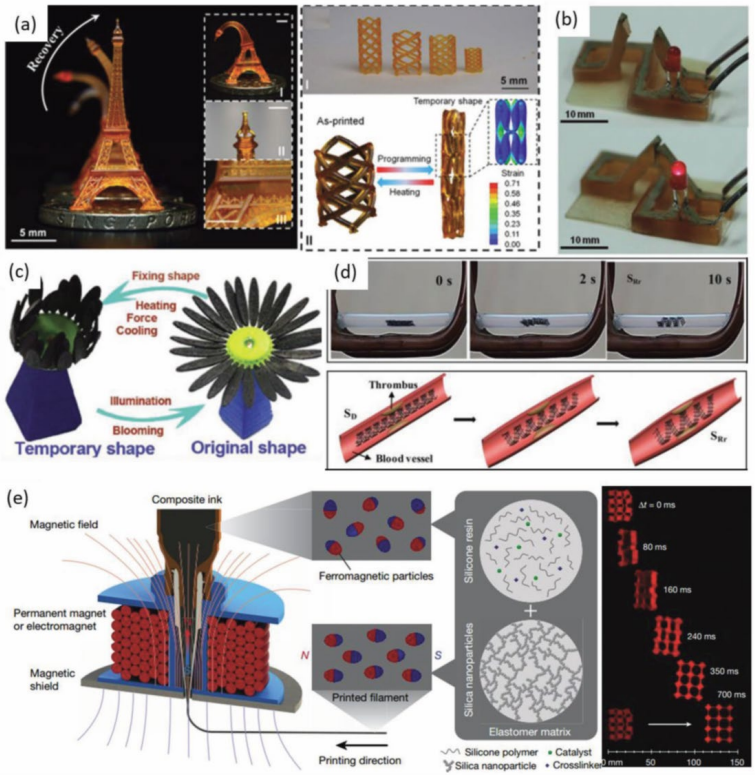

Figure 1.1 4D printing of one-way SMP by different printing techniques. a) PμSL for printing SM Eiffel Tower with high resolution (left) and PμSL printed stent with tunable dimension parameters (right). Reproduced with permission. b) SLA printed an SM device for the temperature sensor. c) Photo-triggered shape memory behavior of FDM printed sunflower from closed to opened state like the blooming of flowers. Reproduced with permission. d) A potential application of the 4D printed scaffold as an intravascular stent. e) Design of ferromagnetic domains in 3D printed soft materials (left) and horizontal leap of a 3D auxetic structure upon sudden reversal of the applied magnetic field direction while attenuating the field strength by rotating a permanent magnet by 90° (right). [21]

Design for 4D printing and active composites is a challenging task. Often the goal is to shape morph a structure from a flat shape to a predefined complex shape. This by nature is an inverse problem in terms of theoretical mechanics. In solid mechanics the usual approach to solving problems is to define a geometry, assign material properties for different regions of the defined geometry, apply boundary conditions, and then solve the continuum balance laws for the displacement field and stress for example. Determining a

material distribution for a given displacement or stress field is the opposite of this approach. Often this inverse problem, in terms of theories of partial differential equations, may not have a solution which exists, or the solution may not be unique. Even if a non-unique solution exists the problem can also suffer from numerical stability issues as well.

Several approaches have been used in recent years for designing material property distributions to achieve a desired shape morphing mode. The first approach that was utilized (and is still utilized to this day) is a trial and error or intuition driven approach [1, 14]. This can be a time and material consuming process requiring many iterations of a design to achieve a desired goal. Furthermore, it is often necessary to have some past experience with the materials the designer wants to use. The second approach which has been utilized to overcome the intuition-based trial and error approach is to use multi-material topology optimization. The drawbacks of this approach are numerical instability and the need to represent a possibly discrete material distribution, which is often seen in voxel-based 3D printing, using a continuous representation. The stability issue often necessitates the need to use simple linearized models which often do not capture all of the physical mechanisms present in shape actuation, thus reducing the fidelity of the physical models. Having a continuous approximation of a discrete material distribution necessitates the need for a post-processing step where a continuous distribution can be discretized into multiple parts, one for each material, which is the typical approach for multi-material 3D printing. The real need in the advancement of design for 4D printing is the ability to determine a material distribution of active and passive phases in a structure in a relatively efficient way which captures all of the relevant physics required for the activation or shape shifting of the materials utilized to print the original structure.

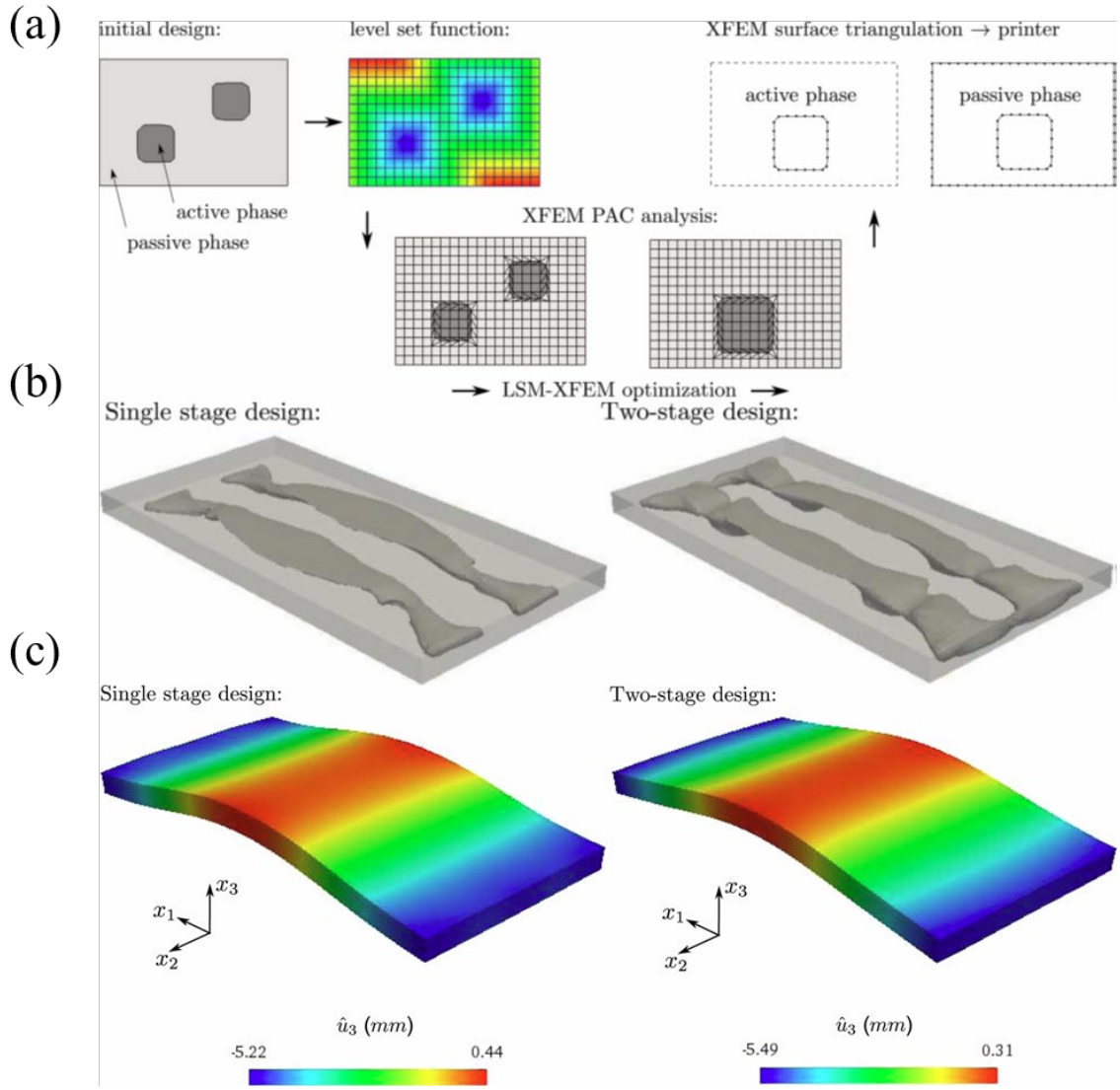

Figure 1.2 Use of topology optimization in active composites design. (a) Simulation strategy using Level the extended finite element method. (b) Calculated material distribution. (c) Simulation results showing the displacement field for different simplified active composites models. [22]

1.1.3 Digital Light Processing 3D printing

Additive manufacturing (AM), also known as 3D printing, is a rapidly growing technology which can fabricate 3D objects using non-destructive manufacturing processes by adding successive layers of material. This technology has the capabilities to

revolutionize the way in which manufacturing, and product development is conducted due to the large design freedom, rapid prototyping, customization, among other beneficial properties. The process typically involves building a computer aided design model (CAD) and converting this model to a file format understandable by the printer, typically a STL file. There are many different types of AM such as stereolithography (SLA), selective laser sintering (SLS), fused deposition modeling (FDM), and digital light processing (DLP) to name a few. Different processes allow for the fabrication of parts with different classes of materials. However, there is no universal AM process which can use all materials.

DLP is a process dependent upon the mechanism of photopolymerization where a liquid resin is exposed with light and cured into a solid polymer. Photopolymerization based methods account for nearly half of the 3D printing market [23]. A common DLP setup usually involves three parts. The first is a light projector which enables the curing mechanism in photopolymers, the second is a resin vat which acts a reservoir for liquid photopolymeric resin, and the third is a motion stage which allows for the layer by layer process. Prior to printing a 3D computer aided design (CAD) model is sliced into many 2D patterns which are built one on top of another to create a 3D part as shown in Figure 1.3. This pre-processing step of the 3D geometry into many discrete slices creates a jagged pattern in the printing direction which ultimately results in a rough part. This jagged pattern can be overcome by further processing the individual sliced images from being black and white to having grayscale [24-26]. In a typical DLP printing process, a source of UV or visible light (typically a projector) is used to project an image, which corresponds to a slice of 3D part, onto a vat of liquid resin. The light then cures the liquid photopolymer resin into a solid part. This process continues in a layer by layer matter until a full 3D part has

been printed. This form of AM is particularly attractive due to the rapid liquid to sold phase change which allows for the rapid production of 3D parts using only a light source and computer as a control. This allows for fast printing due to fast solidification and because a single layer can be cured in a one-shot process unlike extrusion-based processes such as fused deposition modeling or direct ink write. These features make DLP an extremely attractive additive manufacturing method. In practical applications the light is exposed for a few seconds to a minute depending upon the resin formulation and intensity of the projector. It is often advantageous to use a shorter curing time to increase the throughput of printing parts and to avoid overcuring of the resin which can lead to part distortion. However, this is not always possible depending upon the resin formulation and application end goal.

The curing process changes the underlying microstructure which influences the macroscopic materials properties of the solid such as the modulus, diffusivity, and glass transition temperature [27]. The coupling of the light exposure with the chemical reactions responsible for curing is quite complex. The light intensity is not uniform within the plane of the liquid resin due to discrete light beams imparted by a digital micro-mirror device (DMD), as shown in Figure 1.3 and Figure 1.4, and the liquid resin can also absorb the light through the thickness causing another dimension of non-uniformity of light intensity. These mechanisms of spatial variation in light intensity result in chemical concentration gradients within the 3D printed specimen, which cause diffusion of different reacting species. In total, these mechanisms and non-uniform material properties in 3 dimensions can be an unattractive phenomenon in engineering applications, but it is difficult to understand these highly coupled, multi-physics effects on component function without

suitable process models. Hence, a significant effort of this work is the development of such a process model. Specifically, on using a reaction-diffusion based photopolymerization model, we can explore this process at the pixel scale to determine the effect of different processing parameters such as layer cure thickness and exposure times on the result material and component behavior.

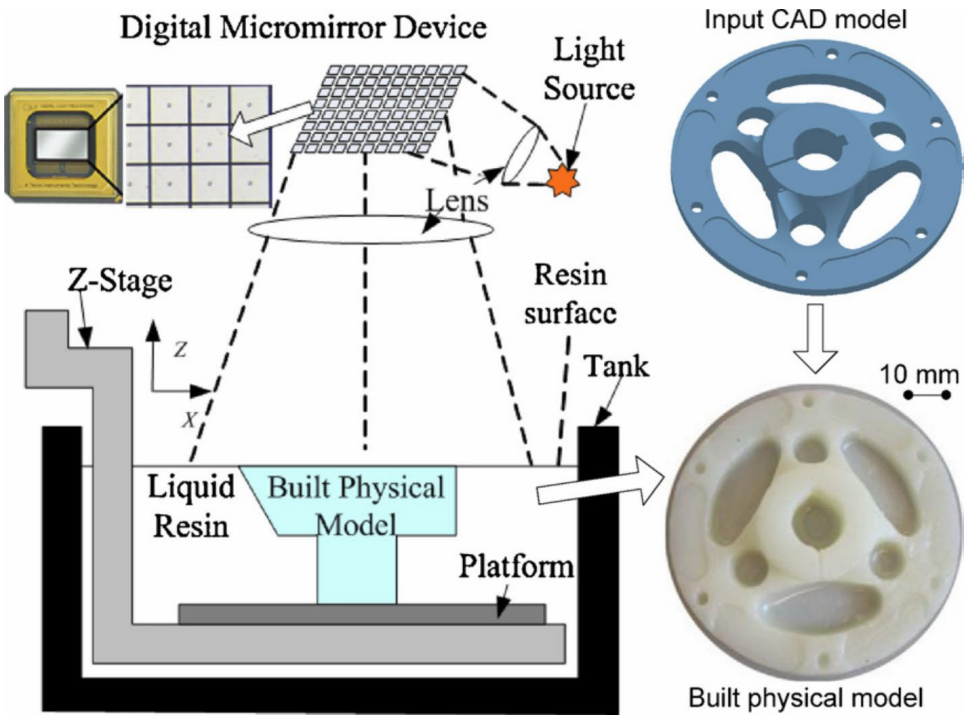

Figure 1.3 Schematic showing the process for DLP 3D printing. [24]

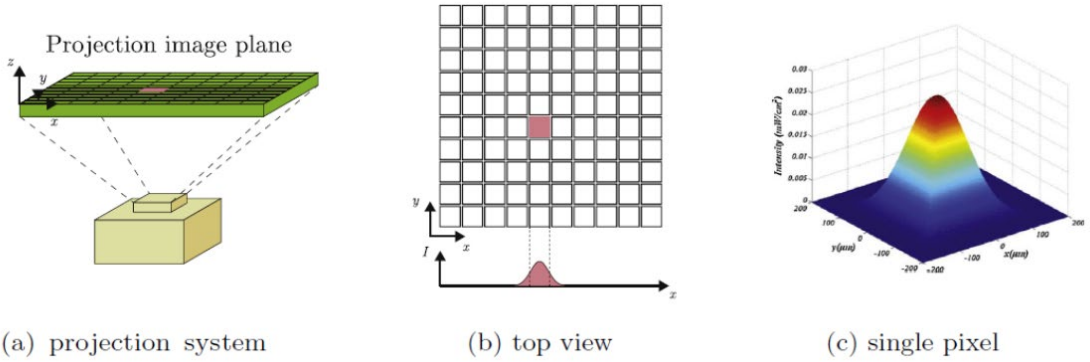

Figure 1.4 Typical light projection system setup for DLP 3D printing. (a) The projection system showing the projector at a fixed distance away from the projection plane with individual pixels shown. (b) The location of an example pixel with the corresponding profile of light intensity shown in 1D. (c) The full 2D Gaussian profile shown for illustrative purposes. [28]

1.1.4 Polymer Dissolution in Vitrimers

Polymer recycling is an attractive area of research due to the potential to reduce the harsh impact these materials have had on the environment over the last century. Typically, chemically crosslinked thermosetting polymers are difficult to dissolve, and thus recycle, due to their inability to melt upon curing. Many of the desirable properties of thermosetting polymers, such as excellent mechanical properties, good solvent, and chemical resistance, come from their strong and stable chemical crosslinking formed during curing. Compared to thermoplastics, thermosetting polymers can neither be melted upon heating nor be dissolved in a solvent, which makes them difficult to recycle. To alleviate the environmental impact of thermosetting polymer waste in landfills and incinerators, many different recycling approaches have been developed [29-31].

Recently, novel thermosetting polymers containing dynamic bonds (or vitrimer) and have been developed to achieve chemical recycling under mild conditions [32-40]. For

example, vitrimer proceeded dynamic exchange reactions which include thiol−disulfide/thioester exchange reactions [41-44], Schiff-base reversible reactions [45, 46], and transesterification reactions [47-52] with a reactive small molecule solvent, can be leveraged to achieve chemical recycling of thermosets at relatively mild conditions. When these thermosetting polymers are immersed in a solvent or solution, the diffusion of solvent into the network leads to selective and effective cleavage of the polymer chains. The polymer chains in the network can be gradually decomposed into short segments and finally be dissolved in the solution and recovered for future repolymerization. These novel polymers have also been successfully 3D printed [51] as shown in Figure 1.5. This novelty opens an avenue for sustainable 3D printing. To properly deploy such a method for sustainable 3D printing in industry a physics-based model is highly desirable to predict an average recycling time of a part for a given volume.

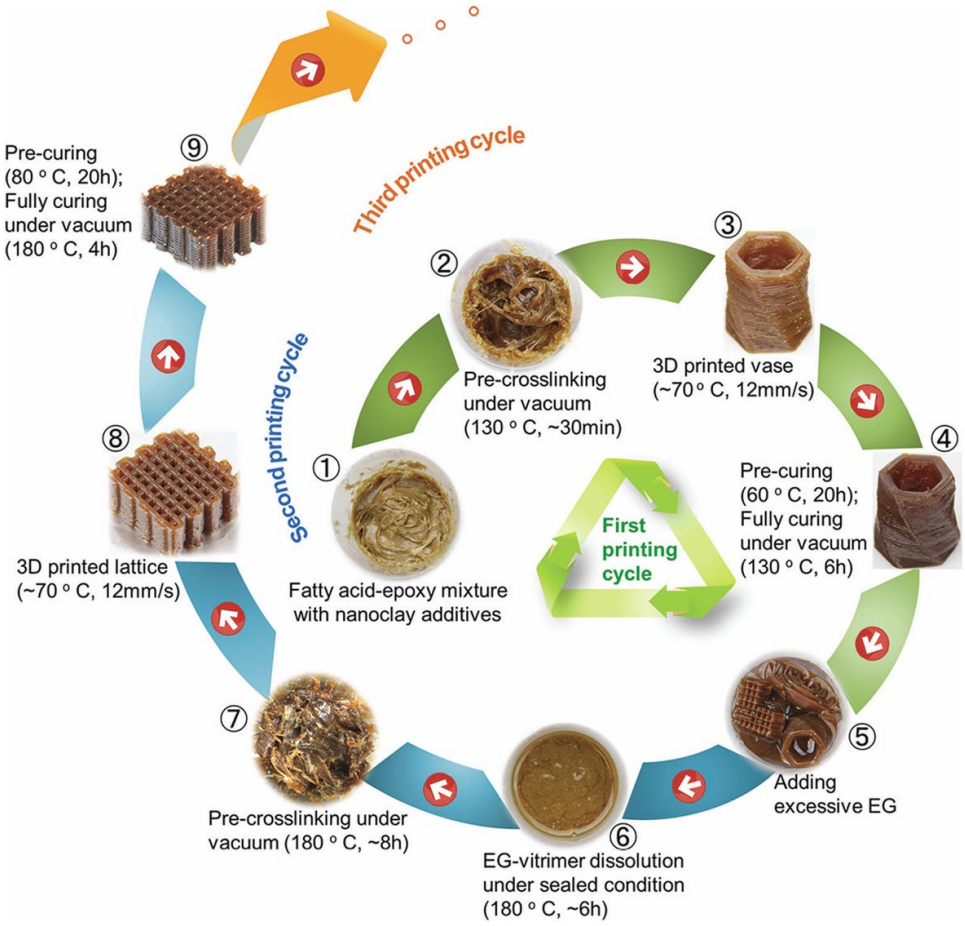

Figure 1.5 3D printing cycle of vitrimer with recyclability [51].

1.2 Outline of Included Work

This thesis research aims to consider modeling various parts of the typical life cycle of a 3D printed part spanning from design and conception through the fabrication and eventually the end of life of 3D printed components through dissolution considerations which have applications in recycling and reuse of materials. The research topics are divided into three parts. The first part is machine learning based design of material distributions for applications in soft active composites and 4D printing which is described in 0. The intention of this research is to fill in gaps present with current design optimization strategies for 4D printing in terms of the physics captured in such methods. The second research topic

discussed is modeling and simulating the species transport of chemical species present in the photopolymerization process during layer-by-layer fabrication of a structure in DLP 3D printing is discussed in **Error! Reference source not found.**. The objective of **Error! Reference source not found.** is to develop a material processing model currently lacking in the literature which accounts for spatial variation in the light intensity in DLP due to the DMD device and grayscale patterns along with incorporating the species transport of free radicals and other chemical species. The third topic is a model for dissolution of vitrimer thermosetting polymers is detailed in CHAPTER 4. This research aims to fill in the scarcity present in the literature for models pertaining to the dissolution of thermosetting polymers for applications in recycling of these materials which can often have a detrimental impact upon the environment. Finally, conclusions and plans for future work are discussed in CHAPTER 5.

CHAPTER 2. MACHINE LEARNING DESIGN FOR ACTIVE COMPOSITES

2.1 Machine learning design for a generalized active composite

The first portion of this research begins by exploring a new optimization paradigm for active composites to guide us on how to properly 3D print multi-material structures for 4D printing applications. Active composites are a class of materials that have environmentally responsive components within them. One key advantage of active composites is that through mechanics design, a variety of actuation can be achieved. The development of active composites has been significantly enhanced in recent years by multimaterial 3D printing where different materials can be precisely placed in 3D space, enabling the achievement of shape-shifting of 3D printed parts, or 4D printing. In practical applications, it is highly desirable that the part shape can change in a pre-described manner, which requires the careful design of where to place different materials. However, designing an active composite structure to achieve a target shape change is challenging because it requires solving an inverse-problem with spatially heterogenous, highly nonlinear (active) material behavior within a potentially complex boundary value problem.

In this chapter, we present a machine learning approach to the design of active composite structures that can achieve target shape shifting responses. Our strategy is to combine the finite element method with an evolutionary algorithm. In order to achieve a target shape, we compose the structures of equally sized voxel units that are made of either a passive or an active material and optimize the distribution of these two material phases.

The optimization method is tested against several illustrative examples in active composite design to show the agreement behind the target shape and the best solution obtained. The work presented in this chapter was published in *Smart Materials and Structures* [53].

2.1.1 Introduction

Active composites are a class of materials that have environmentally responsive components within a non-active matrix. The key ingredients to an active composite are an active material and a passive material. The passive material is usually compliant to allow for large actuation while the active material may be activated by different stimuli such as light, electricity, temperature, magnetism etc. Different classes of active materials include shape memory polymers [1], light active shape memory polymers [2], dielectric elastomers [3], liquid crystal elastomers [4, 5], as well as hydrogels [6, 7]. Upon an environmental stimulus, the responsive material undergoes actuation, but within the confinement of the non-active matrix. Therefore, the shape-change or the actuation depends on the spatial arrangement of active and non-active components in the composites. This imparts an advantage of active composites that through the layout design of active and passive phases throughout a structure, a variety of actuation responses can be achieved upon external stimuli. In the past, active composites were mainly conceptual as fabrication of these composites were very challenging. However, recent advances in additive manufacturing (or 3D printing) enable accurate placement of different materials in a single part. These improvements thus allow for the rapid design and manufacture of structures composed of active materials, which can add functionality to normally static mechanical components. This also leads to the term 4D printing [20, 21], which has potential applications in sensors, robotics, bio-medical applications, smart actuators, and MEMS devices.

In the applications of active composites, it is highly desirable that the shape change can occur in a predictable manner, or that the shape change can be achieved through careful design. However, this design process is difficult, as such a design involves a challenging inverse problem on a particular geometry and boundary value problem: For a given target displacement field (or shape), we must find the optimal spatial distribution of constituent materials. This inverse problem is often difficult because a solution may not exist, or it may not be unique, or the solution process can be unstable. Previous approaches to active composite design utilized topology optimization techniques such as level-set topology [22], linear elastic topology optimization [54], as well as trial and error approaches. However, most active materials achieve their active motion through multiphysics mechanisms, such as the coupling of solvent diffusion and mechanics, electromagnetic driven materials such as MEMS devices, and light active materials to name a few. These multiphysics mechanisms often introduce both material and geometric (large deformation) nonlinearities, which impede conventional gradient-based optimization strategies. Furthermore, the obtained results would only be applicable to one type of activation physics or constitutive relation. The discrete nature of voxel-based 3D printing methods also adds further difficulties to a traditional topology optimization approach. It has been previously discussed in the literature that such discrete approaches to topology optimization can be sensitive to variations in the parameters utilized within the algorithm [55]. A typical solution is to model the material distribution as continuous variables [56]. However, the downside is that a continuous material distribution does not accurately model the mechanism of accurately placing different materials in a discrete matter. A material and stimuli agnostic approach, which accurately models the manufacturing mechanisms, would

be highly desirable to the mechanics and smart materials community but proves to be a challenging and open problem.

Machine learning is gaining wide popularity in recent years across diverse fields due to the significant speed improvements, cost reductions, and parallelization in modern computer systems. Pioneering research in the field was originally conducted in the 1950's with simple statistical algorithms [57]. The sophistication of the field advanced during the 1960's but stagnated drastically in what is known as the "AI winter" during the 1970's due to doubts of the effectiveness of the algorithms. A resurgence of the filed occurred in the 1980's due to the discovery of backpropagation [58], which is a necessary ingredient in creating powerful modern neural networks. Research progressed during the next few decades with the advent of recurrent neural networks (RNNs) [59, 60] and support vector machines (SVMs) [61, 62] to name a few methods. There was also a major paradigm shift at this point where research switched from a knowledge-driven approach about the problem's researchers were trying to solve, to a data-driven approach where knowledge of the problem being solved was not necessary to obtain good results [63]. Although most of the methods and algorithms within the field are mature and well understood, they have only recently been applied to a diverse set of problems after the turn of the millennium due to improvements in computer hardware [64]. For example, convolutional neural networks (CNNs) have been utilized in image recognition [65] with great success in applications such as facial recognition [66] and computer vision [65]. Music and video streaming services [67] also widely use ML techniques to try and deduce what song (or movie) we may want to listen to (or watch) based on our previous choices [68]. Among the many classes of ML techniques and algorithms, evolutionary algorithms (EAs) are one class of

algorithms typically used for multi-objective optimization and combinatory problems. The main difference between EA and other techniques in ML is that parts of the algorithms in EA are inspired by evolutionary processes in nature. An EA attempts to replicate the evolutionary process of "survival of the fittest" in a computational setting and allows populations of solutions to "compete" with each other until the fittest solution prevails. EAs have been used in many different fields such as training AI in video games, an optimization method for training neural networks [69], and even recently has been used in composite design and other fields of mechanics. Examples of previous efforts to utilize ML/EA in engineering design include, reinforcement placement in composites [70], optimization of lattice structures [71], crucial aerospace component design [72], prosthetic optimization [73], among other interesting and challenging problems. Evolutionary approaches also have been used with FEM in engineering optimization problems previously [71, 74].

In this work we aim to expand upon the previous efforts in active composite design by incorporating material nonlinearity. We overcome the challenges in traditional topology optimization techniques by using the gradient free EA method. In addition, since each iteration in the EA involves evaluating the fitness of many individual simulations, the evaluation of a whole generation is naturally parallelizable across several computers. The organization of the work is as follows. The EA is briefly outlined along with the details of our parametric active composite model in section 2.1.2. To test our method, we subject it to three different optimization problems in section 2.1.3. This work concludes with a discussion of the results and concluding remarks in sections 2.1.4 and 2.1.5 respectively.

2.1.2 Methods

In this work, we consider the design of a simple active composite beam. Upon temperature change or a mechanical load, the beam changes into a target shape. The active composite consists of two materials. One is an active material and is responsible for the shape changing behavior and the other is a passive material which does not respond to the stimulus. Due to the different responses of the two materials to activation, the shape change is highly dependent upon the distribution of active and passive materials in the composite structure. Our design goal is to achieve a certain target shape by properly placing these two materials at different locations throughout the structure. Such designs can be easily achieved by multimaterial 3D printing. Depending on the complexity of the desired shape the distribution of active and passive material phases may be non-intuitive and difficult to predict. Our method for the design of the placement of active materials in active composites consists of two major components. The first is the EA which is the optimization component. The second part is the parametric FEM model that tests the candidate solutions produced during the optimization process to gauge whether one solution is better than one previously obtained.

2.1.2.1 Parametric Active Composite Design

In order to use EA, we first need to define the genome, the domain over which the EA optimizer will place the active and passive materials. The genome of our model simply consists of equally sized "voxel units" into which the active composite structure is spatially divided. The voxelization of the structure has the added benefit of being able to have additive manufacturing constraints (such as printing resolution in different directions) implicitly included within the optimization algorithm with no need for including these as additional constraints in the optimization problem. Each unit is represented by a "0" for

placement of the passive material in that location and a "1" for placement of the active material. Our model geometry is a 2D, cantilever beam under plane strain conditions. The beam is partitioned into 500 equally sized square voxels. An example of a candidate solution's genetic encoding is shown below in Figure 2.1. The digital representation of the active composite is known as a genotype in EA methodology, and the generated design is known as the phenotype, jargon with direct analogy to biological terminology.

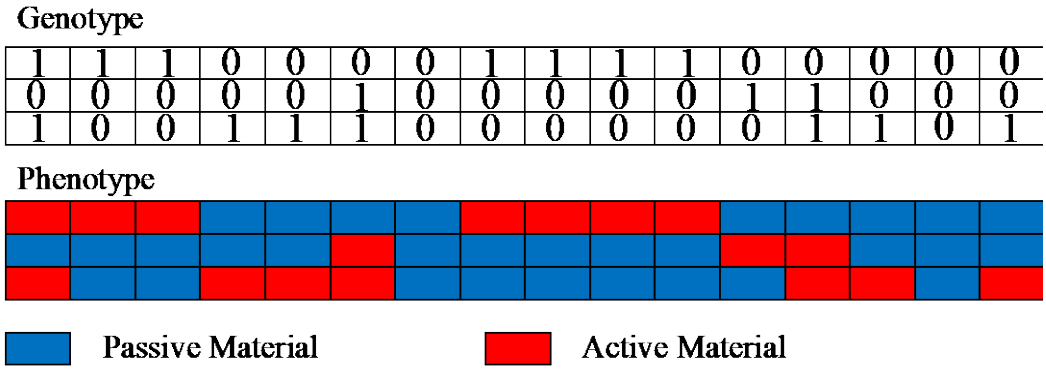

Figure 2.1 Illustrative schematic of our evolutionary algorithm encoding of our model problem. Red is used to represent active material and blue is used to represent passive material in the phenotype illustration above.

To illustrate the method, we utilized plane-strain simulations. The dimensions and meshing scheme for our parametric design are outlined in Table 2.1**.** The beam had a dimension of 50mm by 2.5mm. Each voxel was 0.5mm by 0.5mm for a total of 500 voxels. For FEM simulations, each voxel was meshed with 9 CPE4H element in the commercial software package ABAQUS (2018, SIMULIA, Providence RI), and thus the beam was meshed with a total of 4,500 elements. One advantage of EA is that it is conducted separately from the FEM calculations. Therefore, for any candidate simulations, although it was possible to conduct much more FEM simulations simultaneously, we ran eight FEM

simulations in parallel. This parallelization greatly reduced the time required to achieve a convergent solution.

Table 2.1 Parametric model parameters

Property	Value
Dimensions	50 x 2.5 mm
Voxel Size	0.5 x 0.5mm
Number of Voxels	500
Mesh Size	300 x 15
Reference Temperature	0
Heated Temperature	100

2.1.2.2 Evolutionary Algorithms

An EA is a randomized gradient-free optimization technique. Figure 2.2shows the flowchart in the EA. A typical EA consists of three major operations: selection, mutation, and crossover. In the beginning of the algorithm a population of μ candidate solutions are created and evaluated against the optimization criterion. In order to evaluate each member of the population a fitness function $\mathcal{F}$ must be defined. It is essentially a score of how well the candidate performs and is analogous to an objective function in traditional gradient-based optimization methods. Once the initial population is evaluated an offspring population of size λ is created based on selecting a portion of the best performing individuals from the parent population. Selection is comparable to Darwin's survival of the fittest concept and ensures that very bad solutions should not survive in subsequent

generations. At the end of each generation, every solution has a defined probability for being chosen for mutation, p_M, or crossover, p_C. The probability, p_S, for a member of the population to be selected for the next generation without modification is defined to be $p_S = 1 - p_M - p_C$. Due to the probabilistic nature of the selection process each generation can have a different number of individuals. The average size of a generation can be inferred to be $(1 - p_S)\lambda$. In the case of the parameters we used within this work our maximum offspring size is set to $\lambda = 100$ with $p_M = 0.3$ and $p_C = 0.5$. A simple calculation shows that for an average generation 80 FEM simulations were calculated and an average of 10 solutions were kept in the population without modification. The members that are not selected for survival to the next generation from the parent population are then allowed to mutate and crossover with each other. Mutation is analogous to biological mutation in DNA where a small change occurs in a random section of the genetic code. Since mutation is a randomized process it can take many generations for a desired mutation to occur with a potentially uncountable amount of combinations. Crossover is like reproduction in biology where genetic materials from two parents combine to create a new child which has features from both parents. The algorithm will iterate until a set number of generations, N_{gen}, has been reached or if a member of the population has a fitness function value that is less than (greater than) the tolerance ϵ_{tol}.

We used the open source python library DEAP (Distributed Evolutionary Algorithms in Python) [75, 76] due to its selection of EA algorithms and straightforward interface with the FEM software. The FEM simulations were carried out using built-in material models within ABAQUS. Each candidate solution was encoded into our material

placement convention (discussed later) which was then passed into an ABAQUS python script. The python script generates, runs, and post-processes a simulation based on the material distribution provided by the EA.

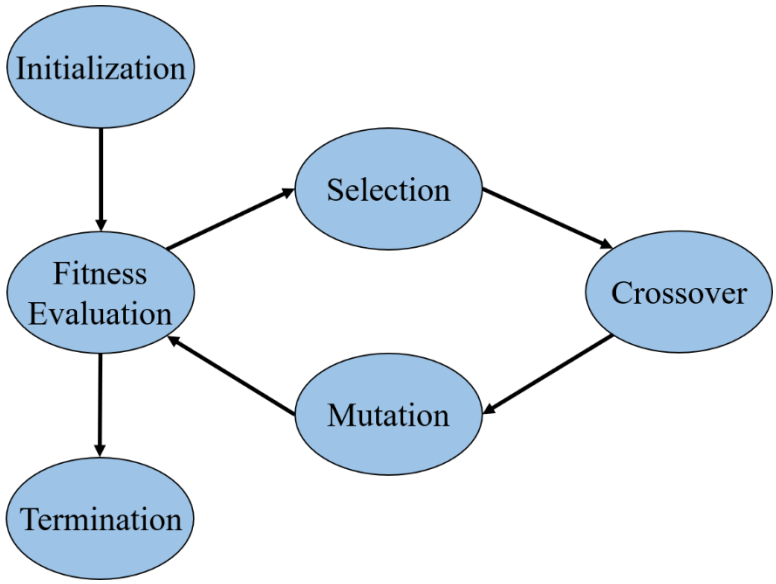

Figure 2.2 Information flow in a standard evolutionary algorithm

The DEAP reproduces a simple evolutionary rule [77]. In DEAP, crossover *or* mutation is applied to a solution but not both, which is done in other EAs. The crossover procedure takes features from two or more candidate solutions and combines them into a new candidate based on a scheme which can be problem dependent. We utilized a two-point crossover method, which chooses two points in the genetic encoding to "cross-breed" the parents into children. Figure 2.3shows an illustrative example of how two-point crossover works for our problem. Two "parent" solutions are chosen and two random points in the designs genetic encoding (represented by an array of 0s and 1s) are picked to split and then recombine into two new "children" solutions. Mutation within an EA is analogous to a search of the optimization space in traditional optimization methods. In the

case of EAs however this search is randomized rather than be directed by a gradient of the objective function. There are many different mutation methods, and the choice of the method can be highly problem dependent. In this work, a flip-bit mutation was used. Essentially this mutation works by assigning each feature in the genome a probability to be mutated. If that feature is chosen to be mutated, then in our case it flips a 1 to a 0 or vice-versa. The selection of good solutions is based upon the evaluation of an individual against the fitness function. Several strategies exist, but due to the algorithm, we utilized selection was based upon the NSGA-II algorithm [78]. The parameters that were utilized in the current work are shown in Table 2.2.

Table 2.2 Parameters for the evolutionary algorithm used in this work

Algorithm Parameter	**Symbol**	**Value**
Population Size	λ	25
Offspring population size	μ	100
Crossover Probability	p_C	0.5
Mutation Probability	p_M	0.3
Feature Mutation Probability	p_F	0.15

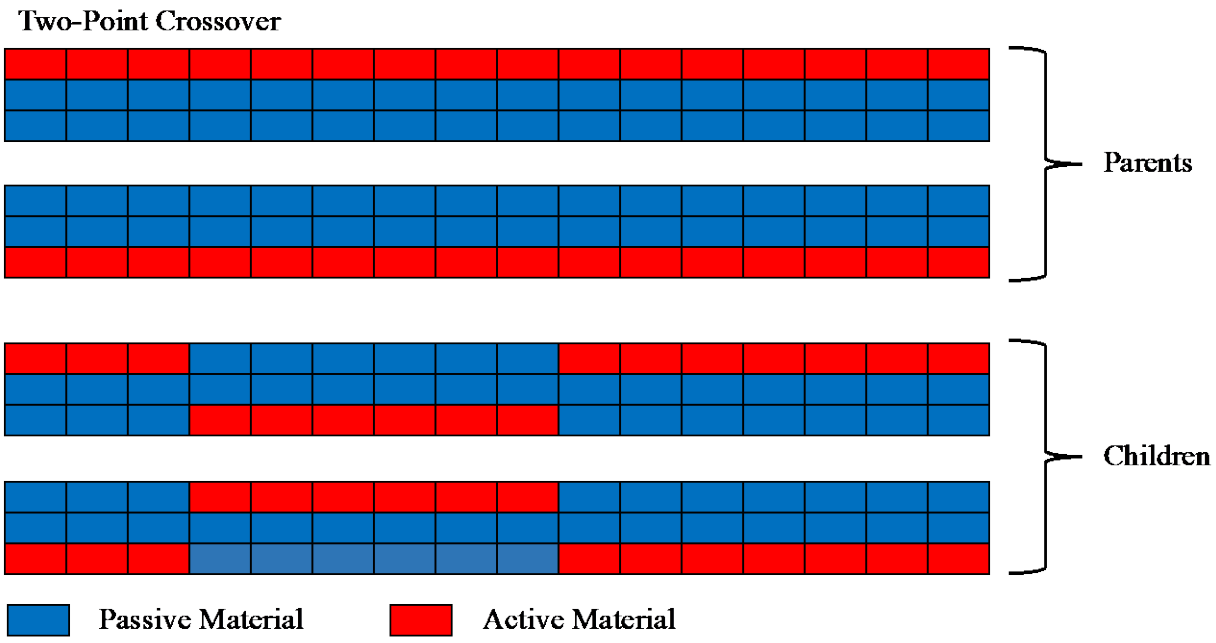

Figure 2.3 Illustrative schematic of two-point crossover for our method.

2.1.2.3 Material Model

In order to simplify the underlying FEM simulations, we use thermal expansion to mimic the active behavior of the active material. To show the strength of our method we utilized a finite strain simulation framework. In the case of concurrent deformation due to loading and thermal expansion, the total deformation gradient may be decomposed into thermal and mechanical components,

$$\mathbf{F} = \mathbf{F}^M \mathbf{F}^T, \tag{2.1}$$

where $\mathbf{F}$ is the total deformation gradient, $\mathbf{F}^M$ is the mechanical deformation gradient and $\mathbf{F}^T$ the thermal deformation, assuming isotropic thermal expansion, is defined as

$$\mathbf{F}^T = \lambda^T \mathbf{I}. \tag{2.2}$$

The thermal stretch, λ^T , in equation (2.2) is defined as

$$\lambda^T = 1 + \alpha \Delta T, \tag{2.3}$$

where α is the coefficient of thermal expansion (CTE) and ΔT is the change in temperature. For the present work we assume quasi-static and spatially uniform temperature conditions. In the absence of body forces, the quasi-static momentum balance is,

$$\text{div}\mathbf{T} = \mathbf{0}, \quad \mathbf{x} \in \Omega. \tag{2.4}$$

where $\mathbf{T}$ is the Cauchy stress. It is also necessary to supply boundary conditions for equation (2.4) which can be generalized as follows

$$\begin{aligned} \mathbf{u} &= \tilde{\mathbf{u}}, \quad \mathbf{x} \in \partial\Omega_{\mathbf{u}} \\ \mathbf{t} &= \mathbf{T}\mathbf{n}, \quad \mathbf{x} \in \partial\Omega_{\mathbf{t}} \end{aligned} \tag{2.5}$$

where $\tilde{\mathbf{u}}$ denotes the displacement boundary conditions on a general surface $\partial\Omega_{\mathbf{u}}$ and $\mathbf{t}$ denotes a traction force applied on a general surface $\partial\Omega_{\mathbf{t}}$. For the mechanical constitutive relation of each phase, we utilize a nearly incompressible Arruda-Boyce model [79], due to its highly nonlinear behavior, in both the active and passive phases of the composite. The Cauchy stress for this model is

$$\mathbf{T} = \mu J^{-5/3} \left(\frac{\lambda_L}{3\bar{\lambda}} \right) \mathcal{L}^{-1} \left(\frac{\lambda_L}{\bar{\lambda}} \right) \left[\mathbf{B} - \frac{1}{3} tr(\mathbf{B}) \mathbf{I} \right] + K \frac{1}{J} (J - 1) \mathbf{I}, \tag{2.6}$$

with $\mathbf{B} = \mathbf{F}\mathbf{F}^T$, $\bar{\lambda} = \sqrt{\frac{1}{3} tr(\mathbf{B})}$, and $J = \det \mathbf{F}$. In equations (2.6), $\mathcal{L}^{-1}$ is the inverse of the Langevin function which is given by

$$\mathcal{L}(\beta) = \coth\beta - \frac{1}{\beta}. \tag{2.7}$$

The material constants in equation (2.6) are the shear modulus, μ , the chain locking stretch, λ_L, and the bulk modulus, K. The values for these material properties that were used in the model problems are summarized in Table 2.3.

Table 2.3 Material properties for constitutive model

Property	**Symbol**	**Active Material**	**Passive Material**
Shear Modulus (MPa)	μ	5	0.5
Bulk Modulus (MPa)	K	1000	1000
Chain Locking Stretch	λ_L	5	5
Coefficient of Thermal Expansion	α	0.001	0

2.1.3 Results

To test our method, we designed three illustrative examples for target active composite functionality. In these problems, activation was achieved by the thermal actuation of the active phase. A temperature change of 100ºC was used in all problems considered. In the first two problems, no mechanical load was applied, and the two target shapes were a parabola and a sinusoid, respectively. In the third problem, in addition to temperature change, a mechanical load was applied at the free end with the target shape still being a sinusoid. Another goal for the third problem was to minimize the amount of

active material used. We added this additional goal to test the applicability of EA for multi-objective optimization problem.

For achieving a target general shape in a 3D problem, the general form of the fitness function can be expressed as follows,

$$\mathcal{F} = \frac{1}{N}\sum_{j=1}^{N}\sqrt{\sum_{i=1}^{3}\left(u_i^{target,j} - u_i^{actual,j}\right)^2}, \tag{2.8}$$

with N being the number of points along the mesh that were sampled for comparison. In this case the goal of the optimization problem is to minimize the error between the target displacement, $\mathbf{u}^{target}$, and the actual displacement, $\mathbf{u}^{actual}$, which can be expressed as

$$\min_{\mathbf{u}^{actual}} \mathcal{F} \tag{2.9}$$

In this work, the sampling points were the mesh points on the top surface of the FEM model.

2.1.3.1 Parabolic Shape

The goal here is to find the distribution of active material locations such that upon heating the simple composite beam will achieve a parabolic shape with large deflection to test our method against a nonlinear mechanics problem. Our goal can be expressed in terms of the y-displacement field. The fitness function for this model problem was meant to minimize the displacement field in the target shape and the actual simulated candidate solution which was given by the following equation

$$\mathcal{F} = \frac{1}{N}\sum_{j=1}^{N}\sqrt{\left(u_y^{target,j} - u_y^{actual,j}\right)^2}. \tag{2.10}$$

The target shape we chose to achieve was a parabola whose displacement field were defined as

$$u_y^{target} = -A\left(\frac{2x}{L}\right)^2, \quad 0 \le x \le L \tag{2.11}$$

with $A = 5mm$ and $L = 50mm.$ In this problem, the maximum deflection of the beam was 20mm, which was 40% of the total length of the beam, ensuring a finite deformation nonlinear problem.

The results for the evolutionary process are shown in Figure 2.4. Figure 2.4a shows the comparison of the targeted curve and the actual active shape of the composite beam, confirming an excellent agreement. The relative error throughout the specimen is also shown in Figure 2.4a, as well as the convergence properties are illustrated in Figure 2.4b. Typically, in EAs, the statistics of a generation's fitness function distribution is used as a measurement of the convergence of the algorithm. The maximum fitness is the worst solution in the current generation, the minimum is the best solution, and the average fitness function shows how well the population is performing overall. As an EA progresses the entire population will begin to converge to an optimal minimum, but not necessarily the global minimum. The final deformed shape compared to the initial undeformed shape is shown in Figure 2.4c. The evolution was continued for 25 generations to achieve agreement with less than 3% error through the geometry. This required roughly 2500 FEM simulations, run in parallel (8 simulations at a time) to greatly reduce simulation time,

throughout the process. The largest error in the actual displacement field of the solution is located at the end of the beam as can be seen towards the right of Figure 2.4a. The evolution converged on the final solution after about 10 generations and did not improve for the subsequent 15 generations which is clear from the minimum fitness function over all generations shown in Figure 2.4b.

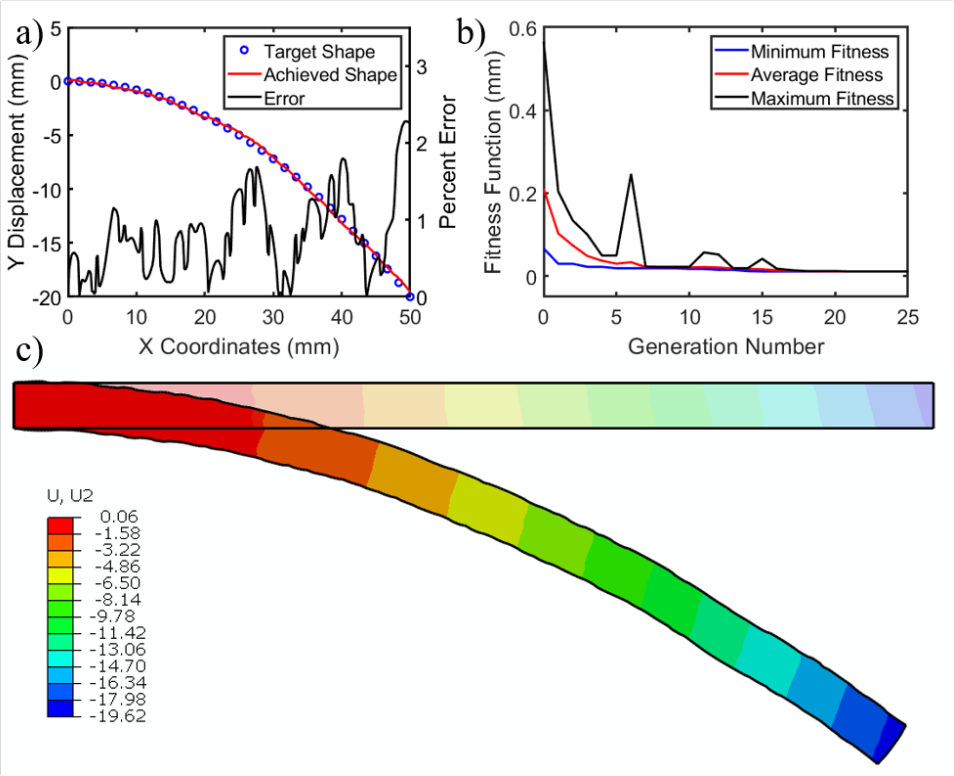

Figure 2.4 Results for parabola target shape problem. a) Agreement between target shape and best achieved individual throughout the evolutionary process (left y axis) as well as the error through the length of the geometry (right y axis). b) Convergence statistics for the evolutionary process. c) Final deformed shape plotted with the y displacement field with original undeformed shape as well.

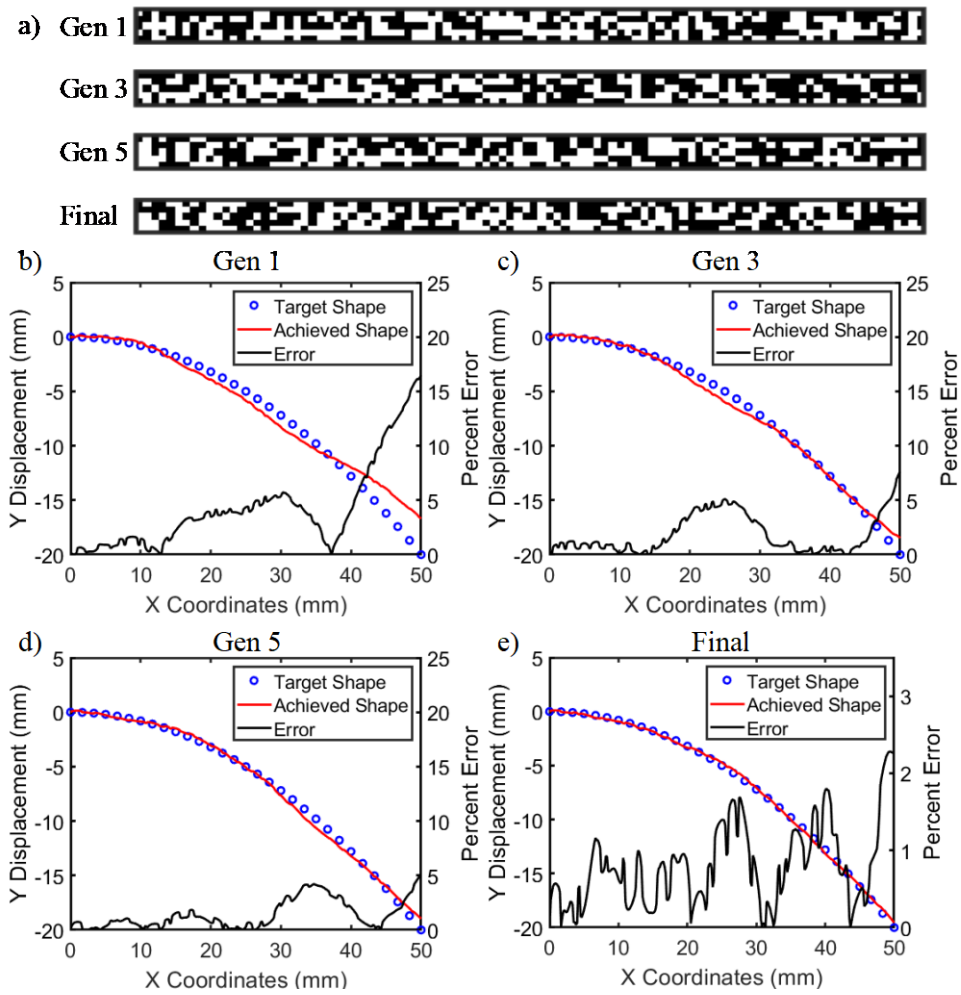

Figure 2.5 a) Evolution of material distribution and error through the length of the beam for the 1st generation, 3rd generation, 5th generation and the final result for the parabola problem. b) Comparison of target and achieved shape for the best individual in generation 1. c) Comparison of target and achieved shape for the best individual in generation 3. d) Comparison of target and achieved shape for the best individual in generation 5. e) Comparison of target and achieved shape for the final result.

The evolution of the material distribution and error through the length of the beam is shown in Figure 2.5. The best solution from 1st generation, 3rd generation, 5th generation and the final results are shown to illustrate the evolutionary process and difficulty to find similar features from generation to the next. As it can be seen the 5th generation already

showed a shape that was close to the target, indicating the rest of the generations became fine-tune the material distributions.

2.1.3.2 Sinusoidal Shape

In this section our aim is to achieve a sinusoidal shape. The fitness function was the same functional, equation (10), that was used in the previous section, but the target shape was different. The target shape in terms of the displacement field is given below

$$u_y^{target} = -B\left[1-\cos\left(\frac{\pi x}{L}\right)\right], \quad 0 \le x \le L \tag{2.12}$$

with $B = 5mm$ and $L = 50mm$. The maximum deflection in this problem is 10mm, ensuring the highly nonlinear problem. The results for the evolutionary process for this problem can be seen in Figure 2.6. The agreement between the target and achieved shape and error through the length of the beam is shown in Figure 2.6a with the greatest deviation being at the end of the beam like the previous problem. This problem had slightly larger error than for the case of the parabolic problem. For most of the geometry the error was 2% or less but at the end of the beam the error is as large as 4%. The best solution was achieved after about 10 generations and did not improve for the subsequent 15 generations, which can be seen in Figure 2.6b showing the minimum fitness function value for each generation. This also required roughly 2500 FEM simulations run in parallel to complete this process. The final simulated shape is shown in Figure 2.6c with the undeformed shape to showcase the large deformation.

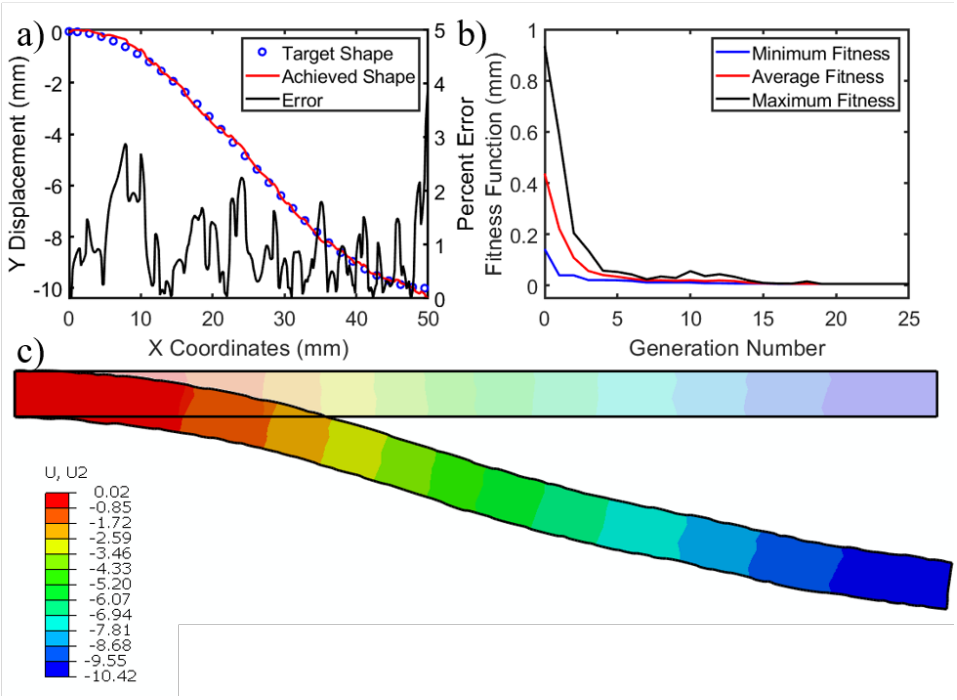

Figure 2.6 Results for sinusoid target shape problem. a) Agreement between target shape and best achieved individual throughout the evolutionary process (left y axis) as well as the error through the length of the geometry (right y axis). b) Convergence statistics for the evolutionary process. c) Final deformed shape plotted with the y displacement field with original undeformed shape as well.

Figure 2.7 shows the evolution of the active and passive material distribution, the agreement between the target and achieved shape, and the errors across the composite at different generations. It can be seen that the distribution of active and passive materials is highly non-intuitive. More active material is present where localized deformation is required depending upon the local curvature of the target shape that is trying to be achieved. In the case of the parabolic shape there is more active material towards the edges. On the other hand, for the sinusoidal target shape active material is more widely distributed in what seems like a random manner. The evolution of the material distribution is even more non-intuitive than the final distribution. Generation 1, 3 and 5 are shown because the best achieved individual in generation 2 was the same as in generation 1 as was true for

generation 3 and 4. It is interesting to note that throughout the evolutionary process the largest error in the active composite is always present at the free end of the beam where the deformation is maximized.

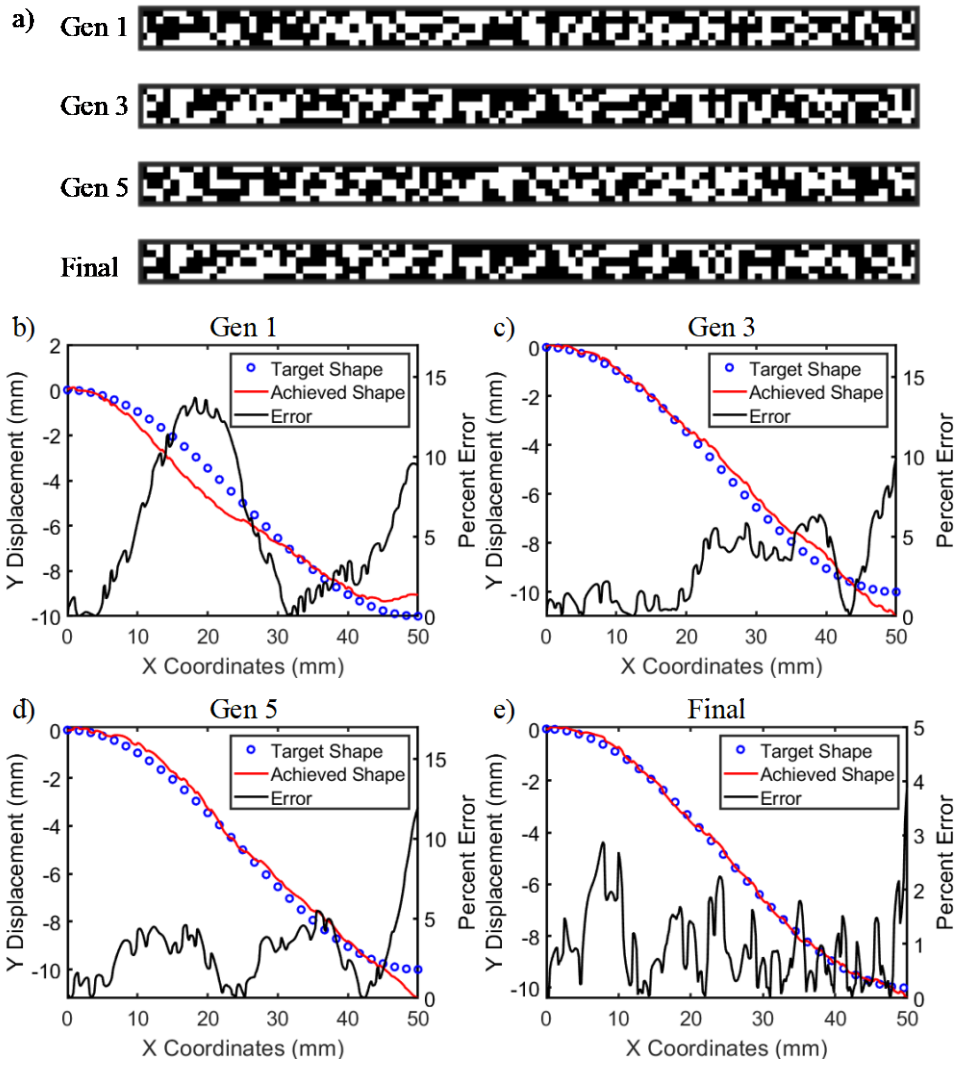

Figure 2.7 a) Evolution of material distribution and error through the length of the beam for the 1st generation, 3rd generation, 5th generation and the final result for the sinusoid problem. b) Comparison of target and achieved shape for the best individual in generation 1. c) Comparison of target and achieved shape for the best individual in generation 3. d) Comparison of target and achieved shape for the best individual in generation 5. e) Comparison of target and achieved shape for the final result.

2.1.3.3 Multiobjective Optimization Problem

In our last example problem, we chose a multi-objective optimization problem to show the extensibility of our method to a multiple constraint problem. This problem is similar to the one presented in the previous section where a sinusoidal shape is the desired activated and deformed shape. But here, we changed the boundary conditions by including a concentrated load at the end of the beam. In addition, we applied an additional constraint of minimizing the amount of active material needed to achieve the target. The same material properties were used as well as the same temperature change.

The multi-objective fitness function is now a matrix of functions rather than a single function. The first entry in this matrix is the fitness function that was used in the previous two sections, equation (2.10). The second part of the fitness function will be denoted by ρ which has the following form,

$$\rho = \sum_{i=1}^{N_{voxels}} \rho_i . \tag{2.13}$$

In equation (2.13) each ρ_i corresponds to the type of material present in the voxel. For simplicity we define this to be

$$\rho_i = \begin{cases} 1 & \text{if voxel i is active} \\ 0 & \text{if voxel i is passive} \end{cases} . \tag{2.14}$$

The complete fitness function is given below,

$$\begin{bmatrix} \mathcal{F} \\ \rho \end{bmatrix} = \begin{bmatrix} \sum_{i=1}^{n_{dim}} \sqrt{\left(u_i^{actual} - u_i^{target} \right)^2} \\ \sum_{i=1}^{N_{voxels}} \rho_i \end{bmatrix}. \tag{2.15}$$

The overall optimization problem can be expressed as

$$\min_{\mathbf{u}^{actual}, \rho} \begin{bmatrix} \mathcal{F} \\ \rho \end{bmatrix}. \tag{2.16}$$

The results for this problem are shown in Figure 2.8. The agreement between the target and achieved shape is shown in Figure 2.8a with good results. The error in this case is comparable to the second problem as shown on the right y axis of Figure 8a. The convergence statistics of the first entry of the fitness function is shown as dotted lines on the left y-axis in Figure 2.8b. The convergence statistics of the second entry of the fitness function is shown on the right y-axis of Figure 2.8b. The final deformed shape for this problem is shown in Figure 2.8c with the undeformed shape superimposed.

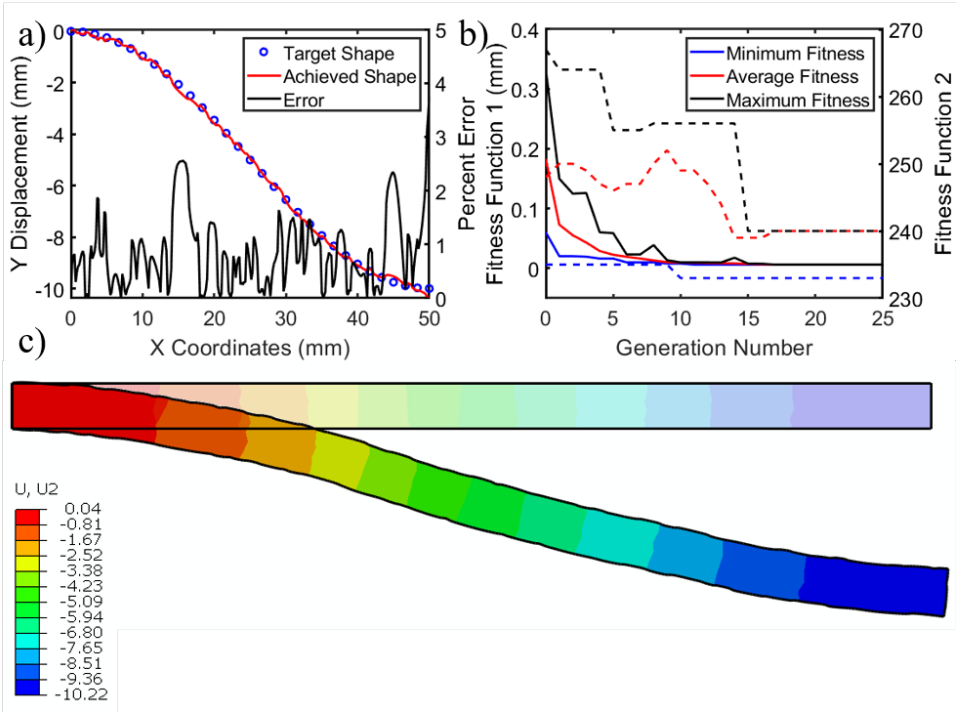

Figure 2.8 Results for multi-objective problem. a) Agreement between target shape and best achieved individual throughout out the evolutionary process as well as the error between target and achieved shape along the length of the beam. b) Convergence statistics for evolutionary process for the first constraint on the left y axis and the second constraint on the right y axis in dotted lines. c) Final activated shape with undeformed shape.

2.1.4 Discussion

Two different classes of inverse mechanics problems were optimized for active composite structure designs. The first class of problems involved targeting a certain shape for an active structure to achieve after evolution. The second class of problems involved different boundary conditions with the added constraint of minimizing the amount of active material in the structure to achieve a target shape after applying load. The second class of problems involved different boundary conditions as well as required a multi-objective fitness function.

Our examples demonstrate the advantages of using ML for design optimization of active composites. First, it does not require the calculations of the gradients of the objective functions, which can be a daunting job, especially, for materials or problems with nonlinearities. Second, the optimization method and the candidate simulation procedure are inherently decoupled, i.e. the objective function of the evolutionary process does not know what material model was used in our FEM model. This decoupling has an immediate advantage: it permits our method to be applied to many different active materials with widely different physical activation mechanisms without changing the optimization procedure; the only work that would be needed would be to create a parametric script that applies all the necessary boundary conditions, initial conditions, etc. In addition, this decoupling allows parallelization. Due to the limited number of ABAQUS licenses available to us, we only ran eight FEM simulations simultaneously, but much more FEM simulations could be conducted simultaneously shall this limitation be removed.

There is still room for improvement. As can be seen from the results in Figures Figure 2.4, Figure 2.6 and Figure 2.8, our method was able to achieve the target shapes well with marginal error in certain areas of the composite structure. The magnitudes of the errors present are on the order of a few voxels and could in theory be further minimized by using a finer voxelization procedure which would be analogous to a finer 3D printing resolution in production of such active composites. The simple DEAP method used in this work is very efficient. The parabolic and sinusoidal shape (with and without load) were both able to be achieved with a few percent error of the target shape. It should be noted that our parametric design has a large number of possible combinations, $2^{500} \approx 3.27 \times 10^{150}$, and our method was able to achieve a target shape on the order of 10^3 FEM simulations

which is infinitesimal compared to large possible combinations. However, we can imagine as more complex design problems are considered, the DEAP method might not be sufficient, but more complex and efficient algorithms, such as multi-population, evolutionary strategies, particle swarm optimization, etc., could be implemented.

Although using ML to design active composites has several advantages, we also observed several disadvantages. One typical problem with EA is the optimization process can be stuck in a local minimum which can be seen from the convergence plots in Figure 2.4, Figure 2.6 and Figure 2.8. Several generations of candidate solutions proceed without any improvement to the design, which can be thought of as a waste of computational time. It is also difficult to predict *a priori* how many generations may be necessary to solve a given optimization problem. Due to the randomized nature of the algorithm the designer could get faster results with a good population of solutions early in the evolutionary process or could have the disadvantage of generating many bad solutions for several generations. In addition, this work used a set idealized simple material property because the purpose of this work is to illustrate the feasibility of using ML for the design of active composites. Using real material parameters with complicated material constitutive behaviors may lead to some additional challenges, such as slower FEA runtimes, more complex constitutive relations, among other difficulties. Currently, we are working on using real 3D printed materials, with realistic constitutive behavior, for the design and the results will be reported in the future.

2.1.5 Conclusion

In this work we have introduced a machine learning based approach for the design of active composite structures by utilizing an evolutionary algorithm in conjunction with standard finite element method simulations. Simple geometries of active components were placed within a beam to achieve different target shape shifting upon heating. Good agreement between the target shapes and the final simulated shapes was achieved with reasonable error. It was also found that the distribution of the active phases was non-intuitive which further justified the need for a method such as the one presented in this work. The simple examples demonstrated in this work suggests that using the evolutionary algorithm has the potential to expand the design of active composite structures to consider nonlinear material models as well finite deformation, both of which are critical to active composite applications.

2.2 Machine learning design for active composites composed of amorphous shape memory polymers

There is currently great attention in the literature on the subject of 3D printing materials which possess the ability to change shape upon responding to its surrounding environment also known as 4D printing. In recent years, the abilities to fabricate such structures, by accurately placing different materials with pinpoint precision, has vastly opened up the design space for active structures and components. In order to make 4D printing a viable design paradigm in engineering applications, it is necessary to be able to predict the complex material response of 4D printed structures before, during, and after environmental stimulus. The complicated material behavior adds many challenges in design optimization which are not present with standard engineering material response. In 4D printing design we typically would like to find a distribution of different active and

passive materials such that a desired shape would be achieved during or after activation. This is contrary to a typical simulation problem in mechanics where a given material distribution is known a-prior and the accompanying displacements and/or stresses are of interest.

Our goal is to solve the inverse problem to find a given partitioning of different materials to achieve a desired displacement field upon activation. In this section a design approach grounded in machine learning to optimize material distributions in 3D printed active composites to achieve desired shape-shifting responses is presented. We utilize thermo-viscoelastic finite element simulations guided by genetic algorithms to achieve this goal. Our approach is tested against several examples and good agreement is obtained between the desired shape and the simulated examples. This work expands upon the methods presented in the previous section by incorporating non-linear inelastic materials models which were calibrated against experiments to represent real materials to further mature the use of machine learning in the design of material distribution for 4D printing.

2.2.1 Introduction

4D printing is an emerging design paradigm which integrates active materials with additive manufacturing (3D printing) technology to achieve printed parts that can occupy multiple configurations via a switching response driven by environmental stimulus such as heat [1, 4, 5, 14, 20, 80, 81], moisture [82, 83], or electromagnetism [84, 85]. Each activation strategy has strengths and weaknesses. For example, hydrogels have the advantage of not requiring programming following printing but their activation is driven by species diffusion [6, 86] which greatly slows the shape changing process. Shape

memory polymers (SMPs) on the other hand offer relatively fast response time but require a complex multi-step programming procedure after printing of a structure. This multi-step programming process along with inelasticity further complicates the design process compared to the idealized active composite presented in the previous section.

Shape memory composites are heterogeneous structures which may possess both active and passive material domains where the active domain is a material which possesses the shape memory effect and the passive material is typically compliant to allow for large deformations which accommodate large shape changes. The capabilities of modern 3D printing technologies allow for the ready fabrication of multi-material structures at the sub millimeter scale which opens an exciting design space for applications in 4D printing. The design of such composites is a challenging task of finding an ideal material distribution which consists of solving an inverse non-linear thermo-viscoelastic solid mechanics problem. Previous approaches to the design of shape memory composites included application specific design paradigms [1, 14, 20], topology optimization [22, 54, 55, 72, 74, 87], and most recently machine learning [53, 88, 89].

In this work our goal is to expand upon our previous efforts incorporating ML with FEM simulations to generate ideal material distributions for shape memory composites that can be readily printed using commercial 3D printers. The organization of the work is as follows. The optimization approach is described in section 2.2.2 followed by the underlying modelling assumptions and constitutive model used within each FEM simulation in section 2.2.3. The materials and experiments that were utilized for constitutive model calibration are discussed in section 2.2.4. Section 2.2.5 presents the results between desired shape upon

activation and the optimized design simulation results. The section ends with concluding remarks in section 2.2.6.

2.2.2 Methods

Within this work we utilize an EA which is a randomized gradient-free multi-objective optimization technique dating back decades. The major ingredients for using an evolutionary algorithm on a problem is a definition of an *individual* and the definition of a *fitness function* which is used to score the *individuals.* The individual is a representative solution for the problem trying to be solved. To simplify matters, candidate solutions are encoded in a *genotype* which is a string of numbers which act as a blueprint for how to build a fully representative individual, also known as a *phenotype.* An illustrative example of the domain with which our optimization procedure will iteratively assign materials is shown as a problem encoding is shown in Figure 2.9. To better model reality we have divided our design space into equally sized units consistent with the resolution of the printer described above. This assumption encodes the constraints a printer may have into the optimization problem explicitly without the need for additional goals to be defined in the optimization procedure. The results presented in this section used the same general workflow from the previous section. There were several small changes needed to the workflow for changing the material behavior response, but the details of the EA are exactly the same. The only change was the material model and material properties. These small number of changes necessary to change up the material further shows the novelty of this method. Unlike in topology optimization, there was no need to derive new numerical methods. Only changes to a few lines of code were necessary to change the problem considered.

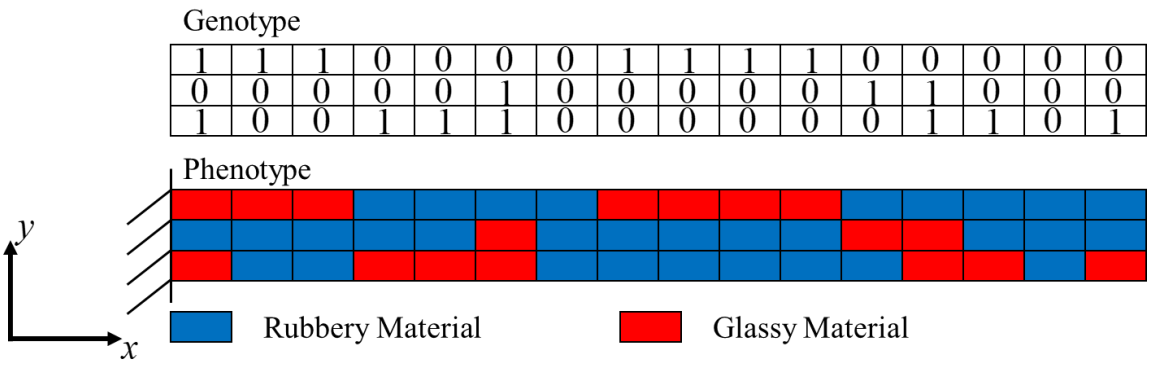

Figure 2.9 Schematic showing the genotype and phenotype encoding for the problem we are trying to solve. We divide the domain into a rubbery passive material which is compliant and does not exhibit the shape memory effect during typical operating temperatures and a glassy material which is stiff at room temperature but becomes compliant at elevated temperatures and exhibits the shape memory effect during operating temperatures.

Our fitness function aims to evaluate the difference between a simulated design's displacement field and the displacement field we wish to achieve. This can be defined using several different error metrics. Here we utilize a L_2 norm averaged over the nodal values which is expressed in equation form below,

$$\mathcal{F} = \frac{1}{N}\sum_{j=1}^{N}\sqrt{\sum_{i=1}^{3}\left(u_i^{target,j} - u_i^{actual,j}\right)^2}. \tag{2.17}$$

Specifically, we chose to utilize the $(\mu+\lambda)$ EA. The general execution of this type of EA is as follows. A population of μ individuals are initially created at random, but non-random initial guesses can also be inserted into this set if previous knowledge of the problem is already known. Each individual is then scored with the fitness function and organized based on the top performing members. This organization is from least to greatest value of the fitness function if the problem is a minimization and from greatest to least fitness function value if the problem is posed as a maximization. Upon evaluation of the

initial population a new generation of offspring of size λ are created based on selecting a small set of the best members of the parent population and allowing the remaining members to mutate and crossbreed. The selection acts as a pruning method to remove poor performing traits from the evolutionary process. Those individuals who are selected propagate to the next generation where they are not evaluated again due to the fitness value already being known from the current generation evaluation. Mutation and crossover act as search operations through the design space. The number of individuals which are selected, or undergo mutation and crossover is not predefined for each generation. This detail is handled in a probabilistic fashion. Each solution has a pre-defined probability for being chosen for selection, p_S, mutation, p_M, or crossover, p_C. These three probabilities sum up to one, i.e.

$$p_S + p_M + p_C = 1. \tag{2.18}$$

Therefore the three probabilities are not independent, so we can choose to pre-define p_M and p_C so that

$$p_S = 1 - p_M - p_C. \tag{2.19}$$

Since the three above mentioned EA operations are performed in a probabilistic fashion each generation can have a different number of individuals to evaluate fitness values for. The maximum size of a generation can never exceed λ but on average the number of individuals needing evaluation is $(1 - p_S)\lambda$. Therefore, the number of individuals allowed to survive into the next generation is $p_S\lambda$. Using similar reasoning it

can also be shown that on average the number of individuals which participate in mutation is $p_M \lambda$ and on average the number of individuals which participate in crossover is $p_C \lambda$.

The optimization proceeds iteratively through what are called *generations* where each individual of the population is evaluated with the fitness function. Simulations are run in parallel across a generation allowing for distributed computing solutions for large and complex problems. At the end of each generation, a portion of the best performing individuals are selected and allowed to undergo mutation and crossover. The algorithm terminates once a predefined error tolerance ϵ_{tol} has been achieved or if the number of generations exceeds a predefined maximum number of generation N_{gen}. More sophisticated termination criterion can be defined such as terminating if the standard deviation of the populations fitness value is too small, meaning each member of the population is too similar which will lead to many generations being exhausted without meaningful value to the increased design performance.

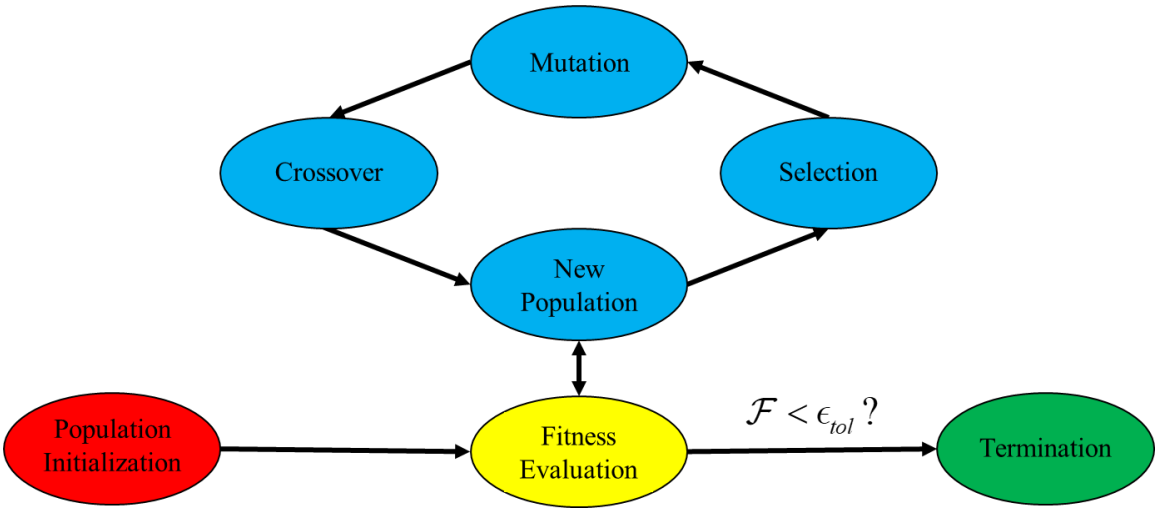

Figure 2.10 Flowchart showing the general flow of information during an execution of the EA. An initial population is created, and each individual's fitness is evaluated

using the defined fitness function. If the minimum fitness value is not less than the pre-defined error tolerance the population enters the loop over generations where selection, mutation, and crossover work in unison to create a new population. The cycle continues until the termination criterion are met.

Implementation of our method was carried out in the open source python library DEAP (Distributed Evolutionary Algorithms in Python) [75, 76] due to its ease of use of many different EA algorithms. The FEM simulations were carried out using built-in thermo-viscoelastic material models within ABAQUS. DEAP handled the generation of candidate solutions which were then passed into the fitness function. Our fitness function consisted of transferring the candidate solution's genotype to an ABAQUS python script which decoded the genotype into a phenotype by constructing the geometry, assigning material and boundary conditions, and running the simulation. The variables of interest were then post-processed from the Abaqus simulation and passed back to DEAP to assign a fitness value to that individual.

DEAP reproduces several classical evolutionary rules [77], one of which was utilized in this work. The specific EA operations that were utilized in DEAP are as follows. We utilized a two-point crossover method, which chooses two points in the genetic encoding to "cross-breed" the parents into children. In this work, a random integer mutation was used to accommodate for more than two potential materials, even though only two materials were considered in the results to be presented. Essentially this mutation works by assigning each feature in the genome a probability to be mutated, if selected the algorithm changes the encoded feature number based on a randomly selecting an integer from a set of possible integer values. The selection operation we chose was the NSGA-II algorithm [78] due to its ability to handle multi-objective optimization problems.

2.2.3 Constitutive Model

To accurately describe the materials, we use a thermo-viscoelastic multi-branch constitutive model to capture the shape memory cycle of the printed polymers. In this section we describe the underlying large deformation kinematics present within each FEM simulation and the underlying constitutive model and assumptions.

To describe the thermomechanical behavior of active and passive materials, a multi-branch model viscoelastic model is utilized, in which one equilibrium branch (which is present to carry long term load, otherwise the material model would describe a polymer melt) and several thermoviscoelastic nonequilibrium branches which are arranged in parallel. Maxwell elements are used in the nonequilibrium branches to represent the relaxation behavior of the material, which are composed of a spring and dashpot arranged in series. The relaxation times shift based on the temperature. Lower temperatures lead to longer relaxation times and vice versa.

Since the material model utilized is in a large deformation setting, we begin by discussing the deformation gradients. Here we represent the total deformation gradient as $\mathbf{F}$ defined below as follows,

$$\mathbf{F} = \frac{\partial \mathbf{x}}{\partial \mathbf{X}}, \tag{2.20}$$

where $\mathbf{X}$ is a point in the initially undeformed material configuration and $\mathbf{x}$ is a point in the deformed spatial configuration. Under the assumption of concurrent thermal and mechanical deformation the total deformation gradient $\mathbf{F}$ may be multiplicatively split into

a mechanical and thermal deformation gradient denoted by $\mathbf{F}_M$ and $\mathbf{F}_T$ respectively. Equation (2.20) then simplifies to

$$\mathbf{F} = \mathbf{F}_M \mathbf{F}_T, \tag{2.21}$$

where we assume that the thermal expansion is isotropic enforcing the thermal deformation gradient to be a spherical and isotropic tensor which can be expressed as

$$\mathbf{F}_T = \lambda_T \mathbf{I}. \tag{2.22}$$

In equation (2.22) λ_T is the thermal stretch which may be calculated readily from the change in temperature as

$$\lambda_T = 1 + \alpha\left(T - T_{ref}\right), \tag{2.23}$$

where α is the coefficient of thermal expansion (CTE), T is the current temperature, and T_{ref} is the reference temperature. Another useful quantity to introduce is the distortion deformation gradient. This is represented by

$$\overline{\mathbf{F}} = J_M^{-1/3} \mathbf{F}_M, \tag{2.24}$$

where $J_M = \det \mathbf{F}_M$.

A quasi-static assumption will be taken throughout, and non-uniform temperatures will be neglected in the work for the sake of speeding up each individual FEA simulation. If we further neglect body forces the balance of linear momentum is then simply

$$\mathrm{div}\mathbf{T} = \mathbf{0}, \quad \mathbf{x} \in \Omega, \tag{2.25}$$

where $\mathbf{T}$ is the Cauchy stress. To keep things general the boundary conditions may be represented as

$$\begin{aligned} \mathbf{u} &= \tilde{\mathbf{u}}, \quad \mathbf{x} \in \partial\Omega_{\mathbf{u}}, \\ \mathbf{t} &= \mathbf{T}\mathbf{n}, \quad \mathbf{x} \in \partial\Omega_{\mathbf{t}}, \end{aligned} \tag{2.26}$$

where we allow for both displacement boundary conditions, $\tilde{\mathbf{u}}$, on the surface $\partial\Omega_{\mathbf{u}}$ and traction forces, $\mathbf{t}$, on the boundary $\partial\Omega_{\mathbf{t}}$. The boundary conditions specific to each example shown later in the work will be presented where relevant. As for the prescription of the mechanical constitutive model, which accounts for the Cauchy stress $\mathbf{T}$ is equations (2.25) and (2.26), for each material we utilize the built-in multi-branch viscoelastic model within ABAQUS. The model consists of a single equilibrium branch, which accounts for the elastic equilibrium response of the materials, and several non-equilibrium branches containing Maxwell elements connected in parallel which account for the viscous dissipation in the materials. The total stress can be decomposed into elastic and viscoelastic contributions. For the equilibrium branch contribution, we utilized a neo-Hookean constitutive model to account for large elastic deformation.

$$\mathbf{T}_0 = G_0 J_M^{-5/3}\left[\mathbf{B}_M - \frac{1}{3}tr\left(\mathbf{B}_M\right)\mathbf{I}\right] + K_0\frac{1}{J_M}\left(J_M - 1\right)\mathbf{I}, \tag{2.27}$$

where $\mathbf{B}_M = \mathbf{F}_M\mathbf{F}_M^T$, G_0 is the equilibrium shear modulus, and K_0 is the equilibrium bulk modulus. This can be converted to the Kirchhoff stress with the following relationship (which will become useful momentarily)

$$\boldsymbol{\tau}_0 = J\mathbf{T}_0. \tag{2.28}$$

Substitution of (2.27) into (2.28) gives the following form for the equilibrium branch Kirchhoff stress

$$\boldsymbol{\tau}_{\mathbf{0}} = G_0 J_M^{-2/3}\left[\mathbf{B}_M - \frac{1}{3} tr\left(\mathbf{B}_M\right)\mathbf{I}\right] + K_0\left(J_M - 1\right)\mathbf{I}. \tag{2.29}$$

The total Kirchhoff stress in the equilibrium branch can be split into deviatoric and hydrostatic components using the following relation

$$\boldsymbol{\tau}_0 = \boldsymbol{\tau}_0^D + \boldsymbol{\tau}_0^H, \tag{2.30}$$

where the deviatoric portion is

$$\boldsymbol{\tau}_0^D = G_0 J_M^{-2/3}\left[\mathbf{B}_M - \frac{1}{3} tr\left(\mathbf{B}_M\right)\mathbf{I}\right], \tag{2.31}$$

and the hydrostatic contribution is

$$\boldsymbol{\tau}_0^H = K_0\left(J_M - 1\right)\mathbf{I}. \tag{2.32}$$

A reduced form of the model present within ABAQUS was utilized by enforcing the following assumption of incompressibility of the inelastic mechanisms which is often utilized assumption in both viscoelasticity and plasticity [90, 91]. The hydrostatic contribution of the total Kirchhoff stress at all times t is then simply

$$\boldsymbol{\tau}^H\left(t\right) = \boldsymbol{\tau}_0^H\left(t\right). \tag{2.33}$$

The update of the total deviatoric contribution of the Kirchhoff stress within ABAQUS is an implementation of the model due to Simo [92]. This total deviatoric Kirchhoff stress at any time t can be calculated as follows

$$\boldsymbol{\tau}^D\left(t\right) = \boldsymbol{\tau}_0^D\left(t\right) + dev\left[\int_0^{\tau} \frac{\dot{G}\left(\tau'\right)}{G_0} \overline{\mathbf{F}}_t^{-1}\left(t - t'\right)\boldsymbol{\tau}_0^D\left(t - t'\right)\overline{\mathbf{F}}_t^{-T}\left(t - t'\right) d\tau'\right] \tag{2.34}$$

where $\dot{G}\left(\tau'\right)$ is the time dependent shear modulus and $\overline{\mathbf{F}}_t$ is the distortion deformation gradient at time t. The time dependent shear modulus has the following representation

$$\dot{G}\left(\tau^{'}\right)=\frac{dG\left(\tau^{'}\right)}{d\tau^{'}}, \tag{2.35}$$

where $\tau^{'}$ represents a reduced time due to a shift in time with temperature that may be equated to the current time using the following relationship

$$d\tau^{'}=\frac{dt^{'}}{a^{shift}\left[T\left(t^{'}\right)\right]}. \tag{2.36}$$

In equation (2.36) a^{shift} denotes the shift factor, to be introduced below, and T is the current temperature. The time dependent modulus may be expanded using the following relationship

$$G\left(\tau\right)=G_0\left(g_\infty+\sum_{m=1}^{N}g_m e^{-\tau/\tau_m}\right), \tag{2.37}$$

where g_m and τ_m the relative modulus and relaxation time for the m^{th} branch and g_∞ is the instantaneous modulus. The relative branch modulus and the instantaneous modulus must satisfy the following the relationship

$$g_\infty+\sum_{m=1}^{N}g_i=1, \tag{2.38}$$

where N is the number of branches.

Based on the time temperature superposition principle (TTSP), the relaxation times τ_m can be calculated at the current temperature based on the relaxation time τ_m^R at the reference temperature as follows

$$\tau_m\left(T\right)=a^{shift}\left(T\right)\tau_m^R, \tag{2.39}$$

where $a^{shift}(T)$ is the temperature dependent shifting factor. To calculate the shifting factors we combine the Williams-Landel-Ferry (WLF) equation [93] and an Arrhenius type equation. When the temperature is above the reference temperature T_{ref}, the shifting factor is calculated using the WLF equation

$$\log_{10}[a^{shift}(T)] = -\frac{C_1(T - T_{ref})}{C_2 + (T - T_{ref})}, \quad T > T_{ref}, \tag{2.40}$$

where C_1, C_2, and T_{ref} are the material parameters which are characterized by experiment. If the temperature is below the reference temperature, T_{ref}, then the shifting factor is calculated using an Arrhenius type equation

$$\ln[a^{shift}(T)] = -\frac{AF_c}{k}\left(\frac{1}{T} - \frac{1}{T_{ref}}\right), \quad T < T_{ref}, \tag{2.41}$$

where A, F_c, and k are a fitting parameter, configurational energy, and Boltzmann's constant respectively.

Within the multi-branch linear model, the temperature dependent storage modulus can be represented as

$$G_s(\omega, T) = G_{eq} + \sum_{m=1}^{n} \frac{G_m^{non}\omega^2\left[\tau_m(T)\right]^2}{1 + \omega^2\left[\tau_m(T)\right]^2}, \tag{2.42}$$

and the loss modulus can be expressed as

$$G_l(\omega,T)=\sum_{m=1}^{n}\frac{G_m^{non}\omega\tau_m(T)}{1+\omega^2\left[\tau_m(T)\right]^2}. \tag{2.43}$$

In equations (2.42) and (2.43) ω is the angular frequency ($\omega=2\pi f$) and G_m^{non} are the non-relative branch moduli. One further useful relationship is

$$\tan\delta(\omega,T)=\frac{G_l(\omega,T)}{G_s(\omega,T)}, \tag{2.44}$$

which can be used to quantify the glass transition temperature of the polymer.

2.2.4 Material Characterization and Constitutive Model Calibration

The materials used in this work were fabricated using an Objet 3D printer (Objet 260). This printer is a PolyJet based 3D printer which has three main materials present. There are two base materials which are mixed to achieve different material properties and the third is a support material for printing complex structures where support is necessary for good geometrical accuracy. The two base materials are Tangoblack and Verowhite. Tangoblack is a rubbery material at room temperature and Verowhite is a glassy material at room temperature. Other materials may be printed by selecting predefined material mixtures in the printer's software to achieve properties in between the rubbery and glassy base materials. For this study we utilized Tangoblack as the passive matrix material and DM9895 (Grey60) as the active material.

Dynamic mechanical analysis (DMA) tests are performed on a DMA machine (model Q800, TA Instruments Inc, New Castle, DE, USA) in film tension mode. The material samples (dimension 10 mm × 6 mm × 2 mm) are first heated to 90 °C (60 °C for

the matrix material) and stabilized for 10 minutes to reach thermal equilibrium. Then the temperature is decreased from 90 °C (60 °C for the matrix material) to −30 °C (−50 °C for matrix material) with a cooling rate of 2 °C/min. A preload of 0.001N is applied to keep the sample straight during the test. During the DMA tests, the strain is oscillated at a frequency of 1 Hz with peak amplitude of 0.1%. The experimental data during the cooling step are used to determine the glass transition temperature of the passive matrix and active material. The results for the DMA sweep are shown in Figure 2.11. The temperature dependent storage modulus of the two materials are shown in Figure 2.11a and the Tanδ curves are shown in Figure 2.11b. The glass transition temperature of the passive matrix material was determined to be -3°C and the glass transition temperature of the active material was determined to be 54°C.

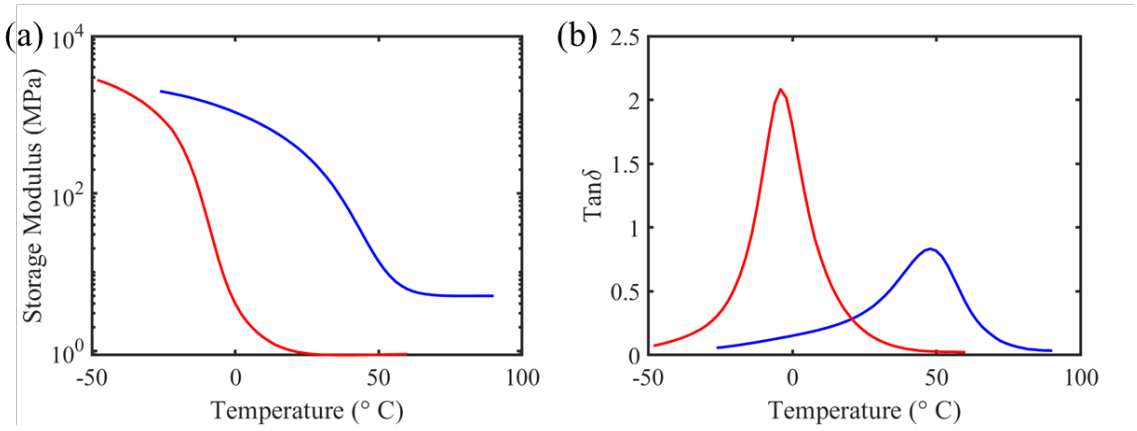

Figure 2.11 DMA temperature sweeps for the active and passive material. (a) Temperatuer dependent storage modulus with the passive material plotted in red and the active material plotted in blue. (b) Temperature dependent Tanδ with the passive material plotted in red and the active material plotted in blue.

The two materials were further characterized by performing a DMA frequency sweep for master curve fitting and determination of Prony series moduli and relaxation times. The samples were first heated to 60°C for the passive material and 100°C for the

active material, respectively. After holding the samples at a fixed temperature, the samples were then oscillated at a set number of frequencies (0.2Hz, 0.5Hz, 1Hz, 2Hz, 5Hz, 10Hz, and 20Hz) to determine the frequency dependent storage modulus at that temperature. This procedure was repeated at several temperatures ranging from 60°C to -50°C for the passive material and from 100°C to -10°C for the active material. The curves were then shifted with the aid of built in TA data analysis software to generate the experimentally determined storage modulus master curve and shift factor. The results for the storage modulus for the active and passive material are shown in Figure 2.12a and Figure 2.12c with the fitted master curve, using equation (2.42). The shift factor was then fitted using equations (2.40) and (2.41). The comparison between the experimentally determined and fitted shift factor for both the passive and the active material are shown in Figure 2.12b and Figure 2.12d respectively.

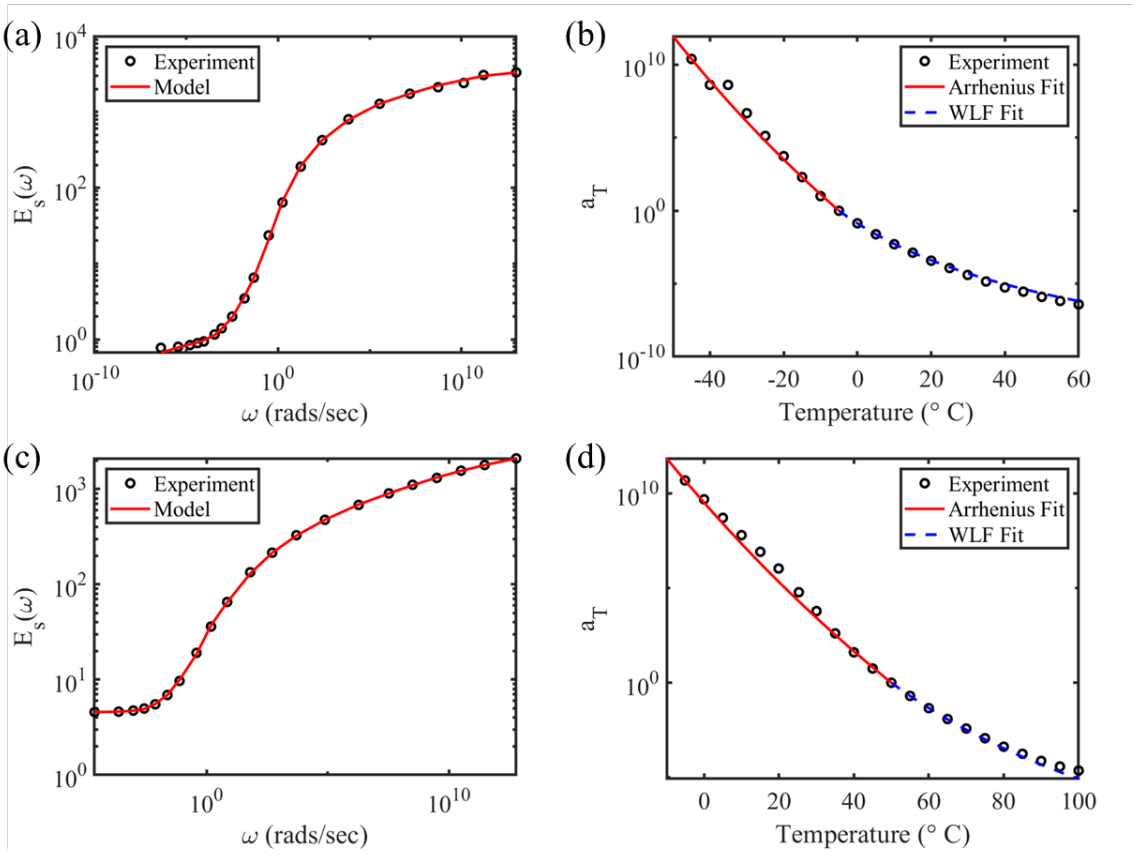

Figure 2.12 Results of the DMA frequency sweeps used for model calibration. (a) Master curve for the passive material's storage modulus. (b) Fitted shift factor for the passive material showing both the Arrhenius and WLF fit. (c) Master curve for the active material's storage modulus. (d) Fitted shift factor for the active material showing both the Arrhenius and WLF fit.

2.2.5 Results

As a verification of our method we conducted several design problems analogous the ones presented in the previous section of this chapter. The main active composites design problem that was explored is that of shape-fixing in shape memory polymer composites. Shape fixing is the process where we wish to achieve a target shape after applying a programming strain at an elevated temperature (above the glass transition temperature of the active material) and releasing the pre-applied strain at lowered

temperatures (below the glass transition temperature of the active material but above the glass transition temperature of the passive material). By this we mean the composite is initially heated, such that the active domain is above its T_g, and strained to a programming strain where it is subsequently cooled to a temperature below the active phase's T_g. The load is then released. Tangoblack and Grey60 were utilized as the passive and active material, respectively. Grey60 has a T_g of roughly 54°C while Tangoblack has a T_g well below room temperature. The boundary conditions for the straining step of the programming are as follows

$$\begin{aligned} u_x(0,y) &= 0, \quad u_x(L,y) = \varepsilon_{programming} L, \\ u_y(0,0) &= 0, \quad u_y(L,0) = 0, \end{aligned} \tag{2.45}$$

where u_x and u_y are the x and y displacements respectively, L is the length of the beam, and $\varepsilon_{programming}$ is the programming strain applied to the right end of the beam. After cooling the material the boundary conditions listed in equation (2.45) are released.

We optimized two different material distributions for this boundary value problem using two different target displacement functions. The first was a simple parabolic shape and the second was a sinusoidal shape such that a simple change in curvature problem could be addressed. The functional form for the parabola is given by

$$u_y^{target} = -A\left(\frac{2x}{L}\right)^2, \quad 0 \le x \le L, \tag{2.46}$$

where L is the length of the beam and A is the amplitude of the parabola. The results for the parabolic shape are presented in Figure 2.13. The material distribution that performed

optimally is shown in Figure 2.13a (only the right half of the material distribution is shown) where it can be seen that that the material distribution is highly nonintuitive and the middle portion has almost zero active material. It should be noted that this shape is rather simple to achieve since it is a function of constant curvature. The final simulation results with the y-displacement plotted is shown in Figure 2.13b with a comparison between the analytic function and the simulation results shown in Figure 2.13d where it can be seen that relatively good agreement is seen except for at the end of the beam where the largest displacement is present. The convergence properties of this material distribution evolution are shown in Figure 2.13c where it can be seen that the algorithm achieves very good agreement with the target analytic function after about 10 generations with further refinement of the distribution until terminating after 20 generations.

The functional form for the sinusoidal shape is

$$u_y^{target} = -B\left[1-\cos\left(\frac{\pi x}{L}\right)\right], \quad 0 \le x \le L, \tag{2.47}$$

where B is the amplitude and again L is the length. The results for the sinusoidal shape are shown in Figure 2.14. The material distribution that performed optimally is shown in Figure 2.14a (only the right half of the material distribution is shown) where it can be seen that that the material distribution is highly nonintuitive and the middle portion has alternating regions between active and passive material phases. This shape is a bit more complex the parabolic shape because it does not have a constant curvature. The final simulation results with the y-displacement plotted is shown in Figure 2.14b with a comparison between the analytic function and the simulation results shown in Figure 2.14d where it can be seen that relatively good agreement is seen except for parts of the beam in

the middle where curvature is changing. The convergence properties of this material distribution evolution are shown in Figure 2.14c where it can be seen that the algorithm achieves very good agreement with the target analytic function after about 10 generations with further refinement of the distribution until terminating after 20 generations.

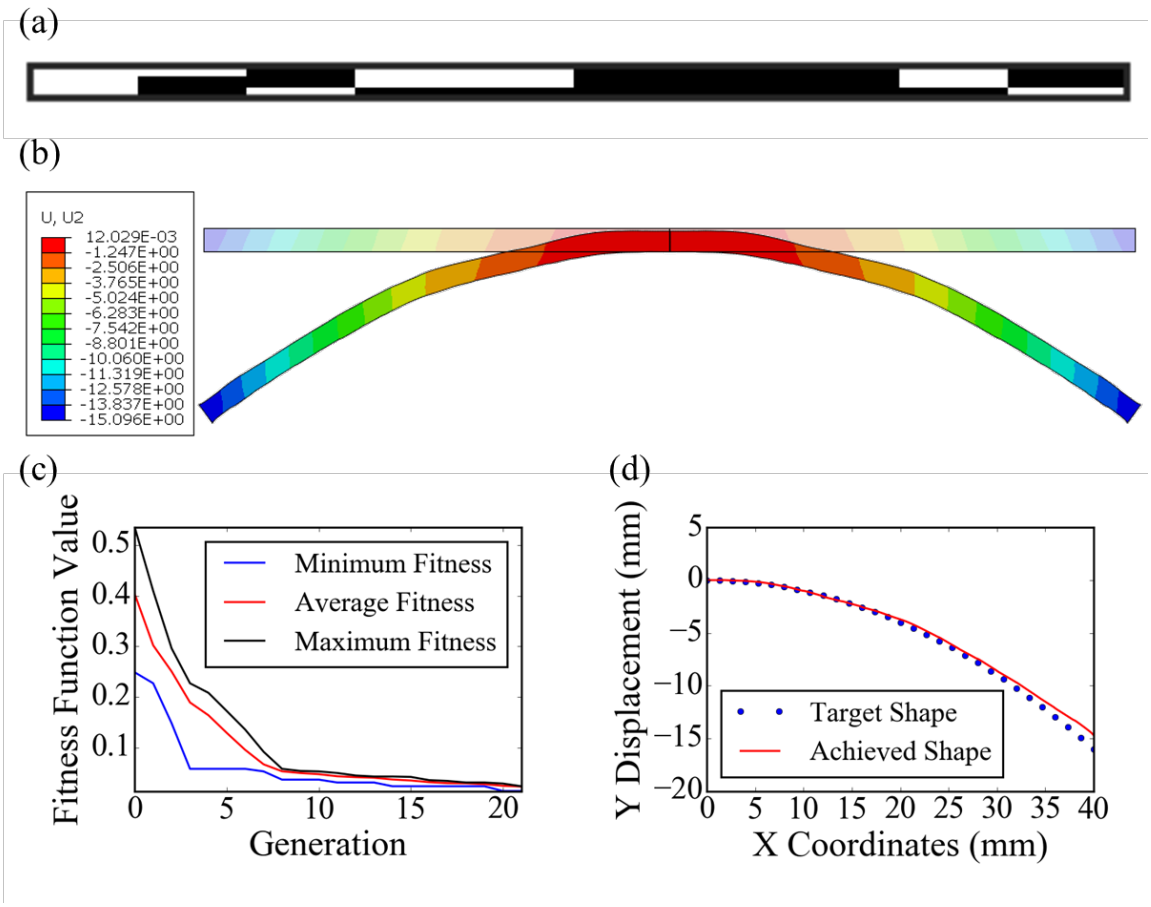

Figure 2.13 Results for the optimized material distribution for a parabolic shape. (a) The optimized material distribution for the parabolic shape where white is used to represent the active material and black is used to represent the passive material. (b) The ABAQUS simulation showing the deformed parabolic shape overlaid on top of the reference shape. (c) The evolution of the fitness function during the course of the optimization. (d) A comparison between the target shape and achieved shape.

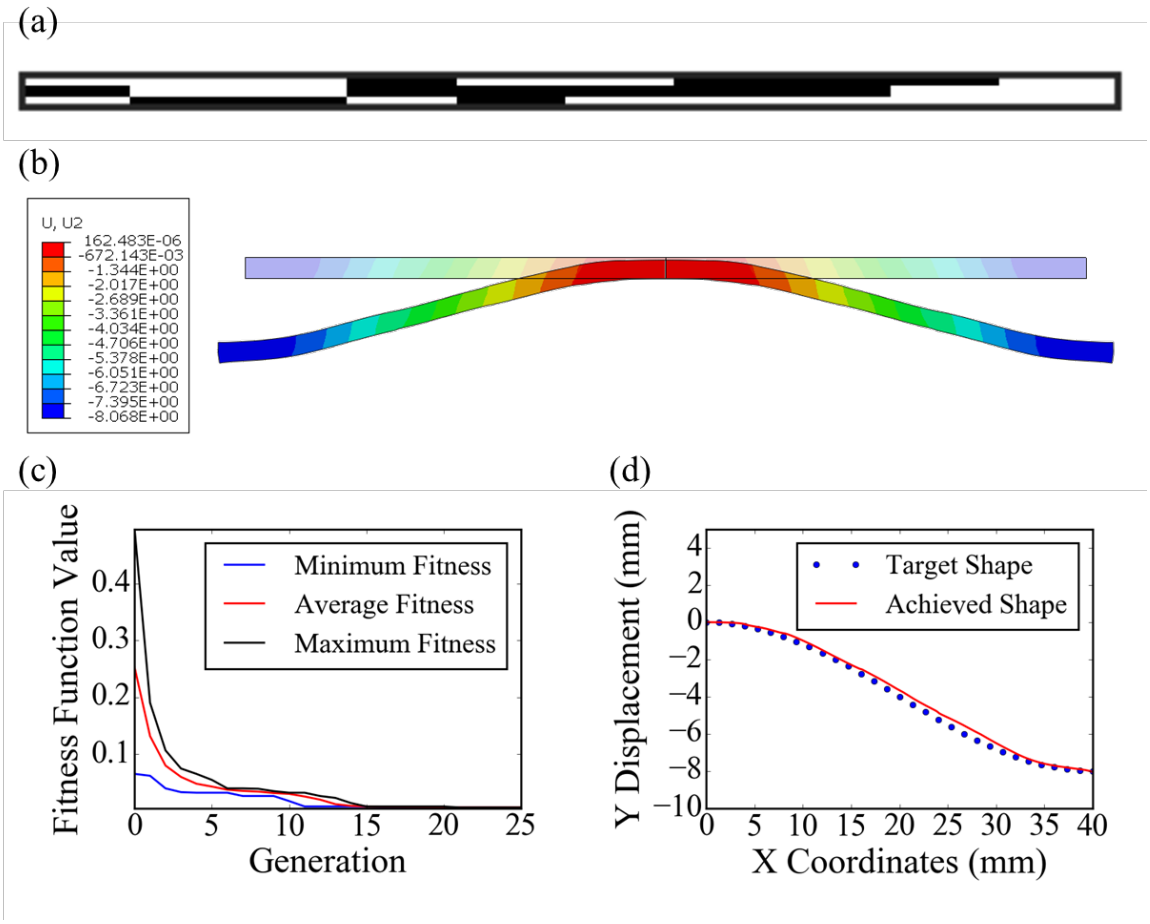

Figure 2.14 Results for the optimized material distribution for a sinusoidal shape. (a) The optimized material distribution for the parabolic shape where white is used to represent the active material and black is used to represent the passive material. (b) The ABAQUS simulation showing the deformed parabolic shape overlaid on top of the reference shape. (c) The evolution of the fitness function during the course of the optimization. (d) A comparison between the target shape and achieved shape.

2.2.6 Conclusion

In the above results we applied evolutionary algorithms to 4D printing design problems involving shape memory composites. The problems consisted of conventional strategies in 4D printing known as shape fixing. The problems illustrated demonstrate the capabilities of ML to generate material distributions for 4D printing design problems with reasonable discrepancy between the desired actuation and the actual actuation during

simulation and printing. A complex thermo-viscoelastic constitutive theory was utilized in the underlying finite strain simulations which would normally be a daunting task to implement into conventional topology optimization procedures.

Convergence onto a well performing design was usually achieved within about 20 generations of the algorithm with individual fitness evaluation being performed in parallel. Currently the evolutions are run on a single desktop computer with 8 cores available. This puts restriction on the number of fitness evaluations that may be carried out at a single time. If there are 32 individuals to be evaluated than the generation will be computed in 4 batches of 8 simulations each run concurrently. If the number of fitness evaluations is not evenly divided by the number of cores available, then certain cores can experience large amounts of ideal time further delaying the design generation and wasting computational resources. Material distribution generation can be sped up by using more sophisticated distributed computing strategies using multiple machines such that evaluation of an entire generation could be performed simultaneously.

The results in this work further show the capability of utilizing evolutionary algorithms in 4D printing design. Major advantages being an optimization method using gradient-free updates, geometries which capture the printing resolution of a machine, and the extension to using more than two materials for increased design freedoms. The methods presented in this work differ from other evolutionary algorithms, such as differential evolution, because since discrete integer values are used as variables to be optimized. Normally integer-based problems cannot be handled by an algorithm such as differential evolution because this algorithm is typically used for real value dominated optimization spaces. Although differential evolution can be modified to allow for integer-based design

spaces with the addition of constraints or ramping a real value to a nearest integer using post-processing functions such as a floor or ceiling type function. Although differential evolution cannot typically handle integer-based problems, the algorithms used in this work are much simpler than the underpinning of the differential evolution algorithm.

CHAPTER 3. A REACTION-DIFFUSION MODEL FOR DLP 3D PRINTING

3.1 Introduction

Photopolymerization is a widely utilized process which forms solid polymers through a light driven chemical reaction which combines many small monomers into a network. This process has been widely utilized in a diverse set of engineering fields such as 3D and 4D printing [94-97], dental fillings, and coatings. This method of polymerization is extremely efficient due to fast cure times but also have drawbacks such as large volume shrinkage induced by residual stress [27] in the network during curing and free radical diffusion. These phenomena can cause undesirable side effects such as warpage and regions of over cure which causes unwanted printing errors and geometrical defects from the CAD design.

A DLP 3D printer typically have a fixed number of operating components. These involve a motion stage to move the build plate up and down to add successive layers of material, a resin vat which holds the uncured liquid resin, and a light source which can either be a projector or a digital micromirror device (DMD). DMD devices have the greatest success in high resolution printing due to the small feature sizes attainable from the small micron-level sized mirrors which project the light in the desired pattern. This portion of the dissertation will mainly focus upon the DMD device and how this affects material process rather than other components of the DLP process such as the motion stage or resin vat design for example.

Recently grayscale DLP 3D printing [95, 97, 98] has shown great promise for expanding DLP 3D printing beyond a rapid prototyping technique. This method can control

the crosslinking density of the printed polymer locally by using grayscale light patterns rather than a single light intensity. This control of the crosslinking density can be exploited to locally tune the modulus and glass transition of the material which allows for the fabrication of composite structures in a one-shot method. Modulus tuning is also possible using other AM techniques, but they typically require multiple resins/materials and in the case of DLP 3D printing it requires multiple resin vats which necessitates a cleaning step in between material resin vat switching. The local tuning of the glass transition temperature offers a technique to fabricate SMP composites where the shape memory effect can be locally tuned based on the application end goal. In illustrative schematic of the DLP process using grayscale is shown in Figure 3.1.

Strategies for improving print resolution [25, 96, 99-102] have been discussed in the literature where there a few different approaches. One approach tunes the angle of the mirrors in the DMD device to create non-uniform Gaussian profiles [100] but this method requires a sophisticated computational algorithm which must be performed on each individual layer image. Other methods have utilized process planning of grayscale images to minimize

Previous modelling efforts in photopolymerization based additive manufacturing have focused on stereolithography [27, 103-109] where a laser scans the liquid resin to selectively cure regions of material. Modelling in this setting often requires a thorough understanding of the heat transfer process due to the large temperature gradients produced in this setting. Heat transfer can also play a role in DLP 3D printing by accelerating the reaction rate of the photopolymerization process but is not nearly as significant as in SLA.

Within this work the goal is to incorporate high fidelity photopolymerization reaction kinetics into a reaction-diffusion physics based model which accounts for the mass transport of free-radicals while at the same time supplying light patterns in a numerical setting which are consistent with those produced by a DMD devices in real DLP 3D printing.

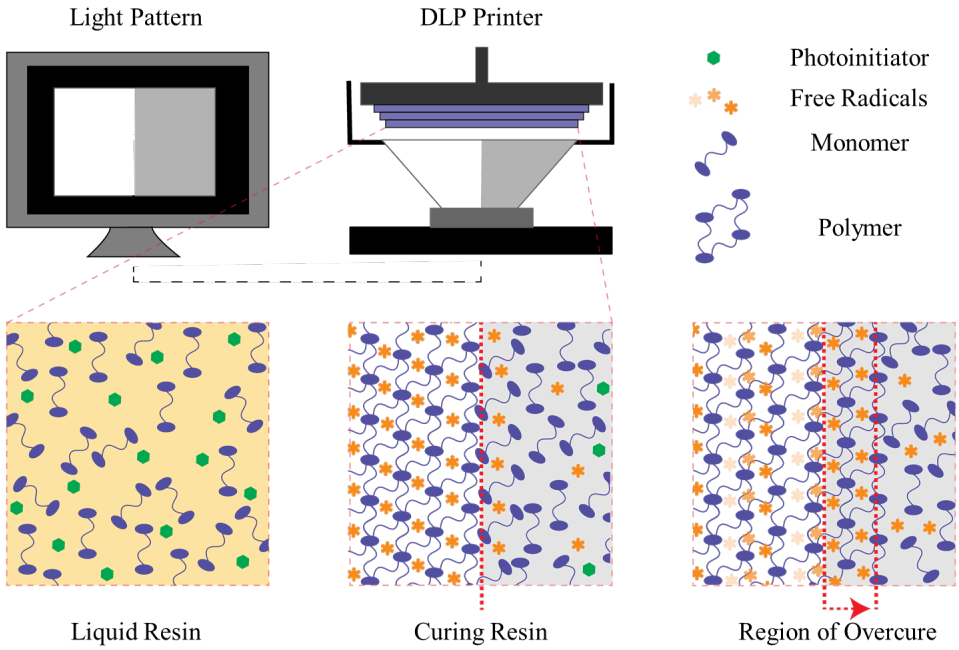

Figure 3.1 Illustrative schematic showing the DLP 3D printing process for a general photopolymer.

3.2 Experimental Methods

In this work we utilized polyethylene (glycol) diacrylate (PEGDA) for the monomer in the resin with a molecular weight of Mn = 250g/mol (Sigma-Aldrich, St. Louis, MO, USA). We used 0.1% by weight of Irgacure 819 as the photoinitiator. This loading percentage of the photoinitiator is lower than what is typically used in practical

DLP printing which we chose to have more control over the experiments to follow. To characterize the ink a reaction cell made up of two class slides with 50μm plastic shim spacers was constructed. The shims were used to control the height of the liquid resin. The resin mixture was then injected into the reaction cell and exposed under a DLP projector for various amounts of curing time. The resulting cured films were then removed the glass slide for characterization.

To characterize the chemical makeup of the resin during various states of cure we utilized Fourier transform interferometry (FTIR) (Nicolet iS50, Thermo Fischer Scientific, Waltham, MA, USA). Each sample was cured 32 times with a resolution of $1cm^{-1}$ to obtain an average result which was used in the data analysis. To determine the conversion of C=C double bonds into C-C single bonds we utilized the peak areas in between 1620 – $1635cm^{-1}$ with the C=O peak at $1725cm^{-1}$ as an internal standard. The peak ratio was calculated using the following relationship

$$PR = \frac{A_{1620-1635cm^{-1}}}{A_{1725cm^{-1}}}, \tag{3.1}$$

where $A_{1620-1635cm^{-1}}$ is the area under the peaks between 1620 and $1635cm^{-1}$ and $A_{1725cm^{-1}}$ is the area under the peak located at $1725cm^{-1}$. The degree of cure (DoC) was calculated using the following equation

$$p(t) = 1 - \frac{PR(t)}{PR(t=0)}, \tag{3.2}$$

where $PR(t)$ is the peak ratio calculated using equation (3.2) for spectrum at different cure times t. The FTIR spectra and accompanying calculated DoC are shown in Figure 3.2.

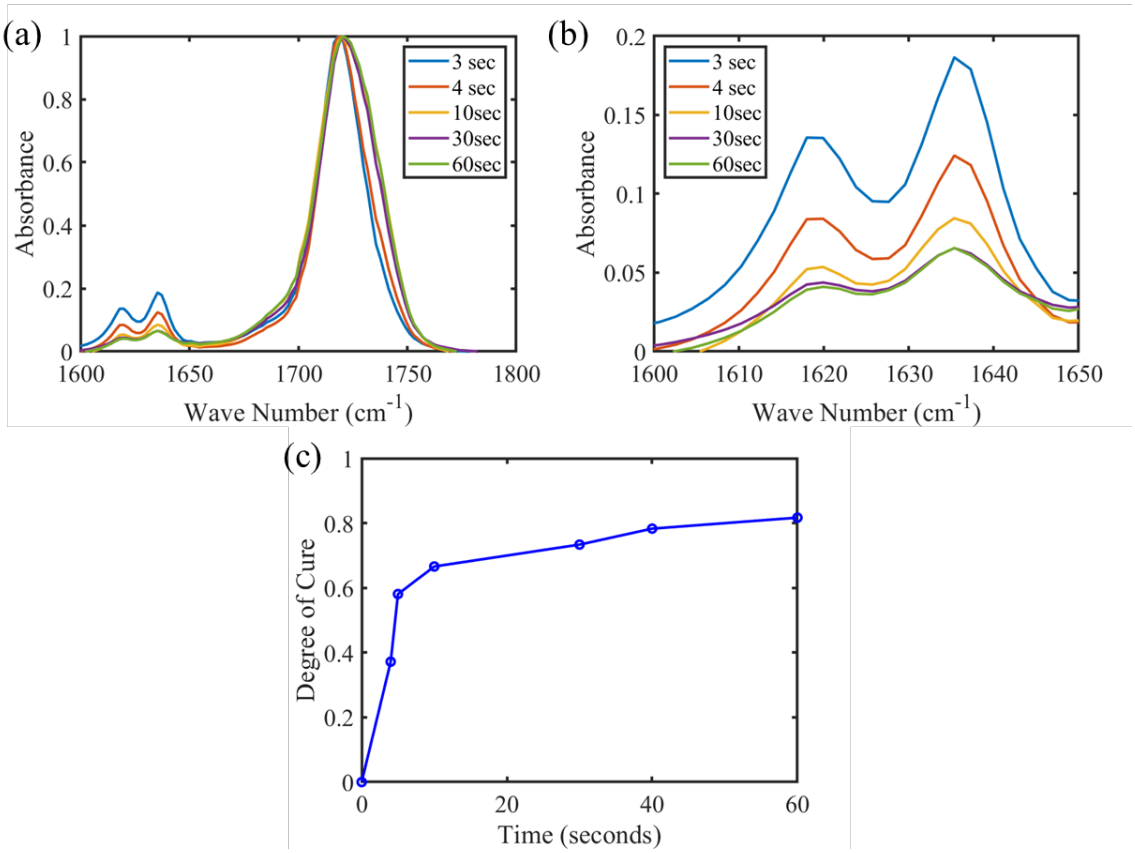

Figure 3.2 Experimental characterization of the resin used for calibrating the model. (a) FTIR spectra for the resin at various curing times showing the range of interest used for calculating the degree of cure. (b) Zoomed in FTIR spectra around the acrylate and ester peaks. (c) Degree of cure calculated from the experimental FTRI analysis.

To determine the geometric feature change during curing for grayscale printed parts we used a similar reaction cell as discussed above. Experiments were performed using this set up but instead of curing the entirety of the solution in between the two glass slides only small square regions of the liquid resin were selectively cured using the DMD device. The small squares that were cured consisted of both uniform light patterns and patterns that were split in a 50:50 ratio between a bright light and a dimmer light. Some examples of these experimental specimens are shown in Figure 3.3. The way in which it was ensured that regions were gelled was by letting liquid resin drain from the substrate

overnight and then taking an air hose to “wash” away liquid resin using compressed air. Gelled material would stick to glass slides quite well but the ungelled liquid resin would “wash” away. This was done to be sure that areas of the simple patterns that cure at different rates were actually cured and not just excess liquid resin that would have affected the optical images used for measurements.

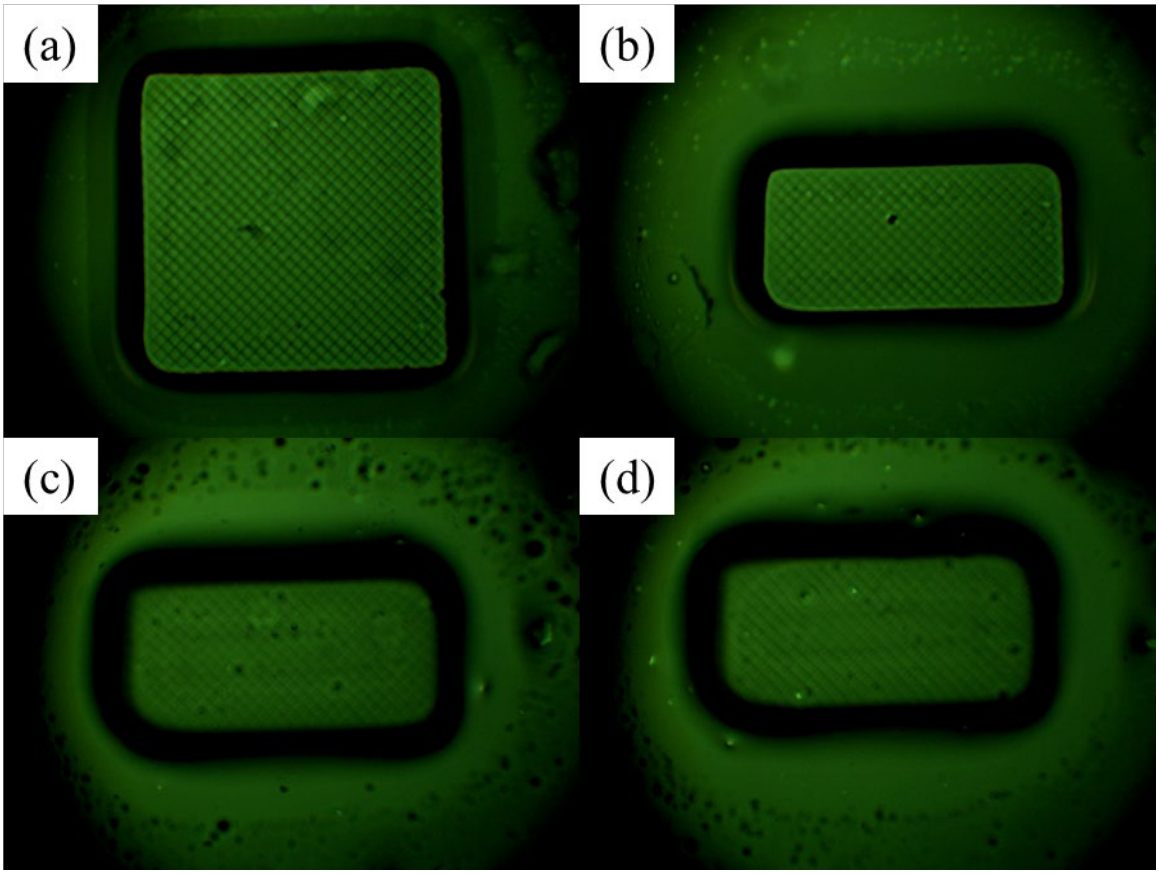

Figure 3.3 Experimental results for various grayscale patterns of 32 x 32 pixels cured for a period of 10 seconds. (a) All G0. (b) G0 cured next to G40. (c) G0 cured next to G60. (d) G0 cured next to G80.

3.3 Radiative Transfer

3.3.1 Theory

The key to properly modeling the printing process in DLP is accounting for the propagation of light through a curing polymer which will transition between a liquid state into a solidified state with varying degrees of crosslinking throughout the curing process. Modeling light propagation is typically conducted in one of two ways. The first is to solve the full set of the coupled Maxwell's equations which can be computationally expensive and is difficult to solve simultaneously with chemical rate equations due to the large mismatch in time scales between electromagnetism and engineering time scales typically seen in DLP printing such as seconds and minutes. The second approach is to use the equations of radiative transfer [110]. This simplifies matters greatly by reducing the number of necessary equations from 4 coupled vector PDEs to a single scale integro-differential equation which may expressed as

$$\frac{1}{c}\frac{\partial I_\nu}{\partial t} + \mathbf{d}\cdot\nabla I_\nu + \left(k_{\nu,s} + k_{\nu,a}\right) I_\nu = j_\nu + \frac{1}{4\pi} k_{\nu,s} \int_\Omega I_\nu d\Omega, \tag{3.3}$$

where c is the speed of light, I_ν is the intensity of the light at a frequency ν, $\mathbf{d}$ is a vector representing the direction of light propagation, $k_{s,\nu}$ is the scattering coefficient for the material at frequency ν, $k_{\nu,a}$ is the absorption coefficient for the material at frequency ν, and j_ν is the emission coefficient. Equation (3.3) simply states an energy balance for a travelling light beam. The beam of light loses energy due to absorption and gains energy by the emission process. Energy is redistributed by the scattering process expressed by the integral term on the right-hand side.

We now make some assumptions upon the way in which light propagates, absorbs, emits, and scatters through a curing resin during operation in a typical DLP process. The assumptions we make are as follows

1. Monochromatic light – a single frequency of light is typically projected from a DMD device so we can drop the frequency subscript ν, and only solve (3.3) for the frequency of light of interest.
2. Steady state light propagation, i.e. $\frac{\partial I}{\partial t} = 0$, - this term is typically only important if light was flashed on the order of pico-seconds due to the inverse speed of light scaling but this rate of flashing is never seen during practical DLP printing.
3. No emission, i.e. $j = 0$, - no light is produced during the photopolymerization so no light will be emitted by the liquid or curing/cured resin.
4. No scattering, i.e. $k_{\nu,s} = 0$, - Often scattering can play a significant role depending upon resin composition but the resin utilized in this study was purposely chosen to minimize the effects due to scattering. This will be discussed further below.
5. Unidirectional light propagation, i.e. $\mathbf{d} = \begin{bmatrix} 0 & 0 & 1 \end{bmatrix}^T$. Here we have defined the z-axis to be the direction of which the light propagates. This assumption is often true because the projection is typically pointed perpendicularly towards the liquid resin although some small deviations are also possible.

These assumptions can be justified with the following arguments. Monochromatic light is a valid assumption for DLP 3D printing since a projector is typically tuned to a single wavelength of light usually in the UV range or visible light range depending upon

the projector for the set up often picked based on the photoinitiator utilized in the resin to be printed. The steady state assumption is valid as long as the DLP projector does not flash images on the scale of nanoseconds or less. Due to the inverse scaling of the speed of light in the first term of equation (3.3) this term is negligible compared to the rest of the terms given the timescales typically seen in DLP 3D printing. Emission can be neglected since light is not produced during the reaction thus the photopolymer can not emit any light except for maybe at the free surface of the liquid resin but a vast percentage of the light will be absorbed by the liquid resin. Scattering emerges from a large difference in the refractive index locally in the material which can be a factor in some niche areas of DLP 3D printing such as bioprinting [26, 102]. Scattering is more important if modeling DLP printing of ceramic-polymeric materials [28, 111] of nano-composites with polydisperse distribution of particles. For the case of PEGDA scattering is not as significant due to the index of refraction not significantly changing during the photopolymerization process and due to the absence of scattering fillers such as ceramic nanoparticles. Scattering can and does cause undesirable side effects in the printing process, although not significant for the resin chosen above, but will not be considered in this work due to lack of experimental quantification and the large amount of numerical difficulty added in calculating the light propagation.

Since scattering, emission and time dependence will be neglected a reduced form of equation (3.3) may be written as follows

$$\mathbf{d}(\mathbf{x},t)\cdot\nabla I(\mathbf{x},t)+A(\mathbf{x},t)I(\mathbf{x},t)=0, \tag{3.4}$$

which only accounts for energy change due to absorption of light in the material. To simplify matters further, we may further restrict equation (3.4) by setting a proper

coordinate system in our modeling of the DLP process. Typically, the light is nearly perpendicular to the liquid resin so equation (3.4) can be simplified further to the following

$$\frac{\partial I(\mathbf{x},t)}{\partial z} + A(\mathbf{x},t)\, I(\mathbf{x},t) = 0 \quad \text{in} \quad \Omega, \tag{3.5}$$

with the boundary condition (for a single layer in the DLP process) of incident light intensity on the face with $z = 0$, i.e.

$$I(x, y, z = 0, t) = I_0. \tag{3.6}$$

The total absorption coefficient in equation (3.5) can be generalized to the following form

$$A(\mathbf{x},t) = \alpha_I C_I(\mathbf{x},t) + p(\mathbf{x},t)\, A_{polymer} + \left[1 - p(\mathbf{x},t)\right] A_{monomer} + w A_{absorber}, \tag{3.7}$$

where α_I is the molar absorptivity of the photoinitiator, C_I is the current concentration of photoinitiators, $A_{polymer}$ is the absorption from the converted polymer, $A_{monomer}$ is the absorption from the unreacted monomers, w is the weight percent of photoabsorbers, and $A_{absorber}$ is the absorption of photoabsorbers. The numerical values for the total absorption coefficient are presented in Table 3.1

3.3.2 Application to a Digital Micromirror Device

The light profile emanating from a DMD device may be calculated using a few simplifying assumptions. The first assumption is that the light profile from each pixel is a symmetric 2D Gaussian function. In general this may not be the case since the angle of individual mirrors in the DMD device may be tuned [100] to produce non-uniform 2D Gaussian forms. The second assumption is that the total light intensity projected by a DMD device is a summation over all projected pixels which may be expressed as

$$I_0(x,y)=\sum_i^m\sum_j^n I_{pixel}(g)\exp\left[-\left(\frac{x-x_0}{2\sigma}\right)^2-\left(\frac{y-y_0}{2\sigma}\right)^2\right], \tag{3.8}$$

where $I_{pixel}(g)$ is the light intensity of a single pixel which has functional dependence upon the grayscale value of that pixel denoted by g, σ is the beam radius, x_0 and y_0 denote the coordinates for the center of the Gaussian beam, and x and y correspond to arbitrary coordinates in plane. In order to calculate the grayscale dependent light intensity there are two more necessary relations. The first relation relates the grayscale value to the RGB value and the second relates the RGB value to the actual light intensity. The relation between the RGB value and grayscale is

$$RGB=255\left[a\sin(g)+b(g-b)^2-c\right], \tag{3.9}$$

where equation (3.9) is an empirically determined relationship where the number 255 in the equation is meant to scale the brightness to the maximum RGB value of 255, and a, b, and c are empirically determined fitting parameters. The actual physical light intensity can then be determined from the RGB value by using the following relationship

$$I_{pixel}=I_{max}\exp\left\{-\left[\frac{(RGB-f)}{h}\right]^2\right\} \tag{3.10}$$

where I_{max} is the maximum intensity obtained when RGB is 255 and f and h are empirically determined fitting parameters. The empirically determined relationship for the grayscale dependence upon the RGB value is shown in Figure 3.4a. This relationship appears nearly linear in regions of low grayscale but starts to deviate from the linearity around 50% grayscale. By substituting equation (3.9) into equation (3.10) the grayscale dependence of the light intensity can be determined which is shown in Figure 3.4b. It can

be seen the actual light intensity for grayscale values is non-intuitive with an almost linear region between grayscale values of 20% and 60% but a less clear relationship outside of those regions.

Table 3.1 Parameters corresponding to the radiative transfer portion of the model.

Radiative Transfer Parameters			
Parameter	Description	Value	Units
α_I	Photoinitiator Molar Absorptivity	45.83	m^2 / mol
$A_{monomer}$	Monomer Absorption	0	$1/m$
$A_{polymer}$	Polymer Absorption	1806.9	$1/m$
$A_{absorber}$	Photoabsorber Absorption	23618066.7	$1/m$
I_0^{ideal}	Light intensity of projector	64	W/m^2
I_0^{pixel}	Light Intensity of a Pixel	41.08	W/m^2
σ	Beam Diameter	1.77E-05	m

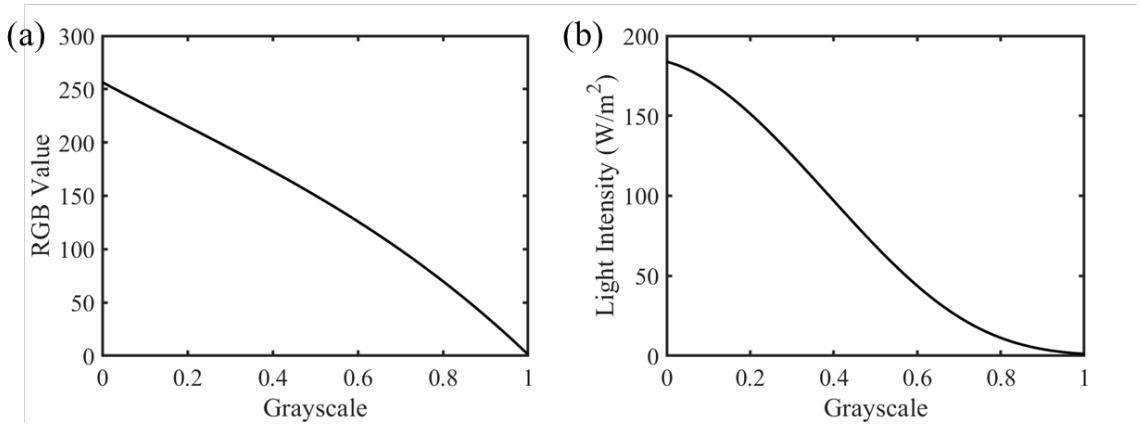

Figure 3.4 Calibrations for the actual light intensity used in a DLP projector based on the RGB value and grayscale. (a) The dependence of grayscale value upon the RGB value. (b) The light intensity in W/m^2 as a function of grayscale.

However, the complexities of the projected light patterns do not stop there. Since each individual "pixel" projected from a DMD device is a Gaussian beam there is crossover between the individual beams which causes the light intensity at a single point to be due to several beams adding up. An illustrative example of this for 1D Gaussian beams is shown in Figure 3.5. In Figure 3.5a a single Gaussian beam is shown based on the empirically determined intensity of a single pixel and the beam diameter. The dotted red lines correspond to where an individual "pixel" should cutoff when the full DMD device is projected. It can be clearly seen that the light bleeds out of that region, although at a lower intensity. This lower intensity can cause regions of the liquid resin, outside of the desired projection area, to cure at slower rates then regions of the liquid resin inside the projection area. This effect can lead to non-uniform cure localized to the edge of printed parts if a single light intensity is utilized. Figure 3.5b shows the light intensity for a simplified 1D case where 10 beams are added to give the total light intensity shown in blue. Figure 3.5c-d show the same approach but where 5 of the beams are G0 and the others are G40 (c) and G80 (d). It can clearly be seen that the transition between the two light intensities is not a jump but there exists a region where the light intensity continuously changes between the two. The numerical values for the beam radius and light intensity of both a single pixel and the full projection of all pixels of the DMD device are presented in Table 3.1.

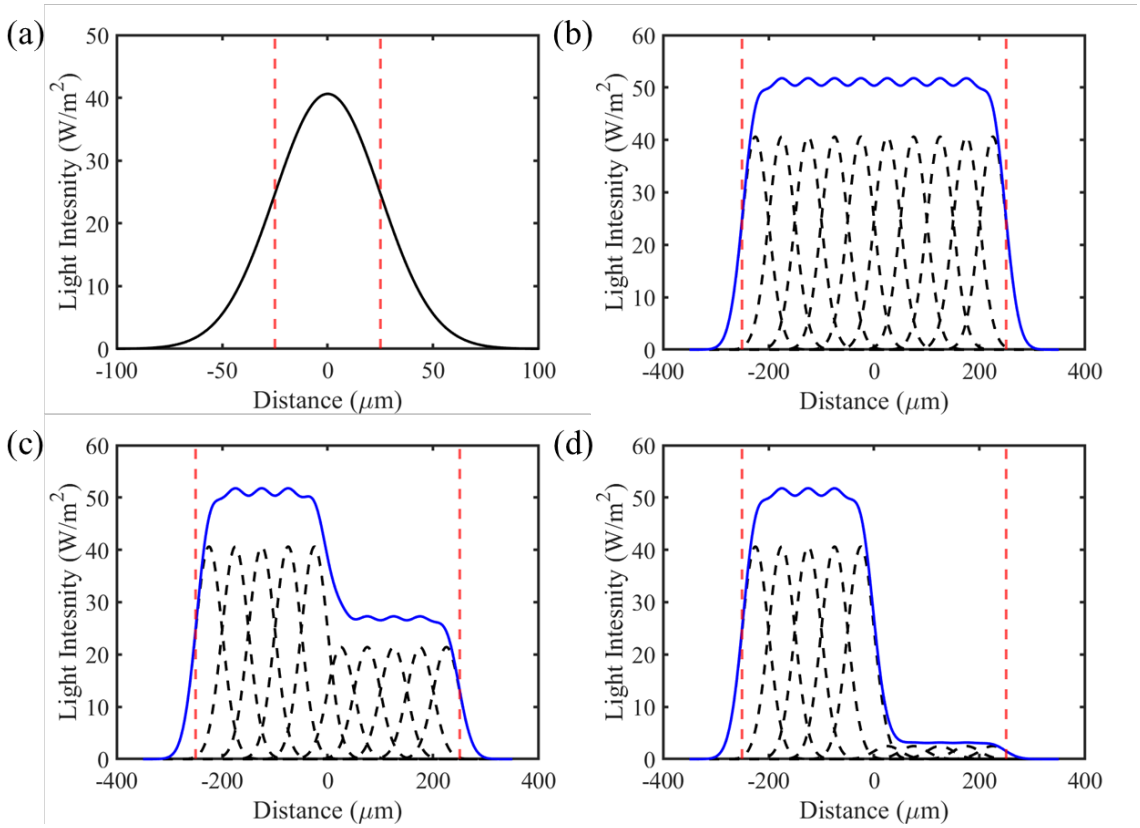

Figure 3.5 One dimensional illustrative of example of how individual Gaussian beams add up. (a) A single Gaussian beam illustrated in black where the reds lines mark where a "pixel" should cut off. (b) Ten Gaussian beams illustrated in black and their sum shown in blue where again the red lines mark where the boundary of "10 pixels" should cut off. (c) Ten Gaussian beams where the left five beams have a grayscale value of G0, and the right five beams have a grayscale value of G40. The individual beams are illustrated with dotted black lines, their sum is shown in blue, and the red lines mark where the boundary of "10 pixels" should cut off. (d) Ten Gaussian beams where the left five beams have a grayscale value of G0, and the right five beams have a grayscale value of G80. The individual beams are illustrated with dotted black lines, their sum is shown in blue, and the red lines mark where the boundary of "10 pixels" should cut off.

The previous figures were just for illustrative purposes and do not capture the true reality of the complexity of DMD device light patterns. In Figure 3.6 2D light patterns, which were used for the modeling results later, are shown. Figure 3.6a-b show a pure G0 light pattern for a 2x2 pixel and 32x32 pixel array to compare the differences between fine-scale light patterns and large-scale light patterns. In Figure 3.6b the "diamond pattern"

should be noted as this is seen when a DMD projector is projected on the reservoir of liquid resin and an artifact of this pattern shows up in the cured samples shown in Figure 3.3. Grayscale patterns where the pattern is split in half between G0 and G40 are shown in Figure 3.6c-d for a 2x2 and 32x32 pixel array respectively. The key feature to note from these two figures is the apparent non-symmetric nature of the light pattern from visual inspection. This phenomenon, along with the diffusion of chemical species to be discussed later, contributes to the differences in geometric features of regions cured with different grayscale values.

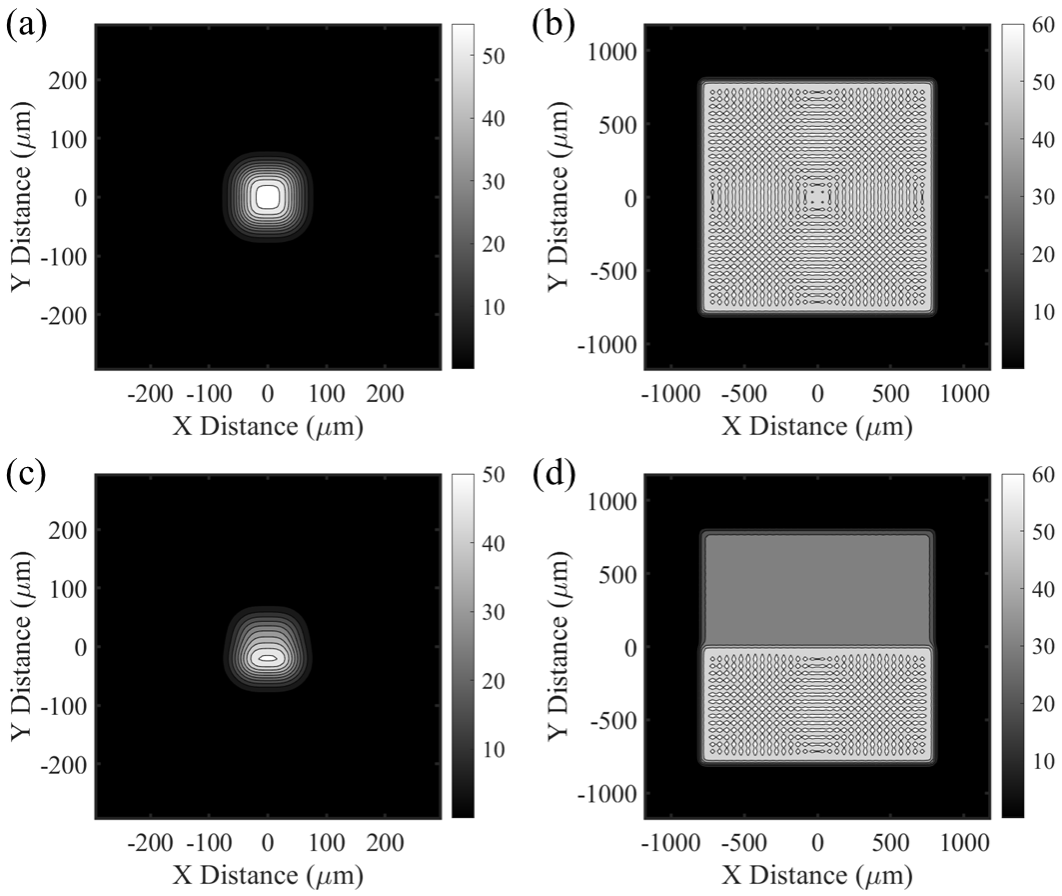

Figure 3.6 Examples of different 2D pixel patterns. (a) A 2x2 pixel pattern where all four pixels have a grayscale value of G0. (b) A 32x32 pixel pattern where all of the pixels have a grayscale value of G0. (c) A 2x2 pixel pattern where the bottom two

pixels have a grayscale value of G0, and the top two pixels have a grayscale value of G40. (d) A 32x32 pixel where the bottom half of the pixels have a grayscale value of G0, and the top half of the pixels have a grayscale value of G40.

3.4 Reaction Kinetics

3.4.1 Reaction Mechanism

Based on the propagation of light equation defined in equation (3.4) the kinetic rate equations for the different constituents in the photocuring resin will now be presented. Photopolymerization typically is decomposed into several coupled chemical reactions. These are photodecomposition, initiation, propagation, oxygen inhibition, and termination [104, 112, 113]. The photoinitiators begin the reaction once they come in contact with a high enough dose of light to decompose into one or more free-radicals (in our case two free radicals) which is represented by the following reaction scheme

$$In \xrightarrow{nh\nu} 2R^{*}. \tag{3.11}$$

In equation (3.11) In is used to represent photoinitiators and R^{*} is used to represent free radicals where the * symbol is utilized to denote that this species has an active site for polymerization to proceed. Functional groups in the monomers (in this case PEGDA acrylate groups) are then activated by the free radicals to initiate the polymerization process which has the following scheme

$$R^{*} + M \rightarrow RM^{*}\left(P^{*}\right), \tag{3.12}$$

where RM^{*} denotes an active monomer which can then propagate the reaction to other unreacted monomers and P^{*} denotes an active site on a polymer chain of arbitrary length. Upon the initiation of the reaction represented in equation (3.12), the polymer chains can

then propagate the reaction by crosslinking with other polymer chains which we may be denoted in the form of a reaction scheme as follows

$$R - M_n^* + M \rightarrow RM_{n+1}^* \quad \text{or} \quad P^* + M \rightarrow P^*. \tag{3.13}$$

Termination can proceed in two different mechanisms which are represented in the scheme below

$$RM_m^* + RM_n^* \rightarrow RM_{m+n}R / RM_m + RM_n \quad \text{or} \quad P^* + P^* \rightarrow P_{dead}, \tag{3.14}$$

where the first mechanism is known as combination where two radicals can combine to form a single dead polymer chain denoted by $RM_{m+n}R$ and the second mechanism is known as disproportionation where two dead polymer chains are produced denoted by $RM_m + RM_n$. Oxygen inhibition [113, 114] is also significant in the photopolymerization kinetics, especially in practical DLP 3D printing where an oxygen permeable window is typically utilized to allow for layer separation from the build area so a layer by layer process can proceed without damaging the initial layer which would cause drastic buildup of geometric defects as printing proceeds. The reaction scheme for oxygen inhibition may be written as

$$\mathrm{RM}_m^* + O_2 \rightarrow RM_mOO, \tag{3.15}$$

which essentially says that oxygen can attack radicals and cause them to no longer have an active site for the polymerization process to proceed.

3.4.2 Reaction Kinetics

Within the competing reactions discussed in the previous section, only the four main species (functional groups) participating within the photochemical reactions will be

tracked. These species are photo-initiators, free-radicals, oxygen, and monomers. We will denote the concentration of photo-initiators by C_I, the concentration of free radicals by C_R, the concentration of oxygen by C_O, and finally the concentration of monomers will be denoted by C_M. With the concentration of monomers known at each instant we can then ascertain the current state of network connectivity through the DoC. The model form of the DoC is analogous to the experimentally determined form given in equation (3.2) which is defined to be

$$p(\mathbf{x},t) = 1 - \frac{C_M(\mathbf{x},t)}{C_M(\mathbf{x},t=0)}, \tag{3.16}$$

which can be simply thought of as the reduction of monomers during the photopolymerization process.

The rate of production/consumption of each of the four species we wish to track will now be introduced and discussed. Once light is irradiated upon the uncured resin, light splits photoinitiators and begins the photopolymerization reaction. The rate of photoinitiator concentration is typically modeled using a first order reaction mechanism as follows [18, 27, 114, 115]

$$R_I(\mathbf{x},t) = -\beta I(\mathbf{x},t) C_I(\mathbf{x},t), \tag{3.17}$$

where β is the photodecomposition rate. The rate of evolution of the concentration of free radicals is the most complex part of the reaction kinetics with three contributing factors. The number of radicals is increased when more photoinitiators are present and radical concentration is reduced through termination and oxygen inhibition which may be represented mathematically as

$$R_R(\mathbf{x},t) = m\beta I(\mathbf{x},t) C_I(\mathbf{x},t) - 2k_{term}(\mathbf{x},t)\left[C_R(\mathbf{x},t)\right]^2 - k_O C_O(\mathbf{x},t) C_R(\mathbf{x},t), \quad (3.18)$$

where m denotes the number of radicals produced by the photoinitiators which is 2 for the case of a PEGDA material system, k_{term} is a non-constant termination reaction coefficient which will be discussed below, and k_O is the reaction coefficient for the effects of oxygen inhibition. The power of 2 in the second term on the right hand side of equation (3.18) is present to model the effect of two radicals terminating. In general, the termination of radicals can be a very complex process where lone radicals as well as more than two radicals may terminate. Within this work only termination due to two radicals was considered for simplicity. The inhibitive effects of oxygen on the photopolymerization process may be modeled using the second order rate equation below

$$R_O(\mathbf{x},t) = -k_O C_R(\mathbf{x},t) C_O(\mathbf{x},t). \quad (3.19)$$

Finally, the rate of monomer consumption can be modeled using the following second order rate equation

$$R_M(\mathbf{x},t) = -k_p(\mathbf{x},t) C_R(\mathbf{x},t) C_M(\mathbf{x},t), \quad (3.20)$$

where k_p represents the non-constant polymerization reaction rate coefficient to be discussed below. Within this work volume shrinkage was not considered so the current and reference configuration may be considered to be the same.

In general, the propagation rate and termination rate in equations (3.20) and (3.18) are not constant. The increasing viscosity of the curing resin causes auto acceleration of the chemical reaction with a sharp change in reaction rate past a certain DoC [116, 117]. Termination rate of radicals is greatly affected by the local diffusion of free radicals from

one chain to a neighboring chain. Two major mechanisms contribute to this phenomenon which are termination due to translational diffusion of radicals and termination due to reaction-diffusion of radicals. The two mechanisms do not occur independent of each other so the total termination rate may be written as [116]

$$k_{term}\left(\mathbf{x},t\right)=k_{t,D}\left(\mathbf{x},t\right)+k_{t,RD}\left(\mathbf{x},t\right), \tag{3.21}$$

where $k_{t,D}\left(\mathbf{x},t\right)$ denotes the translational diffusion contribution to radical termination and $k_{t,RD}\left(\mathbf{x},t\right)$ accounts for the reaction-diffusion termination mechanism. Translational diffusion of chains is due to both the center-of-mass translational diffusion and segmental diffusion. This has been discussed in the literature previously and we use the form utilized in [118]

$$\frac{1}{k_{t,D}}=\frac{1}{k_{t,SD}}+\frac{1}{k_{t,TD}}, \tag{3.22}$$

where $k_{t,SD}$ denotes the segmental diffusion which does not depend upon the degree of cure and $k_{t,TD}$ corresponds to the translational diffusion of the radical's center of mass. The translational diffusion in general depends upon the viscosity of the solution. During the photopolymerization process viscosity increase with increasing degree of cure which directly leads to a decrease of translational diffusion. This can be written simply as

$$\frac{1}{k_{t,TD}}=\frac{\exp\left(cp\right)}{k_{t,TD0}}. \tag{3.23}$$

Another critical termination mechanism is the movement of radicals along a chain as the chain grows which may be modeled using the following relationship

$$k_{t,RD} = C_{RD} k_p \left(1 - p\right), \tag{3.24}$$

where C_{RD} is the reaction diffusion proportion parameter and k_p is the polymerization rate. The polymerization rate is highly non-linear in terms of the current degree of cure of the network and decreases with high conversion. This term has been previously modeled as [27, 116, 119, 120]

$$k_p\left(\mathbf{x},t\right) = \frac{k_{p0}}{1 + \frac{k_{p0}}{k_{p,D0}} \exp\left(cp\right)}, \tag{3.25}$$

where k_{p0} is the initial polymerization rate prior to the beginning of the reaction and $k_{p,D0}$ is parameter which characterizes the propagation portion of the photopolymerization reaction. The nonlinear polymerization and termination rate are shown in Figure 3.7 as a function of the DoC. This rate is relatively constant during early stages of the reaction but drops off sharply as network connectivity begins to increase.

The total termination rate may be calculated with the aid of equations (3.21), (3.22), (3.23), (3.24), and (3.25) as

$$k_{term}\left(\mathbf{x},t\right) = \frac{1}{\frac{1}{k_{t,SD}} + \frac{\exp\left(cp\right)}{k_{t,TD0}}} + \frac{C_{RD}\left(1-p\right)k_{p0}}{1 + \frac{k_{p0}}{k_{p,D0}} \exp\left(cp\right)}. \tag{3.26}$$

Similar to the polymerization rate, the termination rate is also highly non-linear as shown in Figure 3.7. The numerical values for the large number of parameters listed above for calibrated using non-linear least squares with reference values from [27]. The only parameter that significantly changed was the photodecomposition rate β due to a different photoinitiator being utilized in this study but with the same monomer used. The fitting to

the experimental data is shown in Figure 3.8 where reasonable agreement between the experiment and the model calibration is achieved.

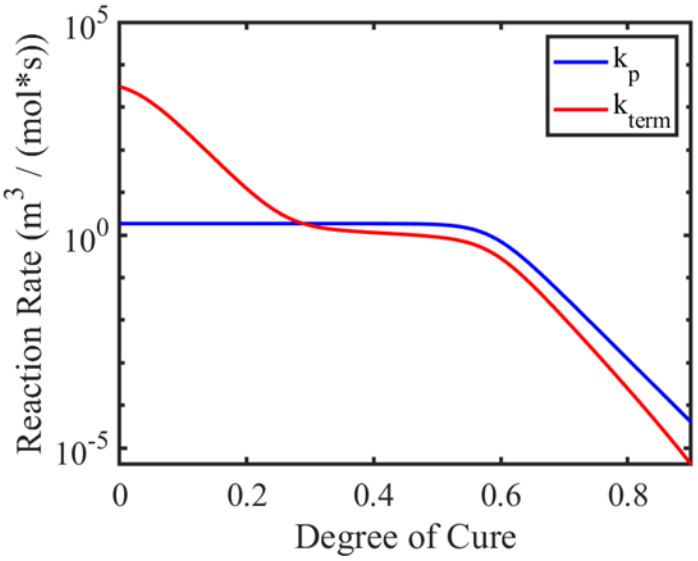

Figure 3.7 The dependence of the termination rate and polymerization rate on degree of cure.

Table 3.2 Reaction kinetics parameters used in the simulations.

Photopolymerization Parameters			
Parameter	Description	Value	Units
β	Photodecomposition Rate	2.70E-03	s^2 / kg
k_{p0}	Initial Polymerization Rate	1.86048	$m^3 / mol / s$
$k_{p,D0}$	Diffusion Controlled Propagation Rate	8.99E+08	$m^3 / mol / s$
k_{SD}	Segmental Diffusion	4.39E+03	$m^3 / mol / s$
c	Relative Viscosity Coefficient	34.149	Unitless
$k_{t,TD0}$	Translational Diffusion	10024.43	$m^3 / mol / s$
C_{RD}	Reaction-Diffusion Proportion Parameter	1.01E+00	Unitless
k_O	Oxygen Inhibition Rate	3.50E+03	$m^3 / mol / s$

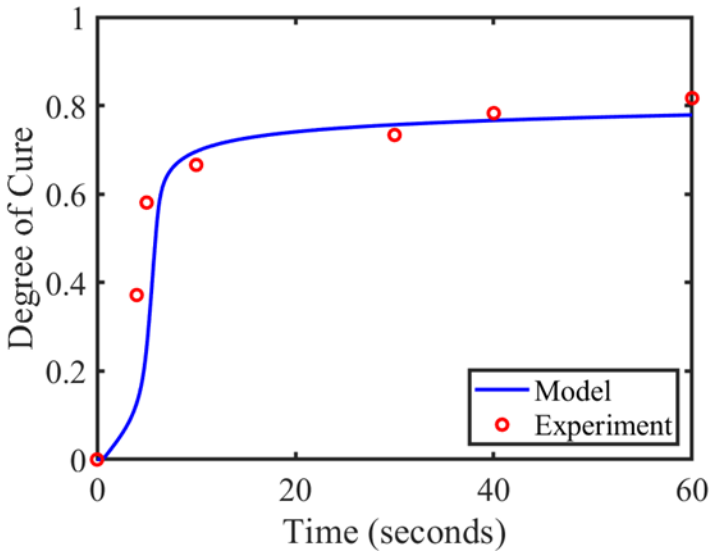

Figure 3.8 Kinetics model fitting against the experimentally determined DoC.

To illustrate why a low photoinitiator resin was chosen for the experiments Figure 3.9 shows DoC evolution curves for different grayscale values. The DoC evolution curves for the photoinitiator concentration used in the experimental studies (0.1wt%) are shown in Figure 3.9a and DoC evolution curves for a typical resin formulation (0.7wt% photoinitiator) are shown in Figure 3.9b. Based on the curves shown in these figures it can be seen that differences between G0 and G80, for example, would be difficult to determine unless very precise control was utilized and radical scavengers were properly utilized to kill the reaction since even after light has stopped shining the polymerization process can still proceed until all of the radicals have terminated.

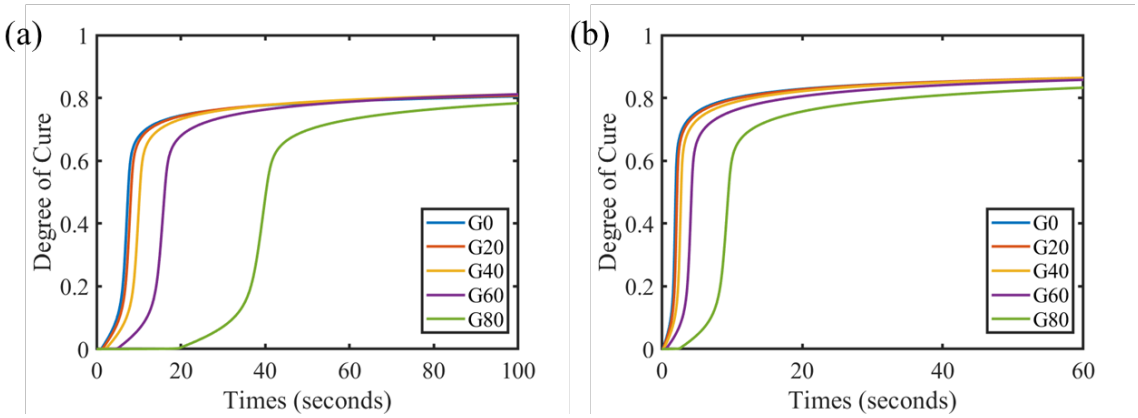

Figure 3.9 Evolution of degree of cure for different grayscale values. (a) DOC evolution with a photoinitiator concentration of 0.1wt% which was utilized in the experiments. (b) DOC evolution with a photoinitiator concentration of 0.7wt% which is a typical value for practical printing.

3.5 Diffusion in Curing Polymer Networks

3.5.1 Balance Laws

Within this section the necessary species transport balance laws to model diffusion of chemical species is introduced. The species transport equation [121, 122] are typically written in the following form

$$\frac{\partial C_\alpha(\mathbf{x},t)}{\partial t} = -\nabla\cdot\mathbf{j}_\alpha(\mathbf{x},t) + R_\alpha(\mathbf{x},t), \tag{3.27}$$

where $\frac{\partial C_\alpha}{\partial t}$ represents the rate of change of the concentration for an arbitrary chemical species denoted by α, $\mathbf{j}_\alpha$ represents the flux of that species, and R_α denotes the rate of production/consumption of that arbitrary species which in general may depend upon all other species present. The R_α's were introduced in the previous section. It remains to

prescribe a constitutive form for the flux vector $\mathbf{j}_\alpha$. The prescription of this quantity utilizes Fick's law of diffusion [121, 122] which may be written as

$$\mathbf{j}_\alpha\left(\mathbf{x},t\right) = -D_\alpha \nabla C_\alpha\left(\mathbf{x},t\right), \tag{3.28}$$

where D_α is the diffusion for an arbitrary species α. Substitution of equation (3.28) into equation (3.27) gives the following

$$\frac{\partial C_\alpha}{\partial t} = \nabla \cdot \left(D_\alpha \nabla C_\alpha\right) + R_\alpha, \tag{3.29}$$

which is the commonly represented reaction-diffusion equation.

With use of equations (3.29), (3.17)-(3.20) the full set of governing equations for the model may now be listed. The photoinitiator concentration balance equation may be written as

$$\frac{\partial C_I}{\partial t} = \nabla \cdot \left(D_I \nabla C_I\right) - \beta I C_I, \tag{3.30}$$

the free-radical concentration balance equation may be written as

$$\frac{\partial C_R}{\partial t} = \nabla \cdot \left(D_R \nabla C_R\right) + m\beta I C_I - 2k_{term} C_R^2 - k_O C_O C_R, \tag{3.31}$$

the oxygen concentration balance equation may be written as

$$\frac{\partial C_O}{\partial t} = \nabla \cdot \left(D_O \nabla C_O\right) - k_O C_R C_O, \tag{3.32}$$

and finally, the monomer concentration balance equation may be written as

$$\frac{\partial C_M}{\partial t} = \nabla \cdot \left(D_M \nabla C_M\right) - k_p C_R C_M. \tag{3.33}$$

For equations (3.30)-(3.33) the boundary conditions will be a Neumann boundary condition on the entire boundary to model that chemical species cannot leave the reaction cell. In some instances of DLP 3D printing this may not actually be the case such as when an oxygen reservoir is present but for the case of curing between glass slides this is a reasonable assumption. The Neumann boundary condition for an arbitrary species α may be written as follows

$$\mathbf{n} \cdot \nabla C_{\alpha} = 0 \quad \text{on} \quad \partial\Omega, \tag{3.34}$$

where $\mathbf{n}$ is the unit normal to the surface and $\partial\Omega$ is the boundary of the domain.

3.5.2 Specialization of the Form of the Diffusion Coefficient to Depend Upon DoC

The diffusion coefficient will now be specialized based on a form previously used in SLA modeling [103]. The idea behind this form is that there are two easily distinguishable diffusivity regimes. The first is the uncured liquid resin where different species can easily diffuse around the medium due to low viscosity. The second is a fully crosslinked polymer network where diffusion is much more difficult. This may be written as follows

$$\frac{1}{D_{\alpha}(p)} = \frac{p}{D_{\alpha}^{solid}} + \frac{1-p}{D_{\alpha}^{liquid}}, \tag{3.35}$$

where the diffusivity for an arbitrary species α is taken to be a function of the crosslinking density. In equation (3.35) D_{α}^{solid} represents the diffusivity of a pure solid polymer and D_{α}^{liquid} is the diffusivity of the pure liquid resin prior to exposure to light and photopolymerization process proceeding. Some of the parameters list above were taken from literature [103, 114] for the monomers, oxygen, and photoinitiators. However, no

literature values for free radical diffusivity were found so these were parameters that were tuned. The parameters utilized for the simulations that are presented in the following sections are listed in

Table 3.3 Diffusion parameters used in the simulations.

Diffusion Parameters			
Parameter	Description	Value	Units
D_I^{liquid}	Photoinitiator Diffusivity in Liquid	1.00E-10	m^2 / s
D_I^{solid}	Photoinitiator Diffusivity in Solid	1.00E-14	m^2 / s
D_R^{liquid}	Free Radical Diffusivity in Liquid	1.00E-10	m^2 / s
D_R^{solid}	Free Radical Diffusivity in Solid	1.00E-10	m^2 / s
D_O^{liquid}	Oxygen Diffusivity in Liquid	1.00E-10	m^2 / s
D_O^{solid}	Oxygen Diffusivity in Solid	1.00E-10	m^2 / s
D_M^{liquid}	Monomer Diffusivity in Liquid	1.00E-10	m^2 / s
D_M^{solid}	Monomer Diffusivity in Solid	1.00E-14	m^2 / s

3.6 Effect of Diffusion on Geometrical Results of DLP Printing

To ascertain the effects that light patterns and species diffusion has upon the geometric features of printed structures the experiments discussed earlier are analyzed with simple measurements. A schematic of the measurements that are presented is shown in Figure 3.10. The grayscale patterns considered are split down the middle where the bottom half is the brightest light (G0) and the top half is taken to be any grayscale value including G0.

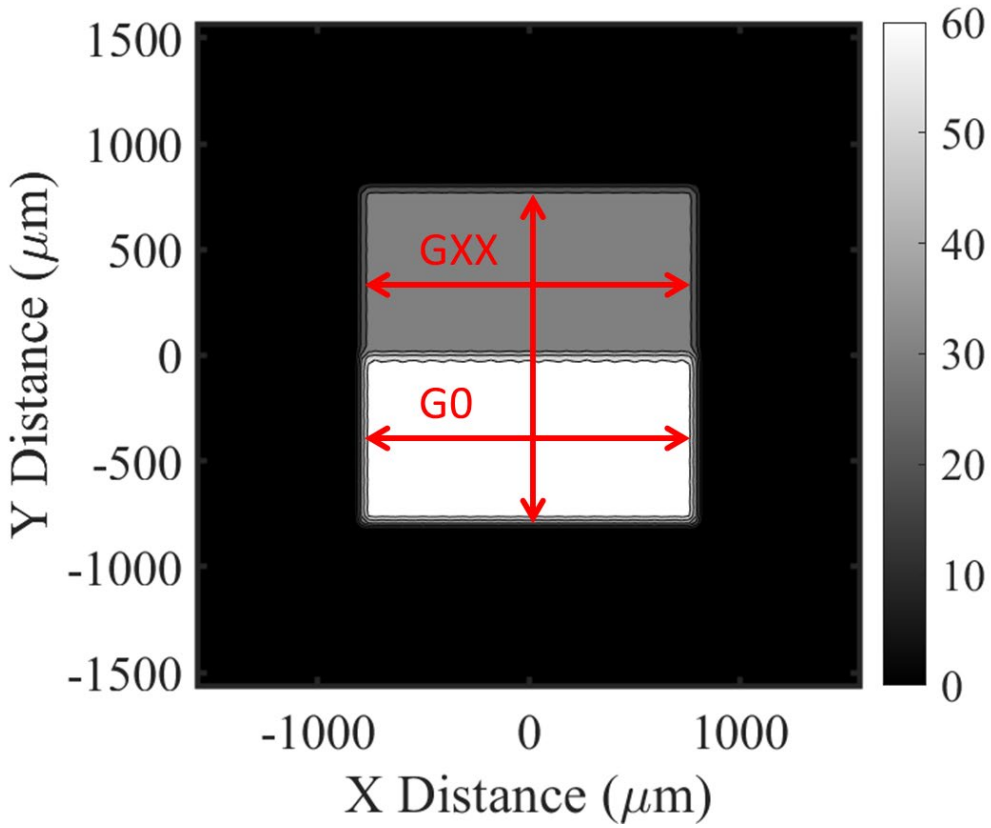

Figure 3.10 Schematic showing the geometrical simulation results which were compared against experimental measurements. GXX is used to represent an arbitrary grayscale between G0 and G80. The red lines denote the places where measurements were taken.

The three measurements are as follows. The first two are horizontal measurements across the middle of the individual "discrete" regions of differing grayscale value. The third measurement is the vertical height along the y-axis. The measurements were performed using optical microscopy. The idea behind these measurements is that the bright G0 region will cure faster (in the case of G80, 30 seconds faster) than the dim region. This will create a lag in the free-radicals produced and will produce different concentration gradients of free radicals in the two regions. The vertical measurement is meant to determine the movement of the "interface" between the two regions which has been

experimentally reported [123]. The results comparing the model predictions and the experiments for the two horizontal measurements are shown in Figure 3.11. Reasonable agreement is seen between the comparison although there are only a handful of experimental data points.

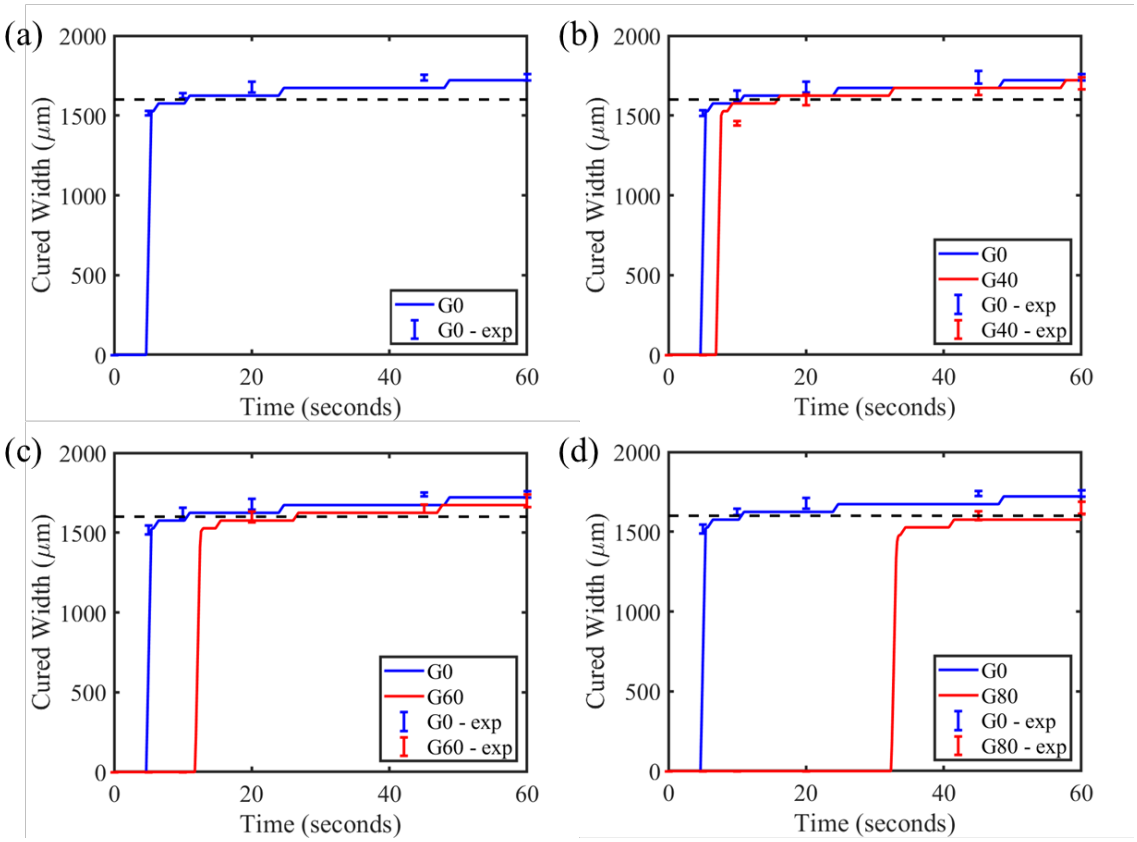

Figure 3.11 Simulation compared to experimentally measured widths for various grayscale patterns. (a) All G0 grayscale pattern. (b) G0 – G40 grayscale pattern. (c) G0 – G60 grayscale pattern. (d) G0 – G80 grayscale pattern.

The results comparing the model predictions and the experiments for the vertical measurement is shown in Figure 3.12. Reasonable agreement is also seen between the comparison although there are only a handful of experimental data points. The vertical measurements are the most interesting for determining the resolution of material properties for example. It can be seen from these results that the G0 region cures first, as expected,

followed by a region of the graph with a slope which corresponds to over cure due to free-radical diffusion. After some time, the darker region eventually cures which is represented by the step in the figures. This phenomenon is more pronounced for larger differences in light intensity which can pose a problem for fabricating novel composites with large material property variation as reported in [97, 123].

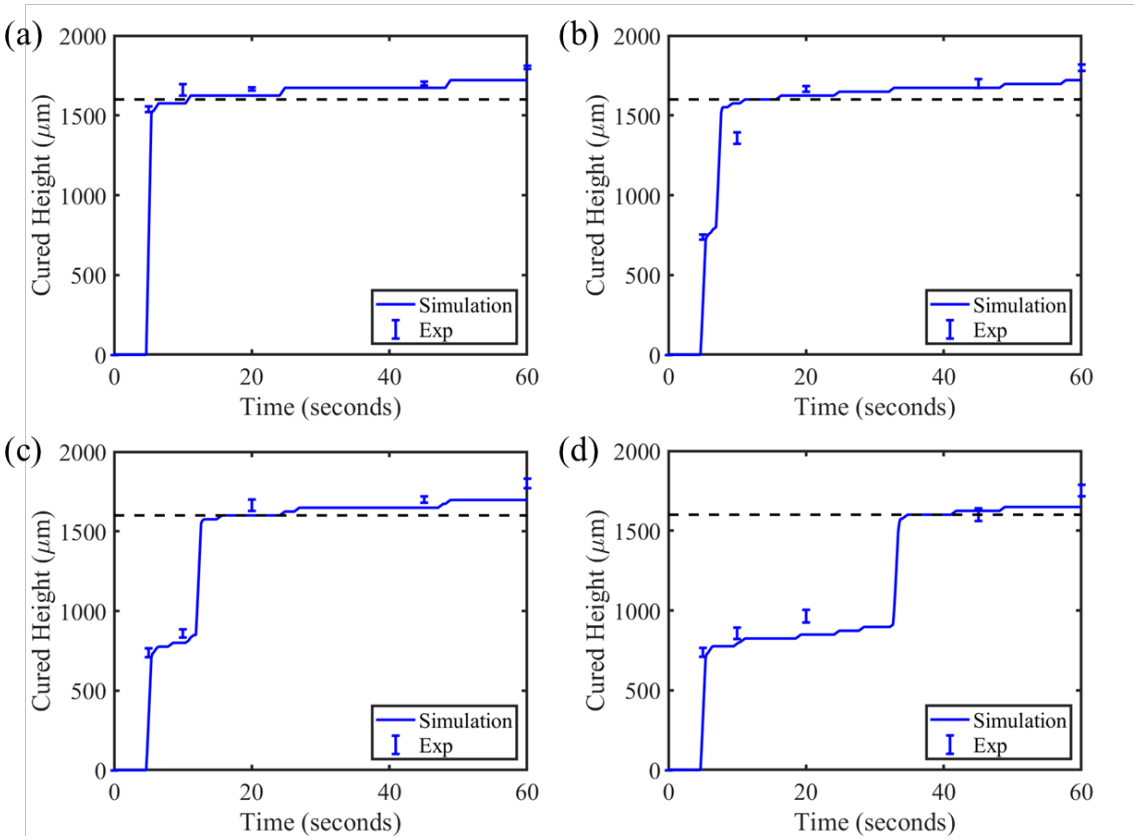

Figure 3.12 Simulation compared to experimentally measured heights for various grayscale patterns. (a) All G0 grayscale pattern. (b) G0 – G40 grayscale pattern. (c) G0 – G60 grayscale pattern. (d) G0 – G80 grayscale pattern.

The experimental results shown in this work only considered visual appearance. With the developed model the DoC across the interface was post-process from the simulations. These results are shown in Figure 3.13 through **Error! Reference source not found.**. The x-axis for all of these figures corresponds to the vertical height through the

entire computational domain. The DoC was directly extracted from the solutions of the governing equations. Figure 3.13 shows the variation of the DoC along this direction for the four grayscale patterns which were already discussed above. The all G0 (Figure 3.13a) case is not that interesting and is used as a control. What can be seen from that is the homogenous distribution of DoC through the interior and the tapering of the DoC at the edges of the printed part, i.e. there is not a discrete transition between the solid printed structure and the liquid reservoir. For the other cases (Figure 3.13b-d) a slope between the two regions can be seen showing a gradient of DoC from a region cured with one light intensity to another.

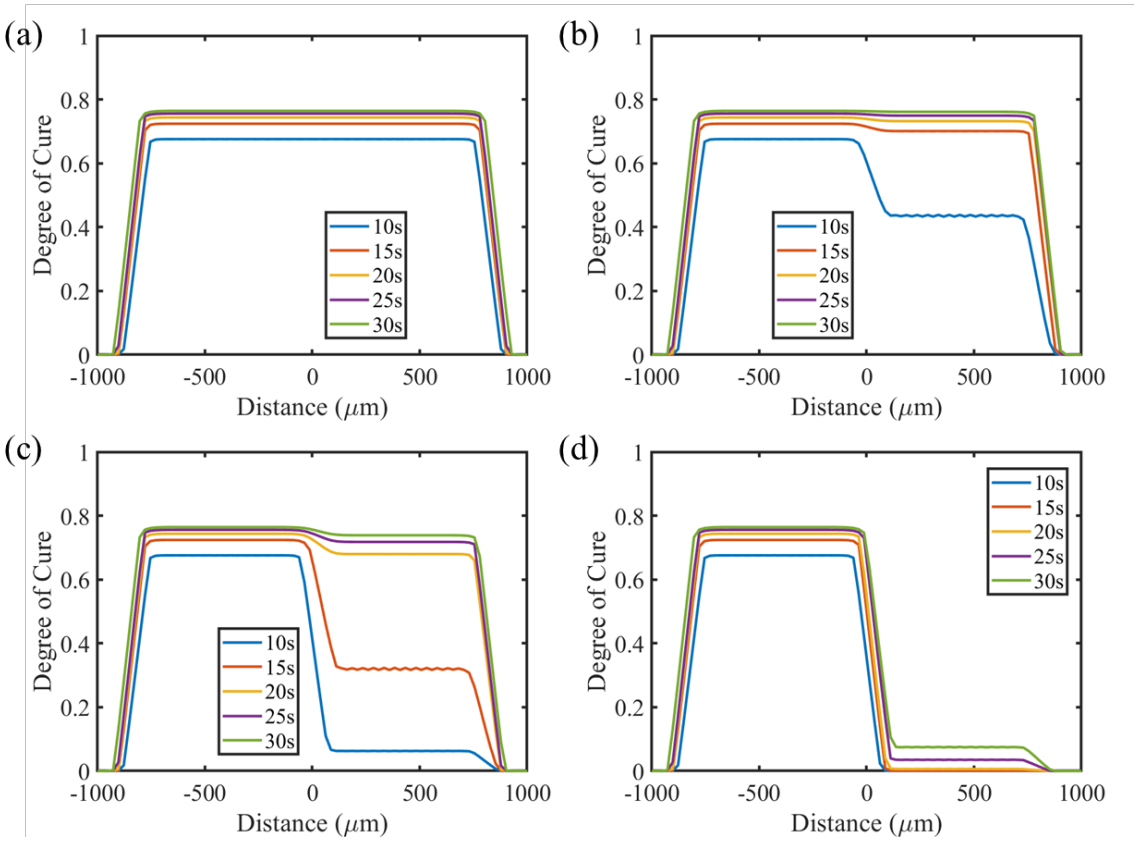

Figure 3.13 DOC through the vertical width of the simulated grayscale patterns (a) All G0. (b) G0 – G40. (c) G0 – G60. (d) G0 – G80.

Figure 3.14 shows a finer scale of the interface with a 500µm window to make the gradient clearer. Again, for the case of all G0 there is not much interesting going on other than a gradual increase of the DoC eventually plateauing after 30 seconds. For the other cases it can be seen that there is a region of about 100-150µm where there is a transition region between one degree of network connectivity and another. These results can inform the proper design of new light patterns used for grayscale DLP 3D printing with the end goal of locally tailoring the material properties and minimizing this phenomenon shown in these results. Although these results are purely numerical, they could be verified using FTIR data sampled from several points across the interface to aid in tuning of the model presented.

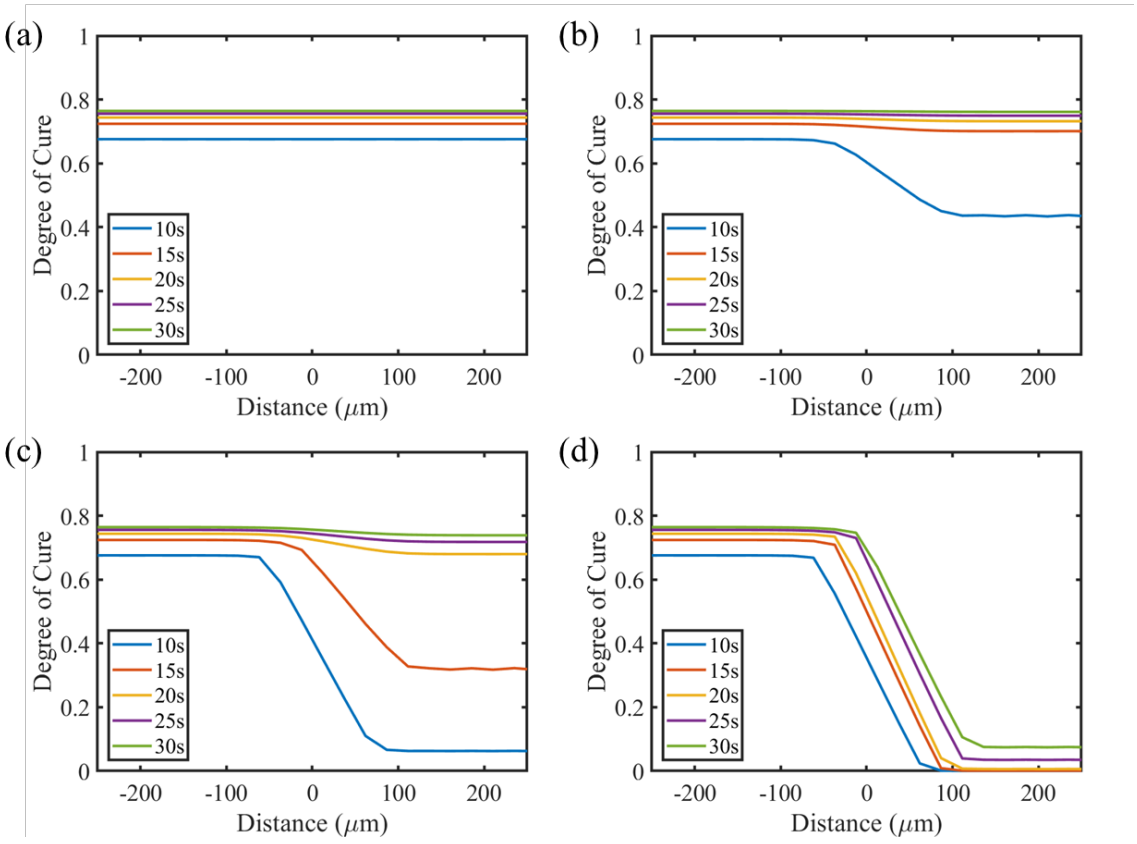

Figure 3.14 DOC through the vertical width of the simulated grayscale patterns (a) All G0. (b) G0 – G40. (c) G0 – G60. (d) G0 – G80.

3.7 Conclusions

In this chapter a reaction-diffusion model for photopolymerization in DLP 3D printing was presented and implemented numerically using the finite difference method. Numerical solutions were compared with simple experiments conducted where a single layer was printed with moderately sized pixel arrays of different grayscale light patterns. The model was calibrated in a stepwise fashion where the kinetics portion of the model was calibrated independently from the species transport from FTIR experiments. Boundary conditions for radiative transfer were given great attention to develop a high-fidelity processing model that could be used to gain insight into the highly complex coupled multi-physics phenomenon present in DLP 3D printing. Future work using this model could incorporate design new grayscale patterns for local modulus tailoring that can allow for fast, efficient, one material process for producing composite materials with novel properties and uses.

CHAPTER 4. DISSOLUTION OF POLYMERS

Thermosetting polymers involving dynamic bonds or exchange reactions (also known as vitrimers) can be fully dissolved in a solvent utilizing a small molecule participated bond-exchange reaction (BER). The dissolution of the polymer network is achieved by selectively cleaving chemical bonds on polymer chains into short segments or clusters through the participation of BER by small molecules. However, the dissolution is a complex process that couples chemical reactions with diffusion featured by varied diffusivity both in time and dimension. Here, a reaction-diffusion model is developed for vitrimer dissolution in alcohol via transesterification. We developed a mathematical model involving both mass transport by diffusion and transesterification kinetics to trace the dissolution behavior of vitrimer samples for various temperatures and solvents. By following the concentration of functional groups and using classical gel theory, the evolution of the mass loss can be obtained. The numerical simulations lead to a quantitative description of the diffusion and dissolution processes. Simulation results are consistent with experimental results, showing good prediction for the size and mass evolution using different dissolution times, temperatures, and solvent choice. This work provides a deep insight into the reaction-diffusion process, which can be used to guide the future development and optimize recycling processes using dynamic bonds. The work presented in this chapter was published in *Macromolecules* [124].

4.1 Introduction

Thermosetting polymers are high performance materials finding wide industrial usage such as coatings, electronic packaging, and as a matrix material for high-performance

composites. After curing, these materials are chemically crosslinked and cannot flow upon heating and thus cannot be reshaped, recycled, or degraded easily. Normally, harsh chemicals, high temperature, and high-pressure conditions are necessary to decompose thermosetting polymers[125-127]. The recent development of thermosetting polymers containing dynamic bonds or labile bonds makes it possible to recycle or degrade chemically crosslinked materials under mild condition[35, 38, 128-130]. Leibler and co-workers have developed an epoxy vitrimer that can undergo transesterification bond exchange reactions (BERs) between the hydroxyl group and ester bond[131-133]. Soon after that, various vitrimers containing different dynamic bonds, such as disulfide exchange reactions[43, 134, 135], Schiff-base reversible reactions[45, 136-139], as well as transesterification reactions[131, 140] have been developed to achieve exciting applications, such as malleability, recycling, surface welding and self-healing properties. More recently, the exchange reaction of vitrimer was used as a dissolution recycling mechanism if properly activated by a catalyst and proper solvent. For example, the vitrimer containing dynamic disulfide bonds can be depolymerized in thiol-containing solvent[41, 42, 141]. Similarly, the fatty acid cured thermosetting vitrimer containing ester linkages can be dissolved in ethylene glycol (EG) at high temperature[47, 49, 142]. The oligomeric components of the depolymerized networks could further be extracted for repolymerization into the original material by evaporating the alcohol at elevated temperatures[49, 51] or reused for high value products[50]. Moreover, industrial grade anhydride-epoxy thermosetting polymers and composites could be dissolved in an alcohol-catalyst solution[142-144]. The solvent-assisted thermosetting polymer dissolution as a recycling mechanism was also used in other different chemistries and materials[45, 145]. This kind

of solvent-based dissolution provides a green and low-cost recycling method for both thermosetting polymers and composites.

The small molecule assisted vitrimer dissolution is a very complex process coupled with solvent/catalyst diffusion and reactions. For example, when a solvent is used in ester containing epoxy vitrimer, unlike in conventional vitrimer where BER occurs among long molecular chains and only causes rearrangement of the network, the participation of small molecules (such as alcohol) into the exchange reaction breaks the long chain, causing the dissolution. Therefore, as shown in Figure 4.1, as alcohol diffuses into the network, the network begins to degrade in a way like a surface-erosion and the decomposed polymer chain segments and clusters are carried away with the recycling solution (alcohol solvent). However, a more detailed investigation reveals that there are two moving boundaries, the eroding polymer front and the diffusion front, both being observed by the FTIR spectrum[144]. Previous experimental methods by evaluating the residual mass and dissolution time at different treating conditions have shown the kinetics of polymer dissolution. Similar to the erodible thermoplastic polymer dissolution, important parameters, such as the solvent diffusion coefficient, solvent thermodynamic solubility and temperature played important roles in the dissolution[146-148]. However, the experimental methods cannot correlate the reaction-diffusion coupling and kinetics in detail. For example, it is difficult to experimentally determine how the concentration of alcohol and the intermediate species as well as the cross-linking density evolve during the dissolution process, demanding a more detailed representation of the complex kinetics in theoretical models. A reaction-diffusion model is highly desirable to better understand and

optimize thermosetting polymer dissolution for applications, such as solution-based recycling and drug release[48].

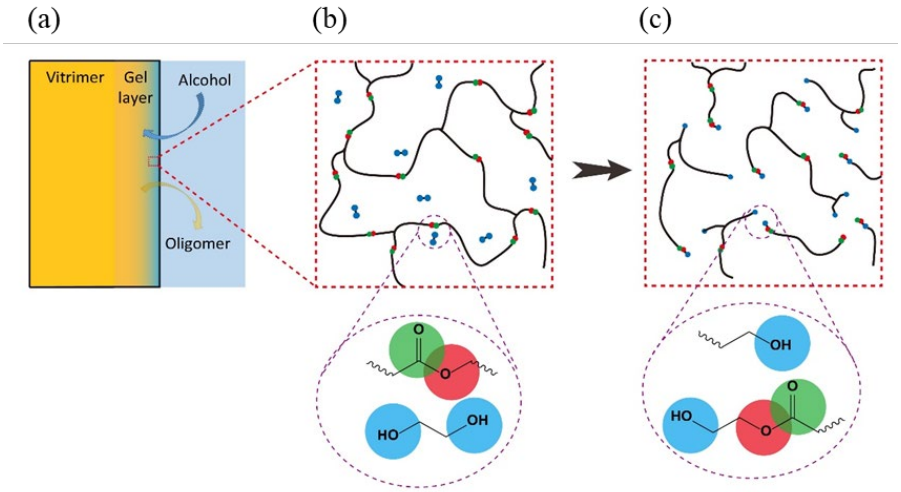

Figure 4.1 Physical mechanisms present in thermosetting polymer dissolution. (a) a schematic graph showing the three distinct regions in the polymer during the dissolution process: the crosslinked vitrimer, a thin layer of solvent diffusion, and the solvent with dissolved vitrimer oligomers. (b) The delivery of alcohol solvent (here EG is shown as the alcohol solvent for illustrative purposes) to an ester linkage. (c) Vitrimer chains after BER.

The major challenge in understanding the dissolution process of vitrimers is due to the diffusion behavior as well as the moving eroding surface and nonuniform swelling[149, 150]. Compared with conventional thermoplastic dissolution, there are two unique features for vitrimer thermosetting polymers: (a) there are several different species with changing chain and cluster sizes during the mass transport process, (b) the diffusivity of different species depends on temperature, time, position and crosslinking density. These features make the analysis of vitrimer dissolution difficult.

The objective of this work is to develop a multiphysics model for vitrimer dissolution by incorporating both mass transport of alcohol solvents and BER kinetics to better

understand the dissolution process. We considered a vitrimer, i.e., the BER catalyst exists in the polymer. Also, we considered the relatively small volume swelling ratio. A set of reaction-diffusion equations for chemical species involved in BERs was developed with non-linear concentration dependent diffusion coefficients. Free-swelling was also incorporated to track the mass-gain and shape distortion from solvent diffusion present during dissolution. The model was implemented numerically and compared with experimental data. We further used the model to predict the distribution of intermediate species during dissolution. Finally, parametric studies were performed to further understand the complex coupled relationship between the BER catalyst reaction rate and solvent diffusivity.

4.2 Materials and Experimental Method

4.2.1 Materials

Bisphenol A di-glycidyl ether (DGEBA) epoxy oligomer, ethylene glycol (EG), diethylene glycol (DG), propylene glycol (PG), and Zinc acetylacetonate (Zn $(Ac)_2$) were obtained from Sigma-Aldrich (St. Louis, MO, USA) and used as received. Fatty acid Pripol 1040 was received from Uniqema Inc. (Paterson, NJ, USA). Silicone mold releasing agent was purchased from Stoner (Quarryvile, PA, USA).

4.2.2 Epoxy Vitrimer Preparation

The epoxy vitrimer was prepared using the method similar to Leibler and co-workers[131]. Briefly, metal catalyst $Zn(Ac)_2$ (with a concentration of 5 mol % to the fatty acid) was mixed with fatty acids Pripol 1040 in a beaker. The temperature was gradually

increased from 100°C to 140°C and then was held at 140°C under vacuum until the production of gases ceased. The catalyst was fully solubilized, yielding a transparent liquid in about 1h. Stoichiometric amounts of di-glycidyl ether of bisphenol A (DGEBA) was added into the fatty acid mixture in open air (with a ratio of COOH and epoxy group of 1:1) at 130°C. The mixture was manually stirred, and then quickly poured into a 10×20×0.6 cm^3 aluminum mold with silicone-based release agent. The mold was placed in a heating oven for at least 6 h at 130°C to ensure fully crosslinked samples.

For dissolution tests, cubic epoxy resin samples with a side length of 6 mm were soaked in alcohol in a glass bottle (with the polymer content of 5 wt% in the solution). The glass containers were sealed with aluminum foil and placed in a heating oven at the designated temperature. At different time intervals, the samples were taken out, cleaned and weighed to monitor the residual mass as a function of time. A similar method was utilized for free swelling tests where the only difference was no catalyst was added to the prepared samples. The samples were soaked in the alcohol for a long enough time such that the swelling response reached a steady state. Due to the lack of catalyst, these samples did not have BER.

4.2.3 Modeling

In this section we develop a continuum level model for vitrimer dissolution. Let us first consider an arbitrary three-dimensional geometry in the reference configuration represented by Ω_R which has a boundary $\partial\Omega_R$. Let $\mathbf{X}$ represent a point in the initially un-swelled reference configuration and let $\mathbf{x}$ be a point in the corresponding swollen current configuration. Using continuum mechanics, we can define a motion $\mathbf{x} = \boldsymbol{\chi}(\mathbf{X}, t)$ that maps

reference points to points in the current domain. Let $C^{\alpha}\left(\mathbf{X},t\right)$ represent the concentration of the α^{th} chemical species and let $\mathbf{j}^{\alpha}\left(\mathbf{X},t\right)$ represent the local flux of the α^{th} chemical species passing through a material point in the reference configuration. We can define the deformation gradient between the two configurations expressed as

$$\mathbf{F}=\frac{\partial \mathbf{x}}{\partial \mathbf{X}}. \tag{4.1}$$

To remain physical, the determinant of the deformation gradient must always be positive

$$J=\det \mathbf{F}>0. \tag{4.2}$$

For the general case, a multiplicative decomposition of the deformation gradient into elastic and swelling parts may be undertaken as follows

$$\mathbf{F}=\mathbf{F}^{e}\mathbf{F}^{s}, \tag{4.3}$$

where $\mathbf{F}^{e}$ is the deformation due to elastic loading and $\mathbf{F}^{s}$ is the deformation due to free-swelling. Equation (4.2) may then be rewritten as

$$J=J^{e}J^{s}=\left(\det \mathbf{F}^{e}\right)\left(\det \mathbf{F}^{s}\right)>0. \tag{4.4}$$

We will restrict our model to the case of isotropic free swelling without other external mechanical loadings so that the deformation gradient may be assumed to be a spherical isotropic tensor taking the form

$$\mathbf{F}=\lambda^{s}\mathbf{I}, \tag{4.5}$$

where λ^{s} is the swelling ratio with $\lambda^{s}>0$ for all time. For the initially un-swollen polymer $\lambda^{s}=1$ and no deformation occurs. Using equations (4.4) and (4.5) it can be shown that

$$J^{s}=\left(\lambda^{s}\right)^{3}>0. \tag{4.6}$$

4.2.3.1 Reaction Kinetics

This section will consider the reaction kinetics at a single material point. The reaction kinetics also depends on the species concentrations, which are captured by the diffusion equations presented in the next section. To assist the study, we chose three different di-functional small molecule alcohol solvents. To better capture the BER at a molecular level we modelled a complete reaction scheme which acknowledges the potential for side reactions between a single di-functional alcohol molecule and fatty acid. This addition adds an additional equation without introducing too much complexity. Reasonable results may still be attained without the addition of side reactions, but this neglects some of the fundamental chemistry occurring throughout the process.

The simplified mechanism is given in Figure 4.2. The main idea is that solvent molecules can dynamically cut the ester bond between the fatty acid and epoxide group, after which, the broken pieces of the network are the epoxy resin with open rings and the fatty acid ester [49]. If this process can proceed for a long enough time, the network begins to break down and dissolves into the solution. Two other reactions can exist due to the di-functional nature of the alcohols utilized, as illustrated in Figure 4.3and Figure 4.4. Briefly, an alcohol molecule bonds to two separate fatty acid molecules and creates either an intermediate species or a potentially undesirable by-product.

To assess the efficiency of the dissolution we first define a crosslinking density such that the remaining mass of bulk polymer can be properly monitored. We define the crosslinking density, which is denoted by p, to be the ratio of ester bonds with linkages, denoted by C^e, currently in the bulk polymer to the amount of ester bonds prior to dissolution, i.e.

$$p = \frac{J^s C^e(t)}{C^e(t=0)}, \tag{4.7}$$

where J^s is the swelling ratio defined in detail later. We say the polymer is in the bulk or swollen state if the crosslinking density is greater than the gel point, $p > p_{gel}$, and we say the local region of polymer chains has dissolved if $p \le p_{gel}$.

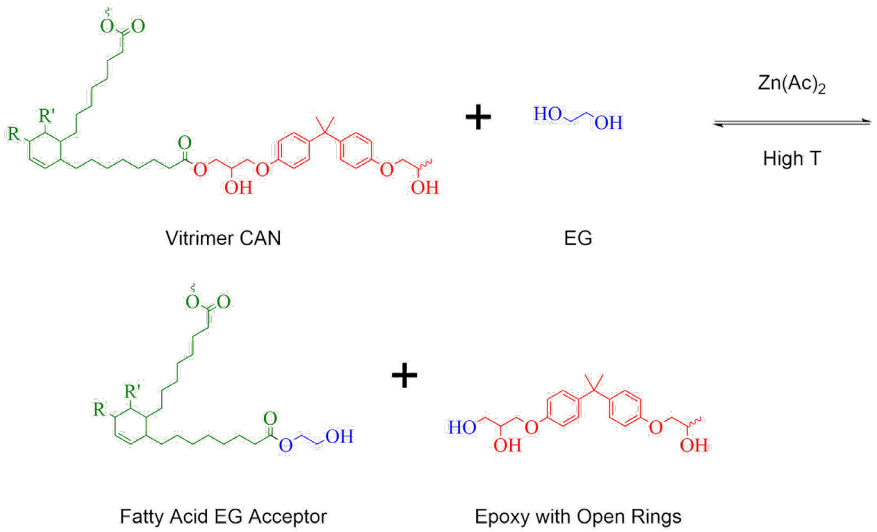

Figure 4.2 Mechanism of vitrimer recycling through transesterification utilizing a di-functional alcohol illustrated in blue. EG is used to illustrate the mechanism of the recycling of epoxy (illustrated in red) and fatty acid (illustrated in green) oligomers.

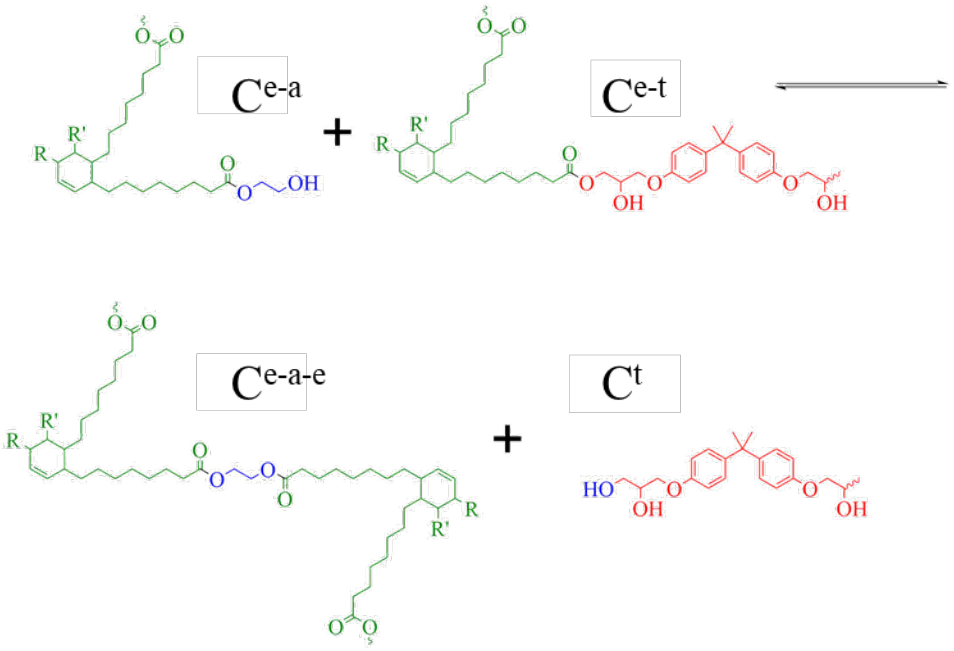

Figure 4.3 Proposed side reaction mechanisms for vitrimer dissolution via transesterification utilizing a di-functional alcohol as a solvent. EG is used to illustrate the role of the solvent but the same mechanism holds for other di-functional solvents. The symbols are the notation we will utilize to represent the concentrations of the functional groups.

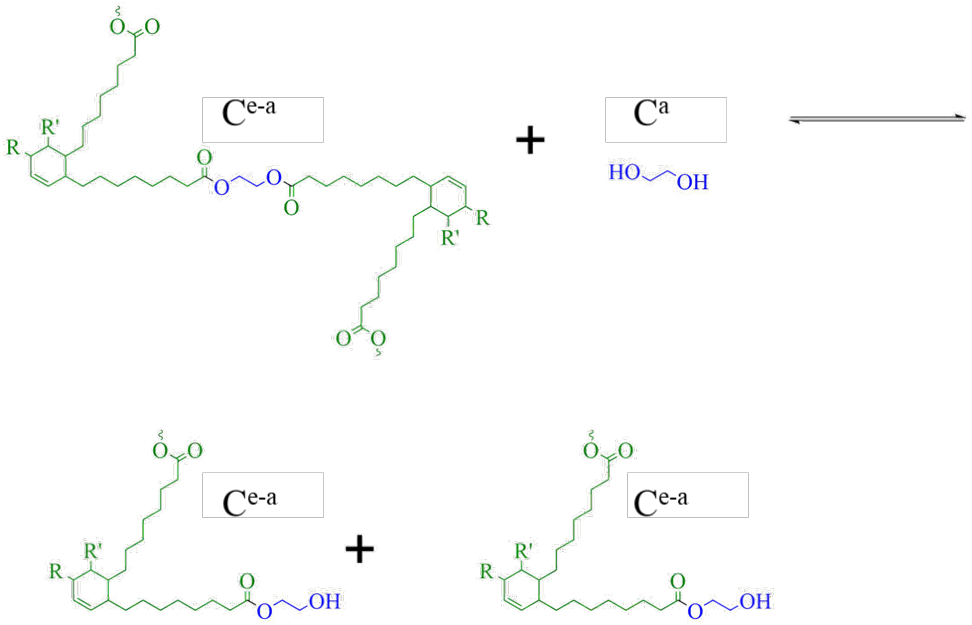

Figure 4.4 Potential side reaction between an alcohol linked to two fatty acid molecules attacked by an EG molecule yielding two EG end-capped fatty acid ester molecules.

The overall mechanism can be broken down into the following three competing reactions,

$$\left[C^{e-t}\right]+\left[C^{a}\right]\underset{k}{\overset{k}{\rightleftharpoons}}\left[C^{e-a}\right]+\left[C^{t}\right], \tag{4.8}$$

$$\left[C^{e-t}\right]+\left[C^{e-a}\right]\underset{k}{\overset{k}{\rightleftharpoons}}\left[C^{t}\right]+\left[C^{e-a-e}\right], \tag{4.9}$$

$$\left[C^{a}\right]+\left[C^{e-a-e}\right]\underset{k}{\overset{k}{\rightleftharpoons}}2\left[C^{e-a}\right]. \tag{4.10}$$

The rates (R) of production/consumption for the chemical species are derived under the assumption that each reaction is second order and may proceed in both directions with the same reaction rate.

$$R^{a}=-kC^{e-t}C^{a}+kC^{e-a}C^{t}-kC^{a}C^{e-a-e}+k\left(C^{e-a}\right)^{2}, \tag{4.11}$$

$$R^{e-a}=-kC^{e-a}C^{t}+kC^{e-t}C^{a}-kC^{e-t}C^{e-a}+kC^{t}C^{e-a-e}-2k\left(C^{e-a}\right)^{2}+kC^{a}C^{e-a-e}, \tag{4.12}$$

$$R^{t} = -kC^{e-a}C^{t} + kC^{a}C^{e-t} - kC^{t}C^{e-a-e} + kC^{e-t}C^{e-a}, \tag{4.13}$$

$$R^{e-a-e} = -kC^{t}C^{e-a-e} + kC^{e-t}C^{e-a} - kC^{a}C^{e-a-e} + k\left(C^{e-a}\right)^{2}, \tag{4.14}$$

$$R^{e-t} = -kC^{a}C^{e-t} + kC^{e-a}C^{t} - kC^{t}C^{e-a-e} + kC^{e-t}C^{e-a}, \tag{4.15}$$

where k is the reaction rate, which in general has a temperature dependence that follows the Arrhenius law,

$$k\left(T\right) = k_{0}\exp\left(\frac{-\Delta E_{BER}}{RT}\right), \tag{4.16}$$

where ΔE_{BER} is the activation energy for the bond exchange reaction and R is the gas constant. The total number of ester bonds within the dissolving vitrimer and the recycling solution should never exceed the initial number of ester bonds in the un-dissolved vitrimer C^{e}. This makes it necessary to impose a reaction constraint upon the ester bonds as follows, with $C^{e} = 0.0028\frac{mol}{mL}$, and the molar volume $\nu_{vitrimer} = 481\frac{mL}{mol}$,

$$2C^{e-a-e} + C^{e-a} + C^{e-t} = \frac{C^{e}}{J^{s}} \tag{4.17}$$

with the relation, $\nu_{0}J^{s} = \nu_{1},$ with ν_{0} being the initial total volume of the sample and ν_{1} the current total volume of the sample. Therefore, the crosslinking density may be expressed in terms of relevant bond concentrations and initial material formulation as follows

$$p\left(\mathbf{X},t\right) = \frac{\frac{C^{e}\left(\mathbf{X},t\right)}{J^{s}} - C^{e-a} - 2C^{e-a-e}}{\frac{C^{e}\left(\mathbf{X},t\right)}{J^{s}}}. \tag{4.18}$$

Equation (4.18) can be further simplified by substitution of equation (4.17) resulting in the following expression

$$p(\mathbf{X},t) = 1 - \frac{J^s C^{e-t}}{C^e(X, t=0)}. \tag{4.19}$$

4.2.3.2 Development of the Reaction-Diffusion Model

We now consider the reaction-diffusion equation. The balance law for species transport can be written in integral form as follows

$$\int_{\Omega_R} \frac{\partial C^\alpha}{\partial t} dv = -\int_{\partial\Omega_R} \mathbf{j}^\alpha \cdot \mathbf{n} da + \int_{\Omega_R} R^\alpha dv, \tag{4.20}$$

where dv is an infinitesimal volume element, da is an infinitesimal area element, $\mathbf{n}$ is the unit vector normal to the surface, and R^α is the reaction rate for species α. After some manipulation via the divergence theorem and the usual assumption of an arbitrary domain, the local law for the balance of chemical species α may be written as

$$\frac{\partial C^\alpha}{\partial t} = -\nabla \cdot \mathbf{j}^\alpha + R^\alpha, \tag{4.21}$$

where R^α is the rate of production of the α^{th} chemical species. According to Fick's laws of diffusion, $\mathbf{j}^\alpha$ is given by the following phenomenologically based constitutive law

$$\mathbf{j}^\alpha = -D^\alpha \nabla C^\alpha. \tag{4.22}$$

Generally, the diffusion coefficient for this problem is non-linear and has a functional dependence upon space, time, temperature, as well as the crosslinking density of the network. This can be expressed in functional form as

$$D^\alpha = \hat{D}^\alpha(T, p). \tag{4.23}$$

Substitution of equations (4.22) and (4.23) into (4.21) gives

$$\frac{\partial C^\alpha}{\partial t} = \nabla \cdot \left(D^\alpha \nabla C^\alpha \right) + R^\alpha. \tag{4.24}$$

We further simplify the functional form of equation (4.23) by assuming that the diffusion coefficient is a separable function in temperature and crosslinking density. Our justification for this assumption is that for a given crosslinking density the diffusion of small molecule solvents into the bulk polymer has a certain Arrhenius type diffusion process. By increasing the crosslinking density, we eliminate more paths for the solvent molecules to proceed thus decreasing the diffusivity but still maintaining the same temperature dependence of the diffusivity, i.e.,

$$D^{\alpha} = D_0^{\alpha} f^{\alpha}\left(T\right) g^{\alpha}\left(p\right), \tag{4.25}$$

where D_0^{α} is reference diffusivity, $f(T)$ is the functional (Arrhenius type) dependence upon temperature and $g\left(p\right)$ is the dependence upon the local crosslinking density of the polymer network. To accommodate for the two distinctly different regions in the dissolving polymer, swollen and un-swollen regions, we utilize an exponential function to accommodate for the sharp dependence of network connectivity on diffusivity as in [151]. For the solvent diffusivity this may be expressed as

$$g^{a}\left(p\right) = \exp\left[\gamma^{a}\left(1-p\right)\right], \tag{4.26}$$

where γ^{a} is a fitting parameter. In the case of the remaining species which may not diffuse unless broken from the network we utilize a piece-wise definition similar to equation (4.26). We express this as follows

$$g^{\alpha}\left(\cdot\right) = \begin{cases} \exp\left[\gamma^{\alpha}\left(1-p\right)\right], & p < p_{gel} \\ 0, & p \geq p_{gel} \end{cases}, \tag{4.27}$$

where γ^{α} is a fitting parameter. Equation (4.27) ensures that polymer chains above the gel point remain bonded to the network and do not diffuse until enough BER has taken place for the chains to be small enough. Therefore, we have

$$D^{\alpha} = D_0^{\alpha} \exp\left(-\frac{\Delta E^{\alpha}}{RT}\right) g^{\alpha}(p). \tag{4.28}$$

The boundary conditions for equation (4.24) are now discussed. We assume that the concentration of the alcohol solution remains constant throughout the liquid medium. This imposes a Dirichlet type boundary condition on the entirety of the vitrimer surface which may be expressed as follows,

$$C_R^a(\mathbf{X}, t) = C_0^a \quad \text{for} \quad \mathbf{X} \in \partial\Omega, \tag{4.29}$$

where C_0^a is the concentration of the liquid medium.

Now we discuss the kinematical constraints imposed upon the material samples by swelling. We assume that the change in the volume of the polymer is due to both an increase of free and chemically trapped alcohol content within the matrix so that we use the following form to describe the volumetric increase

$$J^s = 1 + v_a\left(C^a + C^{e-a-e} + C^{e-a}\right), \tag{4.30}$$

with v_a being the molar volume of the alcohol solvent, or equivalently in terms of swelling ratio as follows

$$\lambda^s = \left[1 + v_a\left(C^a + C^{e-a-e} + C^{e-a}\right)\right]^{\frac{1}{3}}. \tag{4.31}$$

From equation (4.30) it can be easily shown by taking a time derivative of both sides that

the rate of volume change (without BER) is solely due to the rate of alcohol diffusion

$$\dot{J}^s = v_a \left(\dot{C}^a + \dot{C}^{e-a-e} + \dot{C}^{e-a} \right). \tag{4.32}$$

4.2.3.3 Residual Mass during Dissolution

As time progresses the chemical concentrations evolve and there is a coupling between the swelling of the polymer due to solvent diffusion and surface erosion due to transesterification reaction. The system of reaction-diffusion equations described above must be solved numerically due to the strong coupling between different chemical species. We chose to utilize the finite difference method (FDM), implemented in MATLAB (MathWorks Inc. Natick, MA, USA).

Once the concentration profile is known at each time step the local swelling ratio and the crosslinking density may be calculated by utilizing equations (30) and (7), respectively. To calculate the mass of a continuum body the following integral relation may be utilized

$$M(t) = \int_{\Omega_R} \rho(\mathbf{X}, t)\, dv \tag{4.33}$$

The initial density is simply the initial vitrimer density prior to dissolution, $\rho^0 = \rho^{vitrimer}(\mathbf{X}, t = 0)$, and the total density of the body during a time step t is calculated by the average contribution of each species trapped in the vitrimer

$$\rho(\mathbf{X}, t) = \frac{\nu_{vitrimer} C^e}{J^s} \rho^0 + v_a (C^a + C^{e-a} + C^{e-a-e}) \rho^a . \tag{4.34}$$

The residual mass of the vitrimer, in the swollen configuration, may then be calculated using the following integral

$$\frac{M(t)}{M(t=0)} = \frac{1}{M_0} \int_{\Omega(t)} \left[\frac{v_{vitrimer} C^e}{J^s} \rho^0 + v_a (C^a + C^{e-a} + C^{e-a-e}) \rho^a \right] dv. \tag{4.35}$$

Note that in equation (4.35) only the material points with crosslinking density $p > p_{gel}$ contribute to the integral so that only the bulk undissolved polymer contributes to the calculation of the current mass.

4.3 Results and Discussion

4.3.1 Experimental Results

To determine the dependence of vitrimer dissolution on alcohol type and temperature, we performed a series of experiments according to the methods described previously. We chose three different alcohol types (EG, DG, and PG) and three different reaction temperatures (150ºC, 170ºC, and 180ºC). For the control case we prepared epoxy thermosetting polymer samples without embedded catalyst to determine the free-swelling response for each alcohol type and the experimental results are shown in Figure 4.5.

In Figure 4.6 the dissolution profiles at different temperatures are plotted for each solvent utilized. As should be expected the dissolution rate is faster for higher temperatures in all three cases. For the cases of EG and PG, the differences at 170ºC and 180ºC are hardly noticeable but for DG a distinction can still be made. Dissolution can be achieved within four hours for all the three solvents at the highest temperature. Figure 4.6d shows a comparison of the dissolution half-time ($t_{1/2}$) for the three solvents at various temperature. Here, $t_{1/2}$ is defined as the time at which the mass of the remaining bulk polymer is one half

of the initial mass prior to immersion in the recycling solution. The $t_{1/2}$ decreases with increasing temperature. At higher temperatures the difference in $t_{1/2}$ is minimal. As the temperature is lowered, EG and PG begin to perform more efficiently, in terms of solvent delivery speed, than DG due to its sharper temperature dependence. EG has the lowest $t_{1/2}$ at the same treating time than PG. This can be attributed to higher alcohol (or hydroxyl) concentration (C_a) than the other alcohols due to lower molar volume. However, the $t_{1/2}$ is the most sensitive to temperature using PG.

4.3.2 Modeling Results

To compare our model with the experimental results we performed non-linear least square regression utilizing our developed model to fit the unknown material properties and reaction rates to the relevant parameters. The initial and boundary conditions were obtained from determining the alcohol concentration of the recycling solution along with the concentration of functional groups within the vitrimer prior to dissolution and are consistent with our experiments.

The free swelling tests with samples that contained no catalyst were used to obtain the diffusion coefficients. In the absence of catalyst, the transesterification reaction does not take place and the model reduces to a single diffusion equation with a constant scalar diffusion coefficient

$$\frac{\partial C^a}{\partial t} = D_0^a \nabla^2 C^a, \tag{4.36}$$

with a Dirichlet boundary condition on the entire surface $\partial\Omega_R$

$$C^a\left(\mathbf{X},t\right)=C_0^a,\quad \text{for}\quad \mathbf{X}\in\partial\Omega_R. \tag{4.37}$$

The ratio of mass uptake by the bulk polymer in the current configuration can then be expressed as

$$\frac{M\left(t\right)}{M\left(t=0\right)}=\int_{\Omega(t)}\left(1+\nu_a C^a\right)dv. \tag{4.38}$$

Fitting this to experimental data can then give a reference diffusion coefficient, D_0^a and an activation energy ΔE_D for the diffusion process, for each alcohol solvent used in this study.

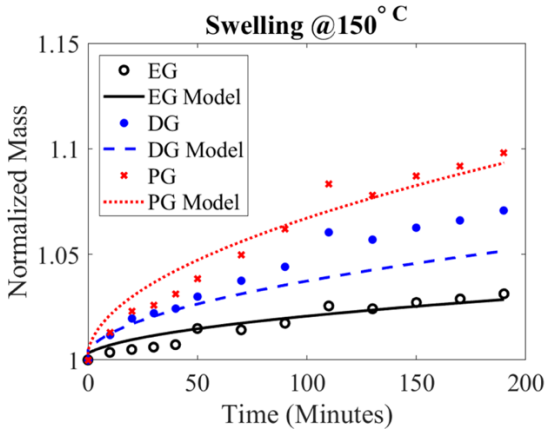

Figure 4.5 Free swelling response and model fitting for different alcohol solvents at 150°C. Experimental data are shown as circles for the corresponding analytical colored curve.

The swelling response of vitrimer cubes immersed in EG, DG, and PG are comparable with little swelling when immersed overnight and even less so within the time frame of the dissolution process. PG has the largest swelling ratio and EG the least significant with DG in the middle. In the absence of embedded catalyst our reduced swelling model fits the experimental data quite well during the typical time period required for dissolution in vitrimers, shown in Figure 4.5. The known molar volumes and density of the alcoholic solvents and vitrimer are shown in Table 4.1 as well as the fitted initial diffusion coefficients and diffusive activation energy for each solvent.

Table 4.1 Model parameters used in the numerical examples

Parameter	Description	Units	Value
$\rho_{vitrimer}$	vitrimer density	kg / m^3	1000
ρ_{EG}	EG density	kg / m^3	1113
v_{EG}	EG molar volume	m^3 / mol	0.0000558
ρ_{DG}	DG density	kg / m^3	1118
v_{DG}	DG molar volume	m^3 / mol	0.0000949
ρ_{PG}	PG density	kg / m^3	1036
v_{PG}	PG molar volume	m^3 / mol	0.0000734
$D_0^{a,EG}$	Reference diffusivity for EG at 150°C	m^2 / s	9.83E-11
ΔE_D^{EG}	Activation energy for diffusion of EG	J / mol	1.76E+04
$D_0^{a,DG}$	Reference diffusivity for DG at 150 °C	m^2 / s	9.93E-11
ΔE_D^{DG}	Activation energy for diffusion of DG	J / mol	1.47E+04

$D_0^{a,PG}$	Reference diffusivity for PG at 150ºC	m^2 / s	1.04E-10
ΔE_D^{PG}	Activation energy for diffusion of PG	J / mol	1.12E+04
k_0	Reference reaction constant	$m^3 / s \cdot mol$	1.1E-09
ΔE_{BER}	BER activation energy	J / mol	79.62E+04
$C^a(\mathbf{X}, t=0)$	Initial alcohol concentration	mol / m^3	0
$C^{e-a}(\mathbf{X}, t=0)$	Initial linked alcohol concentration	mol / m^3	0
$C^{e-a-e}(\mathbf{X}, t=0)$	Initial di-functional linked alcohol concentration	mol / m^3	0
$C^{e-t}(\mathbf{X}, t=0)$	Initial concentration of ester-linkages	mol / m^3	5200
$C^t(\mathbf{X}, t=0)$	Initial hydroxyl concentration	mol / m^3	5200
$C^e(\mathbf{X}, t=0)$	Initial ester concentration	mol / m^3	5200
C_0^a (EG)	Concentration of free alcohol at the boundary	mol / m^3	17800
C_0^a (PG)	Concentration of free alcohol at the boundary	mol / m^3	13600
C_0^a (DG)	Concentration of free alcohol at the boundary	mol / m^3	10550

Temperature has a two-fold effect on the dissolution time. Both the rate of solvent diffusion and the BER cutting rate are temperature dependent. Higher temperatures increase the diffusion and BER rates as well as decreasing the swelling time. Still, a competition exists between the rate at which solvent molecules can be delivered to the ester linkages and the BER rate. Fitted modelling results are shown in Figure 4.6a-c for EG, DG and PG respectively.

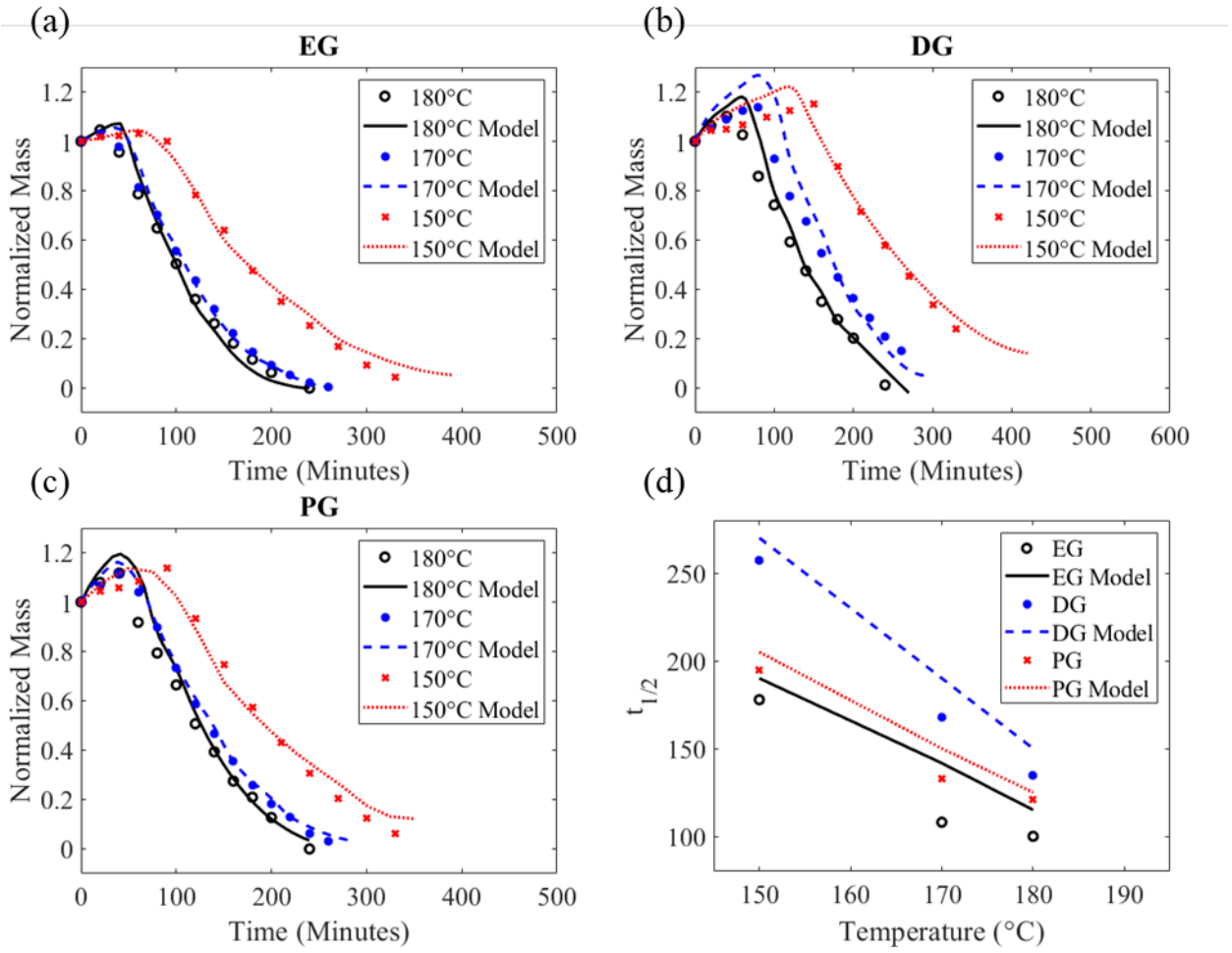

Figure 4.6 Experimental results (shown as circles) compared with fitted modelling results (as solid lines) for (a) EG, (b) DG, (c) PG, (d) and comparison of the half dissolution time for each of the three solvents at various temperatures.

The fitted modelling results compares very well with the experimental results for each temperature and alcohol solvent chosen. DG has the largest dependence upon temperature in terms of dissolution-time with EG and PG showing similar performance. Figure 4.6d shows comparison of the half dissolution time for the experiments and modelling. In each case our model slightly overpredicts the half dissolution time, which can give a conservative estimate of the total time necessary of immersion in the solution such that a maximum number of oligomers may be recovered from the procedure. For all three

solvents the dissolution time decreases with increasing temperature. It would be advantageous in an industrial setting to use a temperature as low as possible (although temperatures below 120^{o}C drastically increases the dissolution time) to reduce the energy costs for dissolution. However, this would increase the treating time for larger samples due to the diffusion process being slowed down at lower temperatures. Therefore, a balance must be found between temperature, treating time, and the solvent utilized to optimize the dissolution process.

4.3.3 Illustrative Numerical Simulations

In the previous section, we quantitatively compared our model to the experimental results by matching the mass dissolution profiles. In this section we illustrate the qualitative aspects of our model by comparing simulation results directly to the images of the experimental results. In reality a simple cubic sample of thermoset will not remain cubic during the dissolution process. The corner of the sample has a large exposure to solvent, leading the corners to be dissolved faster. Due to solvent penetration on all six faces of the cube, there will be an eventual rounding of the sample into a spherical shape.

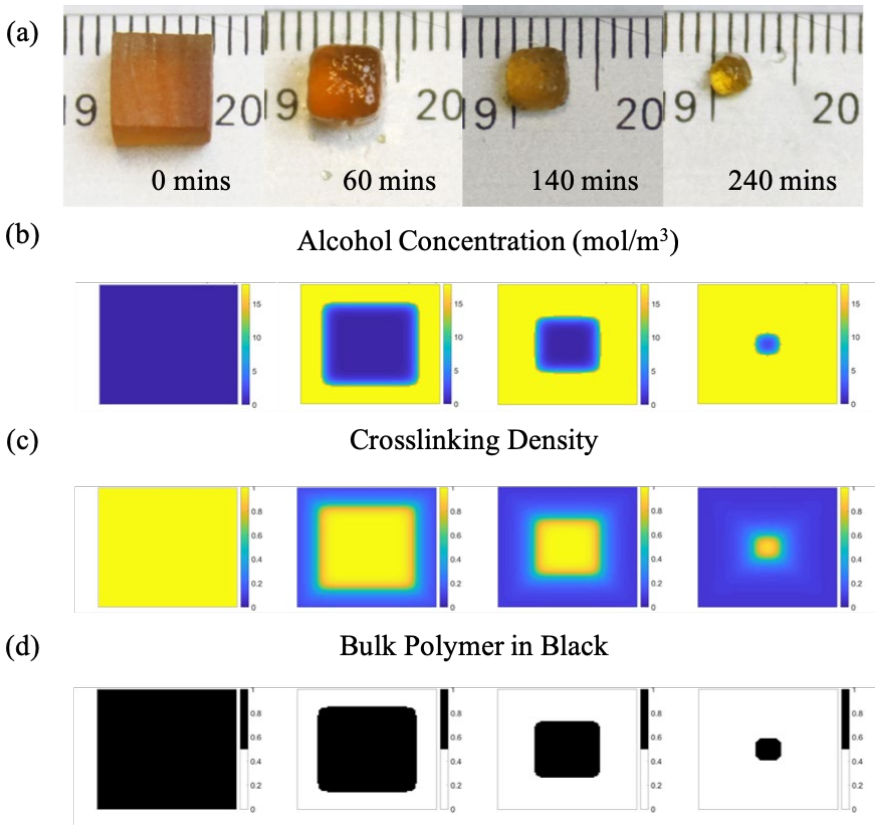

Figure 4.7 Experimental and simulation results for vitrimer dissolution using EG at 170°C. (a) Images are pictures taken directly from experiment with a scale bar for reference. (b) alcohol concentration in mol/L, (c) relative crosslinking density, which is dimensionless, (d) the current solid domain in black and dissolved regions in white. The contours are shown for time 0 min, 60 min, 140 min, and 240 minutes respectively. A 100 x 100 x 100 mesh was utilized as the computational domain and the simulation was run for 10000 times steps.

Figure 4.7a shows the images of the vitrimer cube at different stages of dissolution treated by EG at 170°C. Below those are the alcohol concentration (Figure 4.7b) and crosslinking density (Figure 4.7c) of the cube. Figure 4.7d shows the dissolution process, while the black color denotes the solid domain and the white color represents the absence of bulk polymer in that region. As can be seen our model can capture the shape changing behavior observed as well as predicting the mass loss as shown in the previous section.

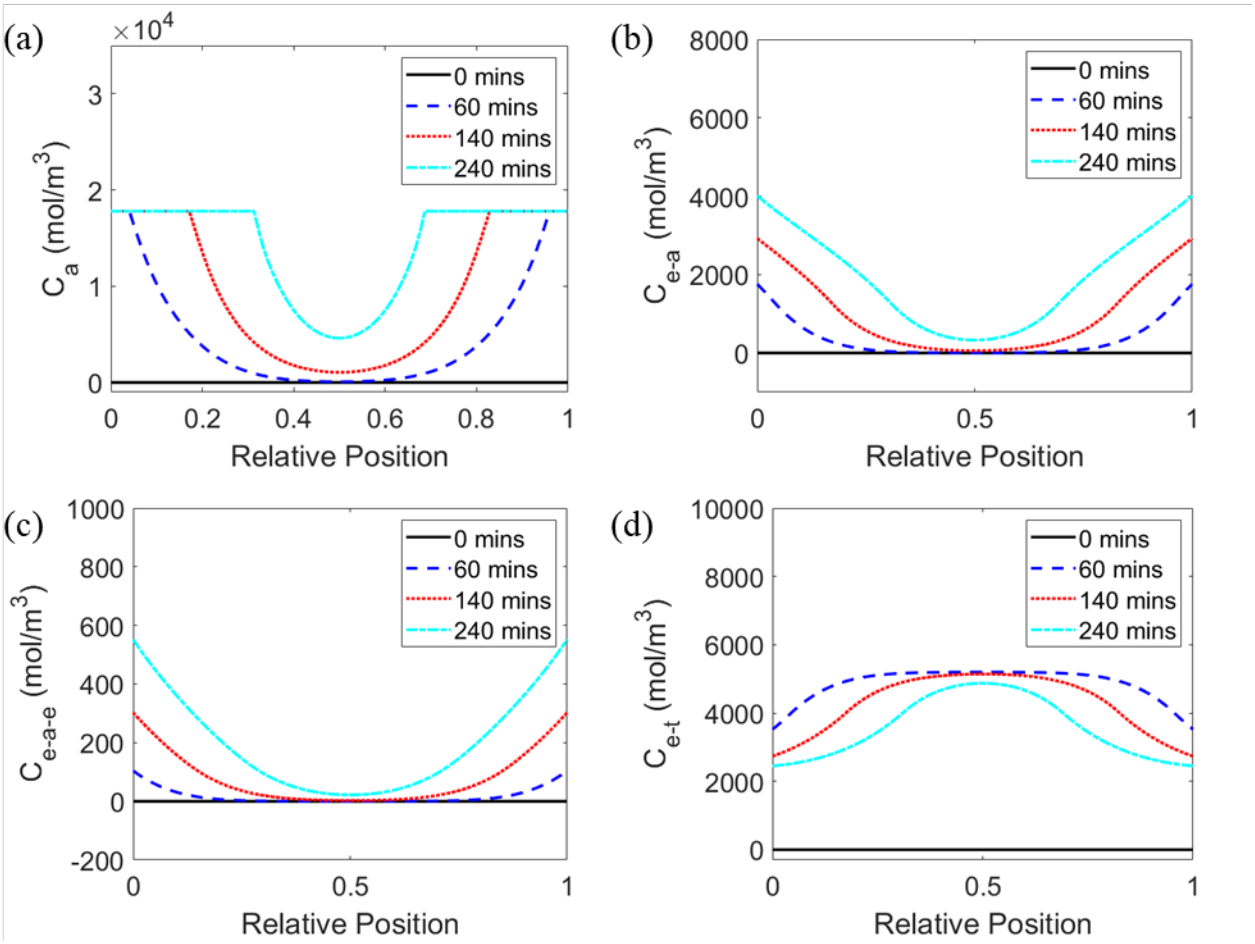

Figure 4.8 (a) Predicted evolution of alcohol concentration, (b) predicted evolution of linked alcohol, (c) predicted evolution of difunctional linked alcohol, and (d) prediction of esther-thiol concentration for the 3D finite difference problem of vitrimer in EG at 170°C.

We further use the model to investigate the cross-linking density and concentration evolution of the different species during dissolution. As mentioned above, local concentration of alcohol solvent is strongly coupled to the BER process. Due to the nonlinear diffusion process there is a moving diffusion front due to the degradation of the vitrimer network. This makes the dissolution process highly diffusion limited since the BER needs to be activated through the alcohol solvent. Figure 4.8a shows the relative alcohol concentration through the thickness of a vitrimer cube at different treating times.

The alcohol can diffuse rapidly into the vitrimer with a fast-moving diffusion front. Before 60 min, the diffusion front has already moved to the center of the material and the eroding front also moves indicating the material dissolution. The alcohol delivered in the network would activate BER to break the polymer linkages. Therefore, we can observe the reduction in the cross-linking density at the center of the material. The results show the strong dependence of crosslinking density on solvent concentration. We also plot the concentration distribution of the intermediate state species as shown in Figure 4.8b-d. These intermediate species are difficult to determine experimentally which adds another benefit to our model in the ability to predict the concentrations of intermediate species during the dissolution process.

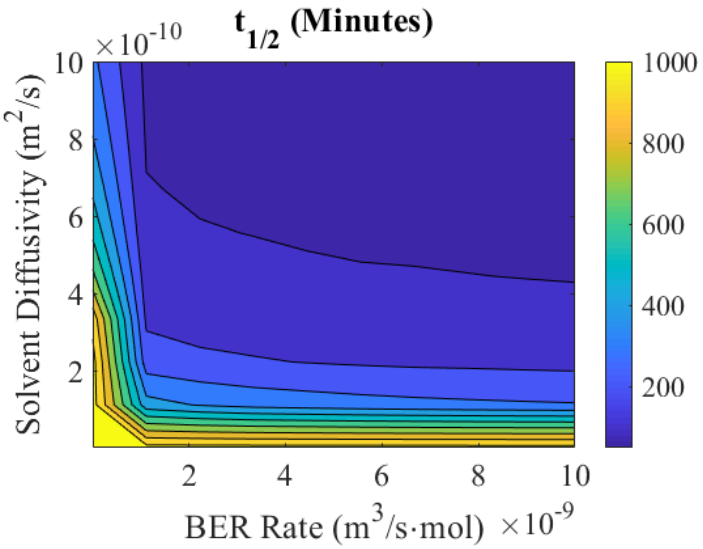

Figure 4.9 Parametric study for the half dissolution time of vitrimer cubes by varying the reaction rate constant and diffusivity.

To gain further insight into the optimization of dissolution-based recycling procedures we performed a parametric study utilizing our model to better understand the complex relationship between BER rate and solvent diffusion. The two major parameters that affect the total dissolution time are the reaction rate of the BER and the solvent diffusivity. To illustrate the coupling effect, we varied the values of these parameters over an entire order of magnitude and plotted the half dissolution time in Figure 4.9. From the contours it can be seen that varying the solvent diffusivity has a more apparent effect upon the half dissolution time. In the lower left corner of the contour plot it is obvious to note that slow diffusion and slow BER cutting rate will lead to the longest dissolution time. Similarly, in the upper right-hand corner the fast diffusion and the fast BER rate lead to the fastest dissolution time which is expected and easy to understand. There are two other extreme cases. For the case of a very poor catalyst, the far left in Figure 4.9, increasing the solvent diffusivity can overcome the slow rate of surface erosion by delivering more solvent into the interior and improve the dissolution rate. In this case, BER rate is the limiting factor, which is also a reaction-rate controlled dissolution process. On the other hand, if a very efficient catalyst is used but if the diffusivity is low (as shown in the bottom-right of Figure 4.9), the dissolution rate is still low as the dissolution only occurs at the surface. In this case, diffusion is the limiting factor, which is a diffusion-rate controlled dissolution process. These two extreme cases suggest that improving diffusivity appear to be more efficient in improving the dissolution process as it can deliver the small molecules inside the material, causing the BER to occur inside the bulk polymer, which provides much higher amount of BERs.

4.4 Conclusions

A reaction-diffusion model incorporating free-swelling was developed for the dissolution driven recycling of thermosetting polymers. A multiphysics model was developed to capture the evolution of all potential functional groups as well as their diffusive nature throughout the dissolution process. The model was implemented by using the finite difference method for a cubic geometry and fitted to experimental data. The model showed good qualitative and quantitative agreement with the experimental results for a range of temperatures as well as different choices of alcohol solvent. Parametric studies were also performed to assess the competition between diffusion and BER reaction rates. We found several distinct cases where the dissolution process was either diffusion controlled, reaction controlled, or somewhere in between. It was found that diffusion of alcohol solvent into the network for the case of vitrimer with embedded catalyst provides the most efficient way to improve the dissolution rate. This modelling effort lays out a basis for the optimization of thermosets for potential industrial applications for non-uniform geometries and may also be applied to further study the recycling of thermosetting polymer-based composites.

CHAPTER 5. CONSLUSION AND FUTURE WORK

This dissertation focuses on the development and implementation of physics-based models to be utilized in different stages of the lifecycle of 3D and 4D printed polymers. An investigation of using machine learning based design approaches is utilized to determine an optimal material distribution for achieving a desired shape change upon application of an external stimulus. Specifically, evolutionary algorithms are utilized due to their great ability in searching large complex discrete design spaces. This method of algorithms is coupled with FEM simulations to determine the quality of each material distribution that are tested. An idealized active composite is used for the development of these methods to reduce the computational complexity of each FEM simulation by using a simple material model which only considers large deformation and actuation is "idealized" into simple thermal expansion with an exaggerated CTE. This method is then extended to incorporate a realistic thermo-viscoelastic material model calibrated from DMA experiments.

The research within also explores the use of reaction-diffusion models with high fidelity photopolymerization reaction kinetics to determine the effect that light patterns and species diffusion has upon the geometrical features of simple square structures. Reasonable agreement is achieved between measurements from printed structures and model predictions. The major contribution in this section of research is the incorporation of light patterns (as boundary conditions for the equation of radiative transfer) and diffusion of free radicals and other chemical species for determining their effect upon geometric resolution of DLP 3D printing structures. Good agreement is seen between the model predictions and the simple experiments conducted.

Polymer dissolution models are also utilized to determine the effect of processing conditions on the rate of recycling for specialty vitrimer based polymers. Good agreement is achieved between experiments and model predictions for a range of different solvents and recycling temperatures. Upon calibration the developed model is also able to make a large range of predictions which normally necessitate a large range of experiments which are time consuming and potentially costly.

The research within this dissertation could be further developed in the following aspects.

1. The machine learning based design approaches for active composites can be further explored by considering several different environmental stimuli other than amorphous SMPs. Possibilities could include hydrogels, dielectric elastomers, magnetic responsive materials, and light activated polymers to name a few. The end goal would be to ascertain whether this method is universal across materials or if it fails due to physics that have not been considered thus far. If it is universal, then refinements to the method would be another branch of future research to speed up the material property distribution discovery and deploy this as a readily available tool for use in industry. Expanding the methods presented within this work to 3D material distributions faces challenges. These challenges could be overcome in several ways. One way is to seed the geometry in a non-uniform way (unlike the work presented here) by using the curvature of a target shape as a seeding metric. This could greatly reduce the number of individual material units which would shrink the design space, thus improving the speed at which the design space can be explored. Another approach would be to start with a course material unit seeding and perform local refinements as another way to reduce the design space. Other

approaches could also be explored such as using different machine learning algorithms, such as neural networks, or using a hybrid approach combining multiple types of algorithms to achieve a material distribution in an efficient way without sacrificing material behavior fidelity.

2. The reaction-diffusion based model for DLP 3D printing should be further investigated for structures other than simple single layer squares. This was a simplified study and could be extended to include complex 3D structures composed of several hundred layers where multiple exposures of previously printed layers become a big issue, especially when material property control is the end goal. Although this would be a difficult undertaking, the model can be further included into a non-linear solid mechanics framework to also account for volume shrinkage, residual stress, and heat transfer. The end goal would be to see how the coupling of these important phenomenon have upon the printed components and how improvements could be made to processing parameters for geometric and material property control.
3. The dissolution model developed in the third part of this work could be further refined to consider recycling of more complex structures other than simple cubes. This work has already been extended to considerations of common thermosetting polymers and composites where there is no embedded catalyst within the structure and has been recently submitted for publication but was left out of this dissertation for brevity.
4. The overall future of this work would be to tie the three parts of the research investigated within together. Given an arbitrary material system, a high-fidelity

model for the three stages of life a polymer sees discussed in this research, and enough experimental data, a hierarchical model which models the full life cycle (not just individual pieces) could be developed. This would be a huge benefit to not only industry, but also fundamental research conducted at universities and other research labs. Such a model would enable the optimization of green "living" material systems which would not require traditional destructive manufacturing.

REFERENCES

1. Wu, J., C. Yuan, Z. Ding, M. Isakov, Y. Mao, T. Wang, M.L. Dunn, and H.J. Qi, *Multi-shape active composites by 3D printing of digital shape memory polymers.* Scientific Reports, 2016. **6**: p. 24224.

2. Lendlein, A., H. Jiang, O. Jünger, and R. Langer, *Light-induced shape-memory polymers.* Nature, 2005. **434**(7035): p. 879-882.

3. Wang, S., M. Decker, D.L. Henann, and S.A. Chester, *Modeling of dielectric viscoelastomers with application to electromechanical instabilities.* Journal of the Mechanics and Physics of Solids, 2016. **95**: p. 213-229.

4. Yuan, C., D.J. Roach, C.K. Dunn, Q. Mu, X. Kuang, C.M. Yakacki, T.J. Wang, K. Yu, and H.J. Qi, *3D printed reversible shape changing soft actuators assisted by liquid crystal elastomers.* Soft Matter, 2017. **13**(33): p. 5558-5568.

5. Devin, J.R., K. Xiao, Y. Chao, C. Kaijuan, and H.J. Qi, *Novel ink for ambient condition printing of liquid crystal elastomers for 4D printing.* Smart Materials and Structures, 2018. **27**(12): p. 125011.

6. Chester, S.A. and L. Anand, *A thermo-mechanically coupled theory for fluid permeation in elastomeric materials: Application to thermally responsive gels.* Journal of the Mechanics and Physics of Solids, 2011. **59**(10): p. 1978-2006.

7. Toh, W., T.Y. Ng, J. Hu, and Z. Liu, *Mechanics of inhomogeneous large deformation of photo-thermal sensitive hydrogels.* International Journal of Solids and Structures, 2014. **51**(25): p. 4440-4451.

8. Lendlein, A. and S. Kelch, *Shape-Memory Polymers.* Angewandte Chemie International Edition, 2002. **41**(12): p. 2034-2057.

9. Lendlein, A. and S. Kelch, *Shape-memory polymers as stimuli-sensitive implant materials.* Clinical Hemorheology and Microcirculation, 2005. **32**(2): p. 105-116.

10. Nguyen, T.D., H. Jerry Qi, F. Castro, and K.N. Long, *A thermoviscoelastic model for amorphous shape memory polymers: Incorporating structural and stress relaxation.* Journal of the Mechanics and Physics of Solids, 2008. **56**(9): p. 2792-2814.

11. Westbrook, K.K., V. Parakh, T. Chung, P.T. Mather, L.C. Wan, M.L. Dunn, and H.J. Qi, *Constitutive Modeling of Shape Memory Effects in Semicrystalline Polymers With Stretch Induced Crystallization.* Journal of Engineering Materials and Technology, 2010. **132**(4): p. 041010-041010-9.

12. Westbrook, K.K., P.H. Kao, F. Castro, Y. Ding, and H. Jerry Qi, *A 3D finite deformation constitutive model for amorphous shape memory polymers: A multi-branch modeling approach for nonequilibrium relaxation processes.* Mechanics of Materials, 2011. **43**(12): p. 853-869.

13. Ge, Q., X. Luo, E.D. Rodriguez, X. Zhang, P.T. Mather, M.L. Dunn, and H.J. Qi, *Thermomechanical behavior of shape memory elastomeric composites.* Journal of the Mechanics and Physics of Solids, 2012. **60**(1): p. 67-83.

14. Ge, Q., H.J. Qi, and M.L. Dunn, *Active materials by four-dimension printing.* Applied Physics Letters, 2013. **103**(13): p. 131901.

15. Ge, Q., K.K. Westbrook, P.T. Mather, M.L. Dunn, and H.J. Qi, *Thermomechanical behavior of a two-way shape memory composite actuator.* Smart Materials and Structures, 2013. **22**(5): p. 055009.

16. Ge, Q., X. Luo, C.B. Iversen, H.B. Nejad, P.T. Mather, M.L. Dunn, and H. Jerry Qi, *A finite deformation thermomechanical constitutive model for triple shape polymeric composites based on dual thermal transitions.* International Journal of Solids and Structures, 2014. **51**(15): p. 2777-2790.

17. Beblo, R.V. and L.M. Weiland, *Light Activated Shape Memory Polymer Characterization.* Journal of Applied Mechanics, 2008. **76**(1).

18. Long, K.N., T.F. Scott, H. Jerry Qi, C.N. Bowman, and M.L. Dunn, *Photomechanics of light-activated polymers.* Journal of the Mechanics and Physics of Solids, 2009. **57**(7): p. 1103-1121.

19. Hamel, C.M., F. Cui, and S.A. Chester, *A finite element method for light activated shape-memory polymers.* International Journal for Numerical Methods in Engineering, 2017. **111**(5): p. 447-473.

20. Ding, Z., C. Yuan, X. Peng, T. Wang, H.J. Qi, and M.L. Dunn, *Direct 4D printing via active composite materials.* Science Advances, 2017. **3**(4).

21. Kuang, X., D.J. Roach, J. Wu, C.M. Hamel, Z. Ding, T. Wang, M.L. Dunn, and H.J. Qi, *Advances in 4D Printing: Materials and Applications.* Advanced Functional Materials, 2018. **0**(0): p. 1805290.

22. Maute, K., A. Tkachuk, J. Wu, H. Jerry Qi, Z. Ding, and M.L. Dunn, *Level Set Topology Optimization of Printed Active Composites.* Journal of Mechanical Design, 2015. **137**(11): p. 111402-111402-13.

23. Associates, W., *Wohlers Report 2018: Additive Manufacturing and 3D Printing State of the Industry : Annual Worldwide Progress Report*. 2018.

24. Zhou, C. and Y. Chen, *Additive manufacturing based on optimized mask video projection for improved accuracy and resolution.* Journal of Manufacturing Processes, 2012. **14**(2): p. 107-118.

25. Xue, D., Y. Wang, and D. Mei, *Multi-step exposure method for improving structure flatness in digital light processing-based printing.* Journal of Manufacturing Processes, 2019. **39**: p. 106-113.

26. Yu, C., J. Schimelman, P. Wang, K.L. Miller, X. Ma, S. You, J. Guan, B. Sun, W. Zhu, and S. Chen, *Photopolymerizable Biomaterials and Light-Based 3D Printing Strategies for Biomedical Applications.* Chemical Reviews, 2020.

27. Wu, J., Z. Zhao, C.M. Hamel, X. Mu, X. Kuang, Z. Guo, and H.J. Qi, *Evolution of material properties during free radical photopolymerization.* Journal of the Mechanics and Physics of Solids, 2018. **112**: p. 25-49.

28. Hafkamp, T., G. van Baars, B. de Jager, and P. Etman, *A feasibility study on process monitoring and control in vat photopolymerization of ceramics.* Mechatronics, 2018. **56**: p. 220-241.

29. Pickering, S., *Recycling technologies for thermoset composite materials—current status.* Composites Part A: Applied Science and Manufacturing, 2006. **37**(8): p. 1206-1215.

30. Zhang, J., V.S. Chevali, H. Wang, and C.-H. Wang, *Current status of carbon fibre and carbon fibre composites recycling.* Composites Part B: Engineering, 2020: p. 108053.

31. Wang, B., S. Ma, S. Yan, and J. Zhu, *Readily recyclable carbon fiber reinforced composites based on degradable thermosets: a review.* Green Chemistry, 2019. **21**(21): p. 5781-5796.

32. García, J.M., G.O. Jones, K. Virwani, B.D. McCloskey, D.J. Boday, G.M. ter Huurne, H.W. Horn, D.J. Coady, A.M. Bintaleb, A.M.S. Alabdulrahman, F. Alsewailem, H.A.A. Almegren, and J.L. Hedrick, *Recyclable, Strong Thermosets and Organogels via Paraformaldehyde Condensation with Diamines.* Science, 2014. **344**(6185): p. 732-735.

33. Hong, M. and E.Y.-X. Chen, *Chemically recyclable polymers: a circular economy approach to sustainability.* Green Chemistry, 2017. **19**(16): p. 3692-3706.

34. Zhao, X., X.-L. Wang, F. Tian, W.-L. An, S. Xu, and Y.-Z. Wang, *A fast and mild closed-loop recycling of anhydride-cured epoxy through microwave-assisted catalytic degradation by trifunctional amine and subsequent reuse without separation.* Green Chemistry, 2019. **21**(9): p. 2487-2493.

35. Ma, S. and D.C. Webster, *Degradable thermosets based on labile bonds or linkages: A review.* Progress in Polymer Science, 2017. **17**: p. 163-171.

36. Kuang, X., G.M. Liu, X. Dong, X.G. Liu, J.J. Xu, and D.J. Wang, *Facile Fabrication of Fast Recyclable and Multiple Self-healing Epoxy Materials through Diels-Alder Adduct Cross-linker.* Journal of Polymer Science Part A: Polymer Chemistry, 2015. **53**(18): p. 2094-2103.

37. Ma, X., W. Guo, Z. Xu, S. Chen, J. Cheng, J. Zhang, M. Miao, and D. Zhang, *Synthesis of degradable hyperbranched epoxy resins with high tensile, elongation, modulus and low-temperature resistance.* Composites Part B: Engineering, 2020. **192**: p. 108005.

38. Yamaguchi, A., T. Hashimoto, Y. Kakichi, M. Urushisaki, T. Sakaguchi, K. Kawabe, K. Kondo, and H. Iyo, *Recyclable carbon fiber-reinforced plastics (CFRP) containing degradable acetal linkages: Synthesis, properties, and chemical recycling.* Journal of Polymer Science Part A: Polymer Chemistry, 2015. **53**(8): p. 1052-1059.

39. Li, Q., S. Ma, S. Wang, Y. Liu, M.A. Taher, B. Wang, K. Huang, X. Xu, Y. Han, and J. Zhu, *Green and Facile Preparation of Readily Dual-Recyclable Thermosetting Polymers with Superior Stability Based on Asymmetric Acetal.* Macromolecules, 2020.

40. Christensen, P.R., A.M. Scheuermann, K.E. Loeffler, and B.A. Helms, *Closed-loop recycling of plastics enabled by dynamic covalent diketoenamine bonds.* Nature Chemistry, 2019. **11**(5): p. 442-448.

41. Takahashi, A., T. Ohishi, R. Goseki, and H. Otsuka, *Degradable epoxy resins prepared from diepoxide monomer with dynamic covalent disulfide linkage.* Polymer, 2016. **82**: p. 319-326.

42. Johnson, L.M., E. Ledet, N.D. Huffman, S.L. Swarner, S.D. Shepherd, P.G. Durham, and G.D. Rothrock, *Controlled Degradation of Disulfide-Based Epoxy Thermosets for Extreme Environments.* Polymer, 2015. **64**(0): p. 84-92.

43. Ruiz de Luzuriaga, A., R. Martin, N. Markaide, A. Rekondo, G. Cabañero, J. Rodríguez, and I. Odriozola, *Epoxy resin with exchangeable disulfide crosslinks to obtain reprocessable, repairable and recyclable fiber-reinforced thermoset composites.* Materials Horizons, 2016. **3**(3): p. 241-247.

44. Wang, C., T.M. Goldman, B.T. Worrell, M.K. McBride, M.D. Alim, and C.N. Bowman, *Recyclable and repolymerizable thiol–X photopolymers.* Materials Horizons, 2018.

45. Taynton, P., H. Ni, C. Zhu, K. Yu, S. Loob, Y. Jin, H.J. Qi, and W. Zhang, *Repairable Woven Carbon Fiber Composites with Full Recyclability Enabled by Malleable Polyimine Networks.* Advanced Materials, 2016. **28**(15): p. 2904-2909.

46. Shen, Y., N. Xu, Y.A. Adraro, B. Wang, Y. Liu, W. Yuan, X. Xu, Y. Huang, and Z. Hu, *Imine or secondary amine-derived degradable polyaminal: low cost matrix resin with high performance.* ACS Sustainable Chemistry & Engineering, 2020.

47. Yu, K., Q. Shi, M.L. Dunn, T.J. Wang, and H.J. Qi, *Carbon Fiber Reinforced Thermoset Composite with Near 100% Recyclability.* Advanced Functional Materials, 2016. **26**(33): p. 6098-6106.

48. Yu, K., H. Yang, B. Dao, Q. Shi, and C.M. Yakacki, *Dissolution of Covalent Adaptable Network Polymers in Organic Solvent.* Journal of the Mechanics and Physics of Solids, 2017. **109**: p. 78-94.

49. Shi, Q., K. Yu, M.L. Dunn, T. Wang, and H.J. Qi, *Solvent Assisted Pressure-Free Surface Welding and Reprocessing of Malleable Epoxy Polymers.* Macromolecules, 2016. **49**(15): p. 5527-5537.

50. Kuang, X., E. Guo, K. Chen, and H.J. Qi, *Extraction of Biolubricant via Chemical Recycling of Thermosetting Polymers.* ACS Sustainable Chemistry & Engineering, 2019. **7**(7): p. 6880-6888.

51. Shi, Q., K. Yu, X. Kuang, X. Mu, C.K. Dunn, M.L. Dunn, T. Wang, and H. Jerry Qi, *Recyclable 3D printing of vitrimer epoxy.* Materials Horizons, 2017. **4**(4): p. 598-607.

52. Liu, T., B. Zhao, and J. Zhang, *Recent development of repairable, malleable and recyclable thermosetting polymers through dynamic transesterification.* Polymer, 2020. **194**: p. 122392.

53. Craig, H., R. Devin, L. Kevin, D. Frederic, D. Martin, and Q. Jerry, *Machine-learning Based Design of Active Composite Structures for 4D Printing.* Smart Materials and Structures, 2019.

54. Fernandes, P., J.M. Guedes, and H. Rodrigues, *Topology optimization of three-dimensional linear elastic structures with a constraint on "perimeter".* Computers & Structures, 1999. **73**(6): p. 583-594.

55. Sigmund, O. and K. Maute, *Topology optimization approaches.* Structural and Multidisciplinary Optimization, 2013. **48**(6): p. 1031-1055.

56. Bendsøe, M.P., *Optimal shape design as a material distribution problem.* Structural optimization, 1989. **1**(4): p. 193-202.

57. Solomonoff, R., *An inductive inference machine, part 2.* Matematika, 1958. **2**(1): p. 139-150.

58. Werbos, P.J., *Beyond Regression: New Tools for Prediction and Analysis in the Behavioral Sciences*. 1975: Harvard University.

59. Rumelhart, D.E., G.E. Hinton, and R.J. Williams, *Learning representations by back-propagating errors.* Nature, 1986. **323**: p. 533.

60. Hochreiter, S. and J. Schmidhuber, *Long Short-Term Memory.* Neural Computation, 1997. **9**(8): p. 1735-1780.

61. Boser, B.E., I.M. Guyon, and V.N. Vapnik, *A training algorithm for optimal margin classifiers*, in *Proceedings of the fifth annual workshop on Computational learning theory*. 1992, ACM: Pittsburgh, Pennsylvania, USA. p. 144-152.

62. Cortes, C. and V. Vapnik, *Support-vector networks.* Machine Learning, 1995. **20**(3): p. 273-297.

63. Langley, P., *The changing science of machine learning.* Machine Learning, 2011. **82**(3): p. 275-279.

64. Oh, K.-S. and K. Jung, *GPU implementation of neural networks.* Pattern Recognition, 2004. **37**(6): p. 1311-1314.

65. Sebe, N., I. Cohen, A. Garg, and T.S. Huang, *Machine Learning in Computer Vision*. 2005: Springer Netherlands.

66. Russakovsky, O., J. Deng, H. Su, J. Krause, S. Satheesh, S. Ma, Z. Huang, A. Karpathy, A. Khosla, M. Bernstein, A.C. Berg, and L. Fei-Fei, *ImageNet Large Scale Visual Recognition Challenge.* International Journal of Computer Vision, 2015. **115**(3): p. 211-252.

67. Li, P. and S. Yamada. *A movie recommender system based on inductive learning*. in *IEEE Conference on Cybernetics and Intelligent Systems, 2004.* 2004.

68. Lund, J. and Y. Ng. *Movie Recommendations Using the Deep Learning Approach*. in *2018 IEEE International Conference on Information Reuse and Integration (IRI)*. 2018.

69. Whitley, D., T. Starkweather, and C. Bogart, *Genetic algorithms and neural networks: optimizing connections and connectivity.* Parallel Computing, 1990. **14**(3): p. 347-361.

70. Muc, A. and W. Gurba, *Genetic algorithms and finite element analysis in optimization of composite structures.* Composite Structures, 2001. **54**(2): p. 275-281.

71. Salonitis, K., D. Chantzis, and V. Kappatos, *A hybrid finite element analysis and evolutionary computation method for the design of lightweight lattice components with optimized strut diameter.* The International Journal of Advanced Manufacturing Technology, 2017. **90**(9): p. 2689-2701.

72. Obayashi, S. *Multidisciplinary design optimization of aircraft wing planform based on evolutionary algorithms*. in *SMC'98 Conference Proceedings. 1998 IEEE International Conference on Systems, Man, and Cybernetics (Cat. No.98CH36218)*. 1998.

73. Cilla, M., E. Borgiani, J. Martínez, G.N. Duda, and S. Checa, *Machine learning techniques for the optimization of joint replacements: Application to a short-stem hip implant.* PLOS ONE, 2017. **12**(9): p. e0183755.

74. Abdi, M., R. Wildman, and I. Ashcroft, *Evolutionary topology optimization using the extended finite element method and isolines.* Engineering Optimization, 2014. **46**(5): p. 628-647.

75. Fran, #231, o.-M.D. Rainville, #233, l.-A. Fortin, Marc-Andr, #233, Gardner, M. Parizeau, C. Gagn, and #233, *DEAP: a python framework for evolutionary algorithms*, in *Proceedings of the 14th annual conference companion on Genetic and evolutionary computation*. 2012, ACM: Philadelphia, Pennsylvania, USA. p. 85-92.

76. #233, l.-A. Fortin, Fran, #231, o.-M.D. Rainville, Marc-Andr, #233, G. Gardner, M. Parizeau, C. Gagn, and #233, *DEAP: evolutionary algorithms made easy.* J. Mach. Learn. Res., 2012. **13**(1): p. 2171-2175.

77. Bäck, T., T. and Fogel, B, and D. Michalewicz, *Evolutionary Computation 1 (Basic Algorithms and Operators)*. 2000.

78. Deb, K., A. Pratap, S. Agarwal, and T. A. M. T. Meyarivan, *A fast and elitist multiobjective genetic algorithm: NSGA-II*. Vol. 6. 2002. 182-197.

79. Arruda, E.M. and M.C. Boyce, *A three-dimensional constitutive model for the large stretch behavior of rubber elastic materials.* Journal of the Mechanics and Physics of Solids, 1993. **41**(2): p. 389-412.

80. Ge, Q., A.H. Sakhaei, H. Lee, C.K. Dunn, N.X. Fang, and M.L. Dunn, *Multimaterial 4D Printing with Tailorable Shape Memory Polymers.* Scientific Reports, 2016. **6**: p. 31110.

81. Yuan, C., Z. Ding, T.J. Wang, M.L. Dunn, and H.J. Qi, *Shape forming by thermal expansion mismatch and shape memory locking in polymer/elastomer laminates.* Smart Materials and Structures, 2017. **26**(10): p. 105027.

82. Sydney Gladman, A., E.A. Matsumoto, R.G. Nuzzo, L. Mahadevan, and J.A. Lewis, *Biomimetic 4D printing.* Nature Materials, 2016. **15**: p. 413.

83. Han, D., Z. Lu, S.A. Chester, and H. Lee, *Micro 3D Printing of a Temperature-Responsive Hydrogel Using Projection Micro-Stereolithography.* Scientific Reports, 2018. **8**(1): p. 1963.

84. Kim, Y., H. Yuk, R. Zhao, S.A. Chester, and X. Zhao, *Printing ferromagnetic domains for untethered fast-transforming soft materials.* Nature, 2018. **558**(7709): p. 274-279.

85. Zhao, R., Y. Kim, S.A. Chester, P. Sharma, and X. Zhao, *Mechanics of hard-magnetic soft materials.* Journal of the Mechanics and Physics of Solids, 2019. **124**: p. 244-263.

86. Chester, S.A. and L. Anand, *A coupled theory of fluid permeation and large deformations for elastomeric materials.* Journal of the Mechanics and Physics of Solids, 2010. **58**(11): p. 1879-1906.

87. Beckers, M., *Topology optimization using a dual method with discrete variables.* Structural optimization, 1999. **17**(1): p. 14-24.

88. Sossou, G., F. Demoly, H. Belkebir, H.J. Qi, S. Gomes, and G. Montavon, *Design for 4D printing: A voxel-based modeling and simulation of smart materials.* Materials & Design, 2019. **175**: p. 107798.

89. Sossou, G., F. Demoly, H. Belkebir, H.J. Qi, S. Gomes, and G. Montavon, *Design for 4D printing: Modeling and computation of smart materials distributions.* Materials & Design, 2019. **181**: p. 108074.

90. Boyce, M.C., D.M. Parks, and A.S. Argon, *Large inelastic deformation of glassy polymers. part I: rate dependent constitutive model.* Mechanics of Materials, 1988. **7**(1): p. 15-33.

91. Gurtin, M.E. and L. Anand, *The decomposition F=FeFp, material symmetry, and plastic irrotationality for solids that are isotropic-viscoplastic or amorphous.* International Journal of Plasticity, 2005. **21**(9): p. 1686-1719.

92. Simo, J.C., *On a fully three-dimensional finite-strain viscoelastic damage model: Formulation and computational aspects.* Computer Methods in Applied Mechanics and Engineering, 1987. **60**(2): p. 153-173.

93. Williams, M.L., R.F. Landel, and J.D. Ferry, *The Temperature Dependence of Relaxation Mechanisms in Amorphous Polymers and Other Glass-forming Liquids.* Journal of the American Chemical Society, 1955. **77**(14): p. 3701-3707.

94. Zhao, Z., J. Wu, X. Mu, H. Chen, H.J. Qi, and D. Fang, *Desolvation Induced Origami of Photocurable Polymers by Digit Light Processing.* Macromolecular Rapid Communications, 2017. **38**(13): p. 1600625.

95. Jiangtao, W., Z. Zeang, K. Xiao, M.H. Craig, F. Daining, and H.J. Qi, *Reversible shape change structures by grayscale pattern 4D printing.* Multifunctional Materials, 2018. **1**(1): p. 015002.

96. Kowsari, K., B. Zhang, S. Panjwani, Z. Chen, H. Hingorani, S. Akbari, N.X. Fang, and Q. Ge, *Photopolymer formulation to minimize feature size, surface roughness, and stair-stepping in digital light processing-based three-dimensional printing.* Additive Manufacturing, 2018. **24**: p. 627-638.

97. Kuang, X., Z. Zhao, K. Chen, D. Fang, G. Kang, and H.J. Qi, *High-Speed 3D Printing of High-Performance Thermosetting Polymers via Two-Stage Curing.* Macromolecular Rapid Communications, 2018. **39**(7): p. 1700809.

98. Mostafa, K., A.J. Qureshi, and C. Montemagno, *Tolerance Control Using Subvoxel Gray-Scale DLP 3D Printing.* 2017(58356): p. V002T02A035.

99. Jariwala, A.S., F. Ding, X. Zhao, and D.W. Rosen, *A Process Planning Method for Thin Film Mask Projection Micro-Stereolithography.* 2009(48999): p. 685-694.

100. Zhou, C. and Y. Chen, *Calibrating Large-area Mask Projection Stereolithography for Its Accuracy and Resolution Improvements*. 2009.

101. You, S., P. Wang, J. Schimelman, H.H. Hwang, and S. Chen, *High-fidelity 3D printing using flashing photopolymerization.* Additive Manufacturing, 2019. **30**: p. 100834.

102. You, S., J. Guan, J. Alido, H.H. Hwang, R. Yu, L. Kwe, H. Su, and S. Chen, *Mitigating Scattering Effects in Light-based 3D Printing Using Machine Learning.* Journal of Manufacturing Science and Engineering, 2020: p. 1-23.

103. Fang, N., C. Sun, and X. Zhang, *Diffusion-limited photopolymerization in scanning micro-stereolithography.* Applied Physics A, 2004. **79**(8): p. 1839-1842.

104. Yoshida, S., Y. Takahata, S. Horiuchi, H. Kurata, and M. Yamamoto, *Numerical Model of Radical Photopolymerization Based on Interdiffusion.* International Journal of Polymer Science, 2014. **2014**: p. 8.

105. Hennessy, M., A. Vitale, J. Cabral, and O. Matar, *Role of heat generation and thermal diffusion during frontal photopolymerization*. Vol. 92. 2015.

106. Westbeek, S., J.A.W. van Dommelen, J.J.C. Remmers, and M.G.D. Geers, *Multiphysical modeling of the photopolymerization process for additive manufacturing of ceramics.* European Journal of Mechanics - A/Solids, 2018. **71**: p. 210-223.

107. Meenakshisundaram, V., L.D. Sturm, and C.B. Williams, *Modeling A Scanning-Mask Projection Vat Photopolymerization System For Multiscale Additive Manufacturing.* Journal of Materials Processing Technology, 2020. **279**: p. 116546.

108. Rehbein, T., A. Lion, M. Johlitz, and A. Constantinescu, *Experimental investigation and modelling of the curing behaviour of photopolymers.* Polymer Testing, 2020. **83**: p. 106356.

109. Taki, K., *A Simplified 2D Numerical Simulation of Photopolymerization Kinetics and Oxygen Diffusion–Reaction for the Continuous Liquid Interface Production (CLIP) System.* Polymers, 2020. **12**(4).

110. Chandrasekhar, S., *Radiative Transfer*. 1960: Dover Publications.

111. Sun, C. and X. Zhang, *Experimental and numerical investigations on microstereolithography of ceramics.* Journal of Applied Physics, 2002. **92**(8): p. 4796-4802.

112. Goodner, M.D. and C.N. Bowman, *Modeling Primary Radical Termination and Its Effects on Autoacceleration in Photopolymerization Kinetics.* Macromolecules, 1999. **32**(20): p. 6552-6559.

113. Dendukuri, D., P. Panda, R. Haghgooie, J.M. Kim, T.A. Hatton, and P.S. Doyle, *Modeling of Oxygen-Inhibited Free Radical Photopolymerization in a PDMS Microfluidic Device.* Macromolecules, 2008. **41**(22): p. 8547-8556.

114. Zhao, Z., X. Mu, J. Wu, H.J. Qi, and D. Fang, *Effects of oxygen on interfacial strength of incremental forming of materials by photopolymerization.* Extreme Mechanics Letters, 2016. **9**: p. 108-118.

115. Long, R., H.J. Qi, and M.L. Dunn, *Thermodynamics and mechanics of photochemcially reacting polymers.* Journal of the Mechanics and Physics of Solids, 2013. **61**(11): p. 2212-2239.

116. Buback, M., B. Huckestein, and G.T. Russell, *Modeling of termination in intermediate and high conversion free radical polymerizations.* Macromolecular Chemistry and Physics, 1994. **195**(2): p. 539-554.

117. O'Shaughnessy, B. and J. Yu, *Autoacceleration in Free Radical Polymerization.* Physical Review Letters, 1994. **73**(12): p. 1723-1726.

118. Buback, M., P. Hesse, R.A. Hutchinson, P. Kasák, I. Lacík, M. Stach, and I. Utz, *Kinetics and Modeling of Free-Radical Batch Polymerization of Nonionized Methacrylic Acid in Aqueous Solution.* Industrial & Engineering Chemistry Research, 2008. **47**(21): p. 8197-8204.

119. Buback, M., *Free-radical polymerization up to high conversion. A general kinetic treatment.* Die Makromolekulare Chemie, 1990. **191**(7): p. 1575-1587.

120. Dickey, M.D. and C.G. Willson, *Kinetic parameters for step and flash imprint lithography photopolymerization.* AIChE Journal, 2006. **52**(2): p. 777-784.

121. Crank, J., *The mathematics of diffusion / by J. Crank*. Oxford science publications. 1975, Oxford [England]: Clarendon Press.

122. Gurtin, M.E., E. Fried, and L. Anand, *The Mechanics and Thermodynamics of Continua*. 2010, Cambridge: Cambridge University Press.

123. Kuang, X., J. Wu, K. Chen, Z. Zhao, Z. Ding, F. Hu, D. Fang, and H.J. Qi, *Grayscale digital light processing 3D printing for highly functionally graded materials.* Science Advances, 2019. **5**(5): p. eaav5790.

124. Hamel, C.M., X. Kuang, K. Chen, and H.J. Qi, *Reaction-Diffusion Model for Thermosetting Polymer Dissolution through Exchange Reactions Assisted by Small-Molecule Solvents.* Macromolecules, 2019. **52**(10): p. 3636-3645.

125. Wang, Y., X. Cui, H. Ge, Y. Yang, Y. Wang, C. Zhang, J. Li, T. Deng, Z. Qin, and X. Hou, *Chemical Recycling of Carbon Fiber Reinforced Epoxy Resin Composites via Selective Cleavage of the Carbon–Nitrogen Bond.* ACS Sustainable Chemistry & Engineering, 2015. **3**(12): p. 3332-3337.

126. Xu, P., J. Li, and J. Ding, *Chemical recycling of carbon fibre/epoxy composites in a mixed solution of peroxide hydrogen and N,N-dimethylformamide.* Composites Science and Technology, 2013. **82**: p. 54-59.

127. Morales Ibarra, R., M. Sasaki, M. Goto, A.T. Quitain, S.M. García Montes, and J.A. Aguilar-Garib, *Carbon fiber recovery using water and benzyl alcohol in subcritical and supercritical conditions for chemical recycling of thermoset composite materials.* Journal of Material Cycles and Waste Management, 2015. **17**(2): p. 369-379.

128. Ma, S., D.C. Webster, and F. Jabeen, *Hard and Flexible, Degradable Thermosets from Renewable Bioresources with the Assistance of Water and Ethanol.* Macromolecules, 2016. **49**(10): p. 3780-3788.

129. Snyder, R.L., D.J. Fortman, G.X. De Hoe, M.A. Hillmyer, and W.R. Dichtel, *Reprocessable Acid-Degradable Polycarbonate Vitrimers.* Macromolecules, 2018. **51**(2): p. 389-397.

130. Luo, K., T. Xie, and J. Rzayev, *Synthesis of thermally degradable epoxy adhesives.* Journal of Polymer Science Part A: Polymer Chemistry, 2013. **51**(23): p. 4992-4997.

131. Montarnal, D., M. Capelot, F. Tournilhac, and L. Leibler, *Silica-Like Malleable Materials from Permanent Organic Networks.* Science, 2011. **334**(6058): p. 965-968.

132. Capelot, M., M.M. Unterlass, F. Tournilhac, and L. Leibler, *Catalytic Control of the Vitrimer Glass Transition.* ACS Macro Letters, 2012. **1**(7): p. 789-792.

133. Capelot, M., D. Montarnal, F. Tournilhac, and L. Leibler, *Metal-Catalyzed Transesterification for Healing and Assembling of Thermosets.* Journal of the American Chemical Society, 2012. **134**(18): p. 7664-7667.

134. Lei, Z.Q., H.P. Xiang, Y.J. Yuan, M.Z. Rong, and M.Q. Zhang, *Room-Temperature Self-Healable and Remoldable Cross-linked Polymer Based on the Dynamic Exchange of Disulfide Bonds.* Chemistry of Materials, 2014. **26**(6): p. 2038-2046.

135. Barcan, G.A., X. Zhang, and R.M. Waymouth, *Structurally Dynamic Hydrogels Derived from 1,2-Dithiolanes.* Journal of the American Chemical Society, 2015. **137**(17): p. 5650-3.

136. Taynton, P., K. Yu, R.K. Shoemaker, Y. Jin, H.J. Qi, and W. Zhang, *Heat- or water-driven malleability in a highly recyclable covalent network polymer.* Adv Mater, 2014. **26**(23): p. 3938-42.

137. Taynton, P., C. Zhu, S. Loob, R. Shoemaker, J. Pritchard, Y. Jin, and W. Zhang, *Re-healable polyimine thermosets: polymer composition and moisture sensitivity.* Polymer Chemistry, 2016. **7**(46): p. 7052-7056.

138. Zou, Z., C. Zhu, Y. Li, X. Lei, W. Zhang, and J. Xiao, *Rehealable, fully recyclable, and malleable electronic skin enabled by dynamic covalent thermoset nanocomposite.* Science Advances, 2018. **4**(2): p. eaaq0508.

139. Zhao, S. and M.M. Abu-Omar, *Recyclable and Malleable Epoxy Thermoset Bearing Aromatic Imine Bonds.* Macromolecules, 2018. **51**(23): p. 9816-9824.

140. Pei, Z., Y. Yang, Q. Chen, E.M. Terentjev, Y. Wei, and Y. Ji, *Mouldable liquid-crystalline elastomer actuators with exchangeable covalent bonds.* Nat Mater, 2014. **13**(1): p. 36-41.

141. Zhang, L., T. Qiu, Z. Zhu, L. Guo, and X. Li, *Self-Healing Polycaprolactone Networks through Thermo-Induced Reversible Disulfide Bond Formation.* Macromolecular Rapid Communications, 2018. **39**(20): p. 1800121.

142. Shi, X., C. Luo, H. Lu, and K. Yu, *Primary recycling of anhydride-cured engineering epoxy using alcohol solvent.* Polymer Engineering & Science, 2019. **59**(s2): p. E111-E119.

143. Kuang, X., Y. Zhou, Q. Shi, T. Wang, and H.J. Qi, *Recycling of Epoxy Thermoset and Composites via Good Solvent Assisted and Small Molecules Participated Exchange Reactions.* ACS Sustainable Chemistry & Engineering, 2018. **6**(7): p. 9189-9197.

144. Kuang, X., Q. Shi, Y. Zhou, Z. Zhao, T. Wang, and H.J. Qi, *Dissolution of epoxy thermosets via mild alcoholysis: the mechanism and kinetics study.* RSC Advances, 2018. **8**(3): p. 1493-1502.

145. Liu, Z., C. Yu, C. Zhang, Z. Shi, and J. Yin, *Revisiting Acetoacetyl Chemistry to Build Malleable Cross-Linked Polymer Networks via Transamidation.* ACS Macro Letters, 2019: p. 233-238.

146. Park, G.S. and J. Crank, *Diffusion in polymers.* 1968.

147. Tu, Y.-O. and A. Ouano, *Model for the kinematics of polymer dissolution.* IBM Journal of Research and Development, 1977. **21**(2): p. 131-142.

148. Peppas, N.A., J. Wu, and E.D. von Meerwall, *Mathematical modeling and experimental characterization of polymer dissolution.* Macromolecules, 1994. **27**(20): p. 5626-5638.

149. Miller-Chou, B.A. and J.L. Koenig, *A review of polymer dissolution.* Progress in Polymer Science, 2003. **28**(8): p. 1223-1270.

150. Tu, Y.-O. and A.C. Ouano, *Model for the kinematics of polymer dissolution.* IBM J. Res. Dev., 1977. **21**(2): p. 131-142.

151. Thombre, A.G. and K.J. Himmelstein, *A simultaneous transport-reaction model for controlled drug delivery from catalyzed bioerodible polymer matrices.* AIChE Journal, 1985. **31**(5): p. 759-766.